

AN INVESTIGATION OF CIRCUMSTELLAR DISK PROPERTIES
IN CLUSTER ENVIRONMENTS

By

KARL E. HAISCH JR.

A DISSERTATION PRESENTED TO THE GRADUATE SCHOOL
OF THE UNIVERSITY OF FLORIDA IN PARTIAL FULFILLMENT
OF THE REQUIREMENTS FOR THE DEGREE OF
DOCTOR OF PHILOSOPHY

UNIVERSITY OF FLORIDA

2000

This dissertation is dedicated to my mother and father.

ACKNOWLEDGMENTS

I am especially grateful to my parents for their love and support throughout my graduate school career. I thank my advisor, Elizabeth Lada, for her advice, support and guidance throughout my graduate work. I also thank Charles Lada for his advice and support.

The author is especially grateful to August Muench and João Alves for acquiring the *JHK* observations of the Trapezium, NGC 2264 and NGC 2362 clusters that were used in this work. I also thank Joanna Levine for providing data on NGC 2024 from CTIO in advance of publication.

I am grateful to my graduate committee members. Their suggestions and comments improved the final version of this work. I thank the Department of Astronomy for supporting me as a graduate teaching assistant during my first year.

Support for this work was provided by a NASA Florida Space Grant Fellowship from 1995 to 1999. Additional support was provided by an ISO grant through the Jet Propulsion Laboratory # 961604, a National Science Foundation award to Elizabeth Lada (NSF AST 9733367) and an ADP (WIRE) grant NAG 5-6751. Accommodations for all observing runs at the NASA Infrared Telescope Facility (IRTF) were provided by the IRTF.

Finally, I thank Lauren Jones, Joanna Levine, Elisha Polomski, Beth Holmes, Tim Spahr and Pimol Moth for their support and friendship.

TABLE OF CONTENTS

ACKNOWLEDGMENTS	iii
LIST OF TABLES	vii
LIST OF FIGURES	ix
ABSTRACT	xi
CHAPTERS	
1 INTRODUCTION	1
1.1 Background	1
1.2 The Star-Formation Process	2
1.3 Evidence for the Existence of Circumstellar Disks	4
1.4 Scientific Issues	6
1.5 Motivation for Study	9
1.6 Target Selection and Description	10
1.7 Thesis Outline	13
2 NEAR-INFRARED OBSERVATIONS AND DATA REDUCTION	15
2.1 The <i>L</i> -Band Observations	15
2.1.1 Primary <i>L</i> -Band Survey	15
2.1.2 Deeper <i>L</i> -Band Survey of NGC 2024 and NGC 2362	17
2.2 The <i>JHK</i> Observations	19
2.3 Standard Star Observations and Dark Frames	20
2.4 Further Details Regarding the Obtention of Near-Infrared Data	21
2.5 Data Reduction	22
2.5.1 Reduction of the STELIRCAM Data	22
2.5.2 Reduction of the NSFCAM Data	25
2.6 Tests of the Near-infrared Data Reduction Procedure	25
3 NEAR-INFRARED CALIBRATION AND SOURCE PHOTOMETRY	28
3.1 Near-Infrared Source Extraction and Photometry	28
3.2 Photometric Calibration	29
3.3 Near-Infrared Photometric Accuracy	30
3.4 Completeness Limits for Near-infrared Data	32
3.5 Astrometry of the Near-infrared Data	35

4	THE TRAPEZIUM AND NGC 2024 CLUSTERS	40
4.1	Results and Spatial Distribution	40
4.2	Color-Color Diagrams	42
4.2.1	Average Extinction	45
4.2.2	Near-Infrared Excess Fractions	47
4.2.3	Sources with Anomalous $K - L$ Colors	52
4.2.4	Infrared Excess Fraction as a Function of Cluster Radius	54
4.2.5	Distribution of $K - L$ Colors	54
4.3	A Circumstellar Disk Census	57
4.4	Disk Fraction vs. Projected Cluster Radius	61
4.5	Nature of Very Red Sources: Candidate Protostars	63
5	MID-INFRARED OBSERVATIONS OF THE NGC 2024 CLUSTER	66
5.1	Motivation for Mid-Infrared Study	66
5.2	Observations and Data Reduction	67
5.3	Spatial Distribution of Mid-Infrared Sources	69
5.4	Spectral Energy Distributions and Spectral Indices	69
5.5	Nondetections and Sensitivity Considerations	74
5.6	Color-Color Diagrams	76
5.7	Luminosity and Extinction Estimates for Class II Sources	80
5.8	Comparison of Near-Infrared and Mid-Infrared Disk Fractions	82
5.9	Nature of the Very Red $K - L$ Sources	83
5.10	Comparison with ρ Oph and Taurus-Auriga	84
6	CIRCUMSTELLAR DISKS IN THE IC 348 CLUSTER	87
6.1	Spatial Distribution	87
6.2	The JHK_L Infrared Excess Fraction	87
6.3	The $H\alpha$ Emission Stars and JHK_L Colors	90
6.4	Effects of Source Variability	91
6.5	A Disk Census in IC 348	93
7	DISK FRACTIONS, LIFETIMES AND PLANET FORMATION	99
7.1	Spatial Distributions	99
7.2	Infrared Excess/Circumstellar Disk Fractions	100
7.2.1	Color-Color Diagrams	100
7.2.2	Effects of Source Variability	104
7.3	Disk Fractions, Lifetimes and Planet Formation	105
7.3.1	Cluster Ages	106
7.3.2	Disk Fractions and Lifetimes	108
7.3.3	Implications for Planet Formation	111
8	THE NGC 2071 AND NGC 2068 CLUSTERS	113
8.1	Spatial Distribution	113
8.2	Infrared Excess/Circumstellar Disk Fractions	113
8.2.1	Color-Color Diagrams	113
8.2.2	Effects of Source Variability	115
8.3	Inferred Ages for NGC 2071 and NGC 2068	116

9	CONCLUSIONS	118
9.1	Disk Formation	118
9.2	Disk Evolution and Planet Formation	119
10	FUTURE WORK	121
APPENDICES		
A	THE <i>JHK</i> L POSITIONS AND PHOTOMETRY FOR NGC 2024 . . .	123
B	THE <i>JHK</i> L POSITIONS AND PHOTOMETRY FOR TRAPEZIUM .	127
C	THE <i>JHK</i> L POSITIONS AND PHOTOMETRY FOR NGC 2071 . . .	137
D	THE <i>JHK</i> L POSITIONS AND PHOTOMETRY FOR NGC 2068 . . .	139
E	THE <i>JHK</i> L POSITIONS AND PHOTOMETRY FOR IC 348	141
F	THE <i>JHK</i> L POSITIONS AND PHOTOMETRY FOR NGC 2264 . . .	144
G	THE <i>JHK</i> L POSITIONS AND PHOTOMETRY FOR NGC 2362 . . .	146
H	THE <i>JHK</i> L POSITIONS AND PHOTOMETRY FOR NGC 1960 . . .	149
REFERENCES		151
BIOGRAPHICAL SKETCH		156

LIST OF TABLES

1-1	Young Embedded Cluster Sample	10
2-1	Summary of Observations	16
3-1	Photometric Solutions for STELIRCAM <i>L</i> -Band Data	31
3-2	Photometric Solutions for NSFCAM <i>L</i> -Band Data	31
3-3	Cluster Completeness Limits	36
4-1	Number of Source Detections in Each Filter	41
4-2	Background Corrected Excess Fractions for the NGC 2024 Cluster . .	49
5-1	The <i>JHKL</i> and $10\mu\text{m}$ Fluxes for Sources Surveyed in NGC 2024 . . .	71
5-2	Luminosities and A_V for Class II Sources	81
6-1	The <i>JHKL</i> Excess Fraction vs. Spectral Type	98
7-1	Number of Sources Detected in Each Cluster	100
7-2	The <i>JHK</i> and <i>JHKL</i> Infrared Excess Fractions	105
8-1	Number of Sources Detected in Each Cluster	113
8-2	The <i>JHK</i> and <i>JHKL</i> Infrared Excess Fractions	116
A-1	The <i>JHKL</i> Photometry of NGC 2024 Sources	123
B-1	The <i>JHKL</i> Photometry of Trapezium Sources	127
C-1	The <i>JHKL</i> Photometry of NGC 2071 Sources	137

D-1	The <i>JHKL</i> Photometry of NGC 2068 Sources	139
E-1	The <i>JHKL</i> Photometry of IC 348 Sources	141
F-1	The <i>JHKL</i> Photometry of NGC 2264 Sources	144
G-1	The <i>JHKL</i> Photometry of NGC 2362 Sources	146
H-1	The <i>JHKL</i> Photometry of NGC 1960 Sources	149

LIST OF FIGURES

1-1	Schematic representation of the star-formation process	3
1-2	The <i>JHK</i> infrared excess fraction vs. cluster age	8
2-1	Tests of photometric reproducibility	27
3-1	Accuracy of the <i>L</i> -band photometry for the Orion clusters	33
3-2	Accuracy of the <i>L</i> -band photometry for the older clusters	34
3-3	Comparison of the <i>L</i> -band STELIRCAM and NSFCAM photometry in NGC 2024	35
3-4	Completeness limits of the SQUID data	37
3-5	Completeness limits of the NGC 2264 STELIRCAM data	38
3-6	Completeness limits of the STELIRCAM data	39
3-7	Completeness limits of the IRTF data	39
4-1	The <i>JHKL</i> images of the NGC 2024 cluster	42
4-2	Source distribution in NGC 2024	43
4-3	The <i>JHKL</i> images of the Trapezium cluster	43
4-4	Source distribution in the Trapezium cluster	44
4-5	The <i>JHK</i> and <i>JHKL</i> color-color diagrams for NGC 2024	45
4-6	The <i>JHK</i> and <i>JHKL</i> color-color diagrams for the Trapezium	46
4-7	The <i>JHK</i> color-color diagram for the SQUID control fields	48
4-8	Disk fraction vs. projected cluster radius	55
4-9	Distribution of <i>K</i> – <i>L</i> colors	56

4-10	The <i>JHK</i> and <i>JHKL</i> color-color diagrams for Taurus	58
4-11	The <i>JHKL</i> color-color diagram for the Trapezium proplyds	59
5-1	Distribution of mid-infrared sources in the NGC 2024 cluster	70
5-2	Radial surface density profile of mid-infrared sources	70
5-3	Spectral energy distributions of detected mid-infrared sources	72
5-4	Distribution of the 2.2 to 10 μm spectral indices	73
5-5	Expected <i>N</i> -band flux vs. <i>K</i> -band magnitude	75
5-6	Percentage of 10 μm sources detected vs. <i>K</i> -band magnitude	75
5-7	Color-color diagram for mid-infrared sources	77
5-8	Color-color diagram of <i>K</i> – <i>L</i> vs. <i>K</i> – <i>N</i>	79
6-1	Distribution of <i>L</i> -band sources in IC 348	88
6-2	The <i>JHKL</i> color-color diagram for IC 348	89
6-3	The <i>JHKL</i> colors of the $\text{H}\alpha$ sources in IC 348	91
6-4	The <i>JHKL</i> colors of CTTS and WTTS stars in IC 348	92
6-5	The <i>JHKL</i> colors of CTTS and WTTS stars in Taurus-Auriga	95
7-1	Source distributions in NGC 2264, NGC 2362 and NGC 1960	101
7-2	The <i>JHK</i> and <i>JHKL</i> color-color diagrams for NGC 2264	102
7-3	The <i>JHK</i> and <i>JHKL</i> color-color diagrams for NGC 2362	102
7-4	The <i>JHK</i> and <i>JHKL</i> color-color diagrams for NGC 1960	103
7-5	The <i>JHK</i> and <i>JHKL</i> excess fractions vs. cluster age	106
7-6	Plot of <i>J</i> -band magnitude vs. spectral type in IC 348	109
7-7	The <i>J</i> -band luminosity functions for NGC 2264 and NGC 2362	110
8-1	Source distributions in NGC 2071 and NGC 2068	114
8-2	The <i>JHK</i> and <i>JHKL</i> color-color diagrams for NGC 2071	115
8-3	The <i>JHK</i> and <i>JHKL</i> color-color diagrams for NGC 2068	116

Abstract of Dissertation Presented to the Graduate School
of the University of Florida in Partial Fulfillment of the
Requirements for the Degree of Doctor of Philosophy

AN INVESTIGATION OF CIRCUMSTELLAR DISK PROPERTIES
IN CLUSTER ENVIRONMENTS

By

Karl E. Haisch Jr.

December 2000

Chairman: Dr. Elizabeth A. Lada
Major Department: Astronomy

Circumstellar disks generally are thought to be a common result of the star formation process. Analogy with the solar system suggests that these disks are protoplanetary disks, the likely formation sites of extra-solar planetary systems. While most of our knowledge regarding the properties of circumstellar disks comes from studies of isolated star-forming regions, most stars in our Galaxy likely form in dense embedded clusters. In this thesis, we have undertaken the first extensive program of *L*-band ($3.4\ \mu\text{m}$) imaging surveys of eight nearby young clusters to determine the circumstellar disk dissipation timescale, and thus evaluate the overall likelihood and conditions of planet formation in the Galaxy.

The derived disk fractions in the youngest clusters lead us to suggest that the formation of circumstellar disks is indeed a common result of star formation, and is not dependent on environment (cluster vs. isolation). If no massive stars are present in the clusters, we show that the disks are not preferentially destroyed in the dense

cluster environment. An examination of successively older clusters reveals that the overall disk fraction decreases with increasing cluster age. We show that the rate of decline also appears to be a function of stellar mass, such that disks surrounding high-mass stars have shorter lifetimes compared with disks surrounding lower mass stars. Finally, we derive the disk dissipation timescale and discuss the implications of this lifetime on the formation of planetary systems.

CHAPTER 1 INTRODUCTION

1.1 Background

Circumstellar disks are of fundamental astrophysical interest. They play a critical role in the star formation process because they are believed to be the primary channel for accreting most of the interstellar gas and dust that ultimately forms a star. More significantly perhaps, analogy with the solar system suggests that circumstellar disks are protoplanetary disks, that is, the likely formation sites of extra-solar planetary systems. The recent detection of small amplitude Doppler periodicities toward a number of nearby field stars provided compelling proof of the existence of extra-solar planetary systems and reinforced the notion that planetary systems may be common in the Galaxy (Marcy & Butler 1999).

We do not yet know how ubiquitous planetary systems really are. Obtaining a meaningful census via direct and indirect detections of planetary systems is a formidable challenge that requires the development of new technological capabilities such as precision astrometric and photometric observations from space. Nevertheless, a meaningful estimate of the frequency of planetary systems is indirectly possible from observations of protoplanetary disk systems. Such observations already are possible using existing technology at ground-based observatories. Thus, obtaining a statistically meaningful census of circumstellar disks around young stars may be a very efficient first step toward determining the frequency of planetary systems in the Galaxy. Before we concentrate on the disk/planet-forming frequencies in populations of young stars, let us briefly investigate the overall process of star formation and the evidence for the existence of circumstellar, protoplanetary disks.

1.2 The Star-Formation Process

In Figure 1-1, we present a schematic diagram of the star formation process. This diagram was reproduced from Wilking et al. (1989), who adapted it from Lada (1987) and Shu et al. (1987). Each step in the star-formation process is shown on the right-hand side of Figure 1-1; on the left-hand side is the corresponding spectral energy distribution (SED). Young stellar objects (YSOs) were arranged in four classes by Lada (1987) based on the slope of the 2.2 to 25 μm SED in a $\log \lambda F_\lambda$ vs. $\log \lambda$ plot. Adams et al. (1987) proposed a more or less continuous evolutionary sequence to unite these classifications, which is well modelled by at least one physically self-consistent theory of star formation and early stellar evolution.

The initial phase of the star formation process is characterized by the collapse of a molecular cloud core. The cloud core collapses gravitationally from the inside out. In the inner regions of the core, we find an accreting protostellar object surrounded by a nebular disk. Theory suggests that the formation of circumstellar disks is a natural consequence of star formation in rotating, collapsing protostellar cloud due to the conservation of angular momentum. The collapse proceeds much faster along the axis of rotation, where the centrifugal forces are small, than on the equatorial plane. This naturally leads to a disk-like configuration. This configuration is surrounded by a dusty infalling envelope. These sources are classified as Class I YSOs by Adams et al. (1987). Because of the large amount of circumstellar dust surrounding these sources, the SEDs of Class I sources are broader than a single blackbody function and peak at far-infrared, submillimeter and millimeter wavelengths. These SEDs rise with increasing wavelength longward of 2.2 μm producing an extremely large infrared “excess” compared to that expected from a normal stellar photosphere.

At some point, an outflow develops along the rotational poles of the system. The infalling envelope gradually is depleted during this phase and the SED is modified significantly. As the envelope is depleted, there is successively less extinction toward

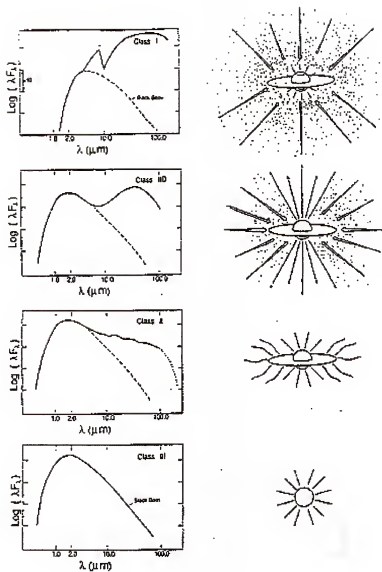


Figure 1-1: Schematic representation of the star formation process. The phases are shown in chronological order from top to bottom. They are protostar, outflow phase, T Tauri or Herbig Ae/Be star and main sequence star. A diagram and SED are shown for each phase. The diagram is reproduced from Wilking et al. (1989).

the central source. As a result, the SED exhibits two peaks, one at short wavelengths due to the central star/disk system, and a second peak at longer wavelengths due to emission from the remnant infalling envelope. Such sources are classified as flat spectrum YSOs. The typical lifetime of sources in the Class I/flat spectrum phases of evolution is on the order of 1 to 5×10^5 yr (Myers et al. 1987; Wilking et al. 1989; Kenyon et al. 1990).

Over time, the infall stops and the system becomes visible, even at ultraviolet, optical and near-infrared wavelengths as a star/disk system to all observers. The optical portion of the SEDs of these so-called Class II YSOs resembles that of a normal stellar photosphere, while the infrared portion of the spectrum exhibits “excess” emission which is well described by a power-law with $\nu F_\nu \propto \nu^\alpha$, where $\alpha = -1.33$ (Lynden-Bell & Pringle 1974; Adams et al. 1987). These sources correspond to the classical T-Tauri and Herbig Ae/Be stars, and have lifetimes ranging from less than 1 Myr to ~ 10 Myr (Lada 1999a).

The circumstellar disks eventually are removed, by either accretion onto the central star, dissipation by strong stellar winds, or condensation into planetary systems; and what remains is the star itself. These sources have SEDs that resemble blackbodies and that are classified as Class III objects. While most Class III YSOs have ages > 5 Myr, a significant number have ages that overlap with those of Class II sources (Walter 1987). An abundance of more detailed information on the star formation process is available [Lada & Kylafis (1991, 1999); Levy & Lunine 1993; Mannings et al. 2000].

1.3 Evidence for the Existence of Circumstellar Disks

Over 20 years ago, Lynden-Bell & Pringle (1974) suggested that the SEDs of T Tauri stars could be explained if these objects were surrounded by circumstellar disks. A few years later, Elsässer & Staude (1978) discovered high degrees of linear

polarization in the optical light from a number of young stars. The polarization was thought to arise from light scattered from dust grains symmetrically arranged above and below a star obscured by a planar or toroidal distribution of dust oriented parallel to the direction of polarization and perpendicular to the line of sight to the star. Thus, the dust around these stars appeared to be arranged in an axisymmetric and flattened distribution.

Further suggestions of flattened distributions of circumstellar material surrounding many pre-main sequence (PMS) stars came from the discovery of well collimated optical jets (Mundt & Fried 1983) and bipolar molecular outflows (Snell et al. 1980) in these objects. In addition, the emission line profiles seen in the spectra of very young stars are preferentially blue-shifted. This implies the presence of circumstellar disks that obscure the red-shifted line emission (e.g., Appenzeller et al. 1984). Furthermore, excess infrared (e.g., Rucinski 1985) and millimeter (e.g., Beckwith et al. 1990) emission imply that, to preserve an optically thin line of sight to the star at visible wavelengths, the circumstellar dust must be distributed in a non-spherical geometry (Myers et al. 1987).

Circumstellar disks have been observed both directly and indirectly around numerous young stellar objects via optical, infrared, centimeter and millimeter wave observations (e.g., Beckwith 1999; Menard & Bertout 1999; Lada 1999a; Wilner et al. 2000) and even resolved in optical and millimeter wavelength images (McCaughrean & O'Dell 1996; Dutrey et al. 1996). The fact that circumstellar disks frequently are observed around the youngest sunlike stars suggests that the formation of planetary systems may be relatively common in the Galaxy and a natural byproduct of the star-formation process itself.

1.4 Scientific Issues

Existing observations of extra-solar planets and circumstellar disks clearly indicate a significant diversity in the nature of these systems, and raise a number of basic questions regarding the processes of planet formation and disk evolution. For example: What is the duration of the circumstellar disk/planet building phase of early stellar evolution? Is it a function of stellar mass or environmental (i.e., initial) conditions? Do disks form around high- as well as low-mass stars?

To address these very basic issues and to advance our understanding of both the nature of disks and planet formation within them, we require detailed knowledge of the frequencies, lifetimes and physical properties of circumstellar disks in populations of young stars. Most of our knowledge regarding the properties of circumstellar disks comes from studies of regions of isolated or distributed star formation such as Taurus. In these regions, 30 to 50% of the young stars (ages ≤ 3 Myr) with masses $M \leq 3M_{\odot}$ exhibit infrared excesses indicative of optically thick disks. Modelling of the broad-band SEDs of these solar-type PMS stars revealed that the typical sizes of these disks range from ~ 10 to 1000 AU with masses from $0.01 < M_{\text{disk}}/M_{\odot} < 0.1$. Thus, a significant fraction of solar-type PMS stars in isolated environments appear to be surrounded by circumstellar disks of solar system sizes having masses at least that of the minimum-mass solar nebula ($M \simeq 0.01 M_{\odot}$). The survival times of these disks as massive, optically thick structures range from $t < 3$ Myr to $t \simeq 10$ Myr (Strom et al. 1993).

However, it is unlikely that most stars form in such isolated environments. Rather, most stars in our Galaxy are widely believed to form in dense embedded clusters (Lada et al. 1991; Lada 1992; Carpenter et al. 1995; Phelps & Lada 1997; Meyer & Lada 1999; Carpenter 2000). These young clusters contain hundreds of stars covering a large range in mass with similar chemical compositions in a relatively small volume at the same distance from the Sun. In addition, since the ages of

clusters can be determined from the Hertzsprung-Russell (HR) diagram, they can be used as chronometers to study the early phases of star formation and evolution in a statistically meaningful way.

Young star clusters represent a different star-forming environment (e.g., high stellar density, the possible presence of massive O stars) as compared to isolated star-forming regions. Thus, one might expect to find fundamental differences in the star-formation process between such regions. A particularly important consideration is the potential effect of the cluster environment on the formation and subsequent evolution of the circumstellar disks which are commonly believed to surround many of the newly formed cluster members (e.g., Johnstone et al. 1993; Störzer & Hollenbach 1999). Because these disks represent the sites of any subsequent planet formation, determining the properties of disks in cluster environments is essential to evaluating the overall likelihood of planetary formation in the Galaxy.

Near-infrared *JHK* (1.25, 1.65, 2.2 μm) color-color diagrams (e.g., plot of $J - H$ vs. $H - K$) have long been used as tools for investigating the physical natures of YSOs in young clusters (Lada & Adams 1992; Lada et al. 1993; Lada & Lada 1995; Lada et al. 1996). In Figure 1-2, we present the infrared excess fractions for several young clusters as determined from their *JHK* colors (Lada 1999). A large fraction of the sources in clusters younger than about 2 Myr exhibit infrared excess emission above that expected for normal stellar photospheres. Such infrared excesses indicate the possible presence of circumstellar, protoplanetary disks. This suggests that there is a high fraction of sources with disks in these very young clusters. In contrast, clusters older than 2 Myr exhibit much smaller infrared excesses, suggesting a small disk fraction. Thus, the infrared excess fraction clearly decreases with increasing cluster age and from this we estimate the lifetimes of disks in such environments to be only a few million years.

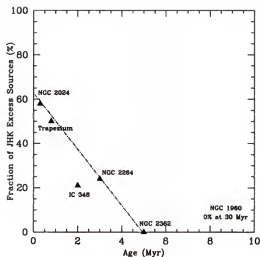


Figure 1-2: The *JHK* infrared excess fraction vs. cluster age. The near-infrared excess fraction decreases as a function of cluster age, suggesting that the average lifetime of circumstellar disks is on the order of a few million years. The figure was adapted from Lada (1999).

The *JHK* observations alone, however, are not long enough in wavelength to enable complete and unambiguous disk identification. This is partly because of problems arising from contamination by extended emission in HII regions, reflection nebulosity, stellar photospheric emission and source crowding in regions of high stellar density. Such effects could lead to artificially high or low disk fractions as inferred from infrared excesses in *JHK* color-color diagrams. Furthermore, the magnitude of the near-infrared excess from a disk also depends on the parameters of the star/disk system (e.g., stellar mass/age, disk inclination, accretion rate, inner disk hole size) [Adams et al. 1987 (hereafter ALS87); Meyer et al. 1997; Hillenbrand et al. 1998]. Are the circumstellar disk lifetimes in clusters really as short as the *JHK* observations imply?

1.5 Motivation for Study

Ideally, one would obtain broad-band energy distributions of a significant fraction of sources in many young clusters to the hydrogen burning limit to study the frequency and lifetimes of the protostellar and disk phases of early stellar evolution. Unfortunately, this is impractical because of the very large sky background, the relative faintness of systems in clusters, and the large number of stars to be measured. In addition, observations at long wavelengths (i.e., longer than about $10\ \mu\text{m}$) are not sensitive enough to detect photospheric emission except from rather massive stars.

Circumstellar disks emit strongly at infrared wavelengths and produce radiation significantly in excess of that emitted by young stellar photospheres. These infrared excesses can readily be detected by near-infrared imaging observations. The magnitude of the infrared excess produced by a disk rapidly increases with wavelength. Current instrument sensitivities in the *L*-band ($3.4\ \mu\text{m}$) are sufficient to detect relatively faint low-mass stars because the *L*-band wavelength is sufficiently near the peak of the stellar energy distribution of a typical late-type star. In this respect, *L*-band observations are far superior to mid-infrared observations (i.e., $\geq 10\ \mu\text{m}$) made at the world's best sites with the largest telescopes. In addition, one can survey large areas in many clusters at *L*-band in reasonable amounts of telescope time, a capability not presently possible using mid-infrared detectors on ground-based telescopes. Hence, statistically significant numbers of stars in young clusters can be obtained from observations in the *L*-band. Therefore, combining near-infrared *JHK* observations with *L*-band data is an extremely powerful method for investigating the nature of young stellar sources.

To exploit the capabilities of *L*-band observations to study the frequency and lifetime of circumstellar disks, we conducted the first extensive program of *L*-band imaging surveys of eight nearby young clusters. The clusters span a range of ages (≤ 1 to $30\ \text{Myr}$) and environments (e.g., stellar density and stellar content). The

aim of this study is to determine the circumstellar disk fraction in each cluster and to investigate the dependence of the disk fraction on cluster age and environment. This will not only provide the first statistically significant census of the frequency distributions of circumstellar disks in cluster environments but, since the duration of the disk phase of stellar evolution sets the timescale for planet formation, the results of this study will also set strong and meaningful constraints on the likelihood and conditions of planet formation in the Galaxy.

1.6 Target Selection and Description

Our sample clusters are listed in Table 1-1. Column 1 lists the names of the clusters. The Right Ascension and Declination coordinates (epoch J2000) are given in Columns 2 and 3. The cluster distances (in parsecs) and mean ages are given in Columns 4 and 5 respectively.

Table 1-1: Young Embedded Cluster Sample

Cluster	RA (h:m:s;J2000)	Dec ($^{\circ}$,',";J2000)	Distance (pc)	Mean Age (Myr)
NGC 2024	05 41 43.50	-01 54 17.0	415	0.3
Trapezium	05 35 16.47	-05 23 22.9	470	0.8
NGC 2071	05 47 04.40	+00 21 19.0	415	~1.5
NGC 2068	05 46 47.70	+00 00 50.0	415	~1.5
IC 348	03 44 30.00	+32 17 00.0	320(260)	3(2)
NGC 2264	06 38 00.00	+09 40 00.0	760	3
NGC 2362	07 18 48.00	-24 57 00.0	1500	5
NGC 1960	05 36 12.00	+34 08 24.0	1200	30

Young Embedded Cluster Sample. Positions, distances and mean ages for the sample clusters. The columns are as follows: (1) Cluster name, (2) Right Ascension (J2000), (3) Declination (J2000), (4) cluster distance in parsecs, and (5) mean age in Myr. References for the distances and mean ages are given in the text.

The NGC 2024, NGC 2071 and NGC 2068 clusters all are associated with the L1630 (Orion B) molecular cloud (Lada et al. 1991). Since all three clusters are associated with the same molecular cloud, we assume a distance to each cluster of 415 pc (Anthony-Twarog 1982). The NGC 2024 cluster has a high overall stellar

surface density ($\rho \simeq 172$ stars pc^{-2} ; Lada 1999), a young mean age (~ 0.3 Myr; Meyer 1996) and contains an O9.5 star (Thompson et al. 1981). The NGC 2024 cluster and surrounding HII region is well studied. Barnes et al. (1989) described the structure of the HII region and surrounding molecular material in detail, and their K -band ($2.2 \mu\text{m}$) imaging also revealed a cluster consisting of ~ 30 infrared sources. A detailed near-infrared JHK imaging survey conducted by Lada et al. (1991) to study global star formation in the L1630 molecular cloud yielded a large number (~ 300) of faint infrared sources in the NGC 2024 cluster. Subsequent JHK imaging of the central region of NGC 2024 led to the conclusion that a large fraction, perhaps as high as two-thirds, of the low mass objects in this young embedded cluster display infrared excesses characteristic of circumstellar disks [e.g., Comerón et al. 1996 (hereafter CRR96)].

The NGC 2071 and NGC 2068 clusters are somewhat less dense ($\rho \simeq 132$ and 112 stars pc^{-2} respectively; Lada 1999) and may be older (ages ~ 1 to 2 Myr) than NGC 2024 (Launhardt et al. 1996; Lada et al. 1997; Gibb 1999; Gibb & Little 2000). The young ages of these two clusters were inferred from the fact that they are embedded deeply in the L1630 molecular cloud and contain high fractions of infrared excess sources. These clusters contain no O stars and thus represent less harsh environments than NGC 2024. Lada et al. (1991) observed NGC 2071 and NGC 2068 as part of their $2.2 \mu\text{m}$ survey of the L1630 cloud. They uncovered 105 and 192 sources in the NGC 2071 and NGC 2068 clusters respectively.

The Trapezium cluster is a very rich cluster (~ 1600 stars within 2.5 pc of the Trapezium stars) within the Great Orion Nebula. The cluster resides in the L1641 molecular cloud at a distance of ~ 470 pc (Genzel et al. 1981), has a mean age of ~ 0.8 Myr (Hillenbrand 1997) and contains many massive O and B type stars. Many near-infrared JHK studies of the Trapezium cluster already were completed (e.g., McCaughrean & Stauffer 1994; Ali & Depoy 1995; Hillenbrand et al. 1998).

There is ample observational evidence for a large population of star/disk systems in the Trapezium cluster. Resolved Hubble Space Telescope images of silhouetted disks within the cluster (McCaughrean & O'Dell 1996) are perhaps the most compelling demonstration for the existence of circumstellar disks around young stars yet obtained. However, the exact size of the disk population still is uncertain.

The IC 348 cluster is a relatively dense ($\rho \simeq 105$ stars pc^{-2} ; Lada 1999) cluster located in the Perseus molecular cloud. The cluster contains no O stars; the earliest type star is of spectral class B5 V. The distance to IC 348 is somewhat uncertain. The most straightforward and precise method, averaging parallaxes of cluster members measured by the Hipparcos satellite, yields a distance of ~ 260 pc (Scholz et al. 1999), marginally closer than the distance of ~ 320 pc derived from the HR diagram (Herbig 1998). Most of the star formation in IC 348 occurred within the past 3 Myr, with a mean age of ~ 2 to 3 Myr depending on the distance (Luhman et al. 1998). Previous combined near-infrared studies of IC 348 revealed approximately 350 infrared sources in the cluster (Strom et al. 1974; Lada & Lada 1995).

The NGC 2264 cluster is a very well known cluster located in the Monoceros OB 1 association at a distance of 760 pc (Sung et al. 1997). The most massive star in the cluster is the O7 V star S Mon. The age of most PMS stars in NGC 2264 is in the range 0.8 to 8 Myr, with a mean age of approximately 2 Myr (Sung et al. 1997). A more recent study of NGC 2264 by Soderblom et al. (1999) indicates a mean age of ~ 3 Myr with an age spread of only 4 Myr. Infrared imaging of NGC 2264 revealed that the cluster contains $360 (\pm 130)$ members, and $50\% \pm 20\%$ of these stars exhibit infrared excess emission indicative of circumstellar disks (Lada et al. 1993).

The remaining two clusters in our sample, NGC 2362 (distance $\simeq 1500$ pc; Balona & Laney 1996) and NGC 1960 (distance $\simeq 1200$ pc; Barkhatova et al. 1985, Sanner et al. 2000), are open clusters located in Canis Major and Auriga respectively.

Isochrone fitting yields an age for NGC 2362 of ~ 5 Myr (Balona & Laney 1996), while NGC 1960 represents the oldest cluster in the sample (age ~ 30 Myr; Barkhatova et al. 1985). The NGC 2362 cluster contains the O star binary HD 57061. The NGC 1960 cluster does not contain O stars. Neither cluster was studied at near-infrared wavelengths.

1.7 Thesis Outline

In Chapter 2, we describe how the observations were made. In Chapter 3, we present a detailed description of our methods of stellar photometry, including calibration of the data and estimates of the accuracy of the photometry. We conclude Chapter 3 by examining the completeness limits of the surveys and determining of the stellar position on the celestial coordinate system.

Chapters 4, 5, 6 and 7 constitute the main scientific sections of this work. In Chapter 4, we examine the infrared excess (candidate circumstellar disk) fractions in the NGC 2024 and Trapezium clusters. These excess fractions then are compared to those in Taurus, where star formation occurs in relative isolation. We finish the chapter with an investigation of the protostellar population in both NGC 2024 and the Trapezium.

We discuss the results of our mid-infrared survey of NGC 2024 in Chapter 5. We examine both the protostellar and circumstellar disk fractions and compare the results with the respective fractions obtained in our *JHKL* surveys. As in the previous chapter, we also compare our results with the Taurus star-forming region.

In Chapter 6, we investigate the circumstellar disk fraction in IC 348, and compare the results to the younger NGC 2024 and Trapezium clusters. Disk lifetimes are studied and compared to the lifetimes of disks in Taurus.

In Chapter 7, we combine the results for clusters (except NGC 2071 and NGC 2068) of our sample clusters. To this end, we compare the infrared excess fractions

in each cluster and identify any trends in excess fraction as a function of cluster age and environment. We compare the results with previous studies of young clusters and isolated star-forming regions. We conclude the chapter with an examination of the likelihood and conditions for planet formation in the Galaxy.

In Chapter 8, we briefly discuss the NGC 2071 and NGC 2068 clusters. The penultimate chapter summarizes the major scientific results of this work. We conclude with suggestions for improvement in the present work, as well as directions for future study.

CHAPTER 2 NEAR-INFRARED OBSERVATIONS AND DATA REDUCTION

In this chapter, we discuss the near-infrared observations obtained for this survey. A summary of all observations is presented in Table 2-1. The table lists the clusters observed, observation dates, total integration times, filters used and areal coverage for each filter.

2.1 The *L*-Band Observations

2.1.1 Primary *L*-Band Survey

All of the clusters in our survey except NGC 2362 were observed at *L*-band with the dual channel infrared camera STELIRCAM on the Fred Lawrence Whipple Observatory (FLWO) 1.2 meter telescope on Mt. Hopkins, Arizona. The camera consists of two 256×256 InSb detector arrays. Each is fed from a dichroic that separates wavelengths longer (red array) and shorter (blue array) than 1.9 μm . Three separate magnifications can be selected by rotating different cold lens assemblies into the beam. For all observations, we selected a field of view of 2.5'×2.5' with a resolution of 0.6" per pixel. Typically, the camera was configured to obtain both *H*- and *L*-band observations.

In the NGC 2024, NGC 2071, NGC 2068 and IC 348 clusters, we observed twenty-five fields arranged in a 5×5 square covering an area of ~ 110 arcmin². The individual images were overlapped by 30" in both Right Ascension (RA) and Declination (Dec). This overlapping provided redundancy for the photometric measurements of sources located in the overlapped regions, and enabled the construction of accurate positional mosaics of each cluster. Each individual field in the mosaic was observed in

Table 2-1: Summary of Observations

Cluster	Date (UT)	Integration Time (sec)	Filter	Survey Area (arcmin ²)
NGC 2024	01/92	180	<i>J,H,K</i>	~450
NGC 2024	01/98	180	<i>H,L</i>	~110
NGC 2024	01/99	280	<i>L</i>	~6.25
NGC 2024	12/96, 09/97	45	10 μ m	N/A ¹
NGC 2071	01/92	180	<i>J,H,K</i>	~450
NGC 2071	01/98	180	<i>H,L</i>	~110
NGC 2068	01/92	180	<i>J,H,K</i>	~450
NGC 2068	01/98	180	<i>H,L</i>	~110
Trapezium	12/97	540	<i>J,H,K</i>	~36
Trapezium	12/97	360	<i>L</i>	~36
Trapezium	11/98	180	<i>J,H,L</i>	~49
Trapezium	02/00	140	<i>L</i>	N/A ²
IC 348	01/92	180	<i>J,H,K</i>	~450
IC 348	02/98	180	<i>H,L</i>	~110
NGC 2264	12/98	720	<i>J,H,K</i>	~800
NGC 2264	12/98	1080	<i>L</i>	~42
NGC 2362	12/96	900	<i>J,H,K</i>	~120
NGC 2362	02/00	280	<i>L</i>	~28
NGC 1960	—	1.455	<i>J,H,K_s</i>	— ³
NGC 1960	02/98	1080	<i>H,L</i>	~42

¹Mid-infrared observations were performed on a source by source basis. Therefore, no area was computed.

²Two frames were obtained for cross-calibration purposes.

³The *JHK_s*-band data for NGC 1960 was extracted from the 2MASS archive.

a 3×3 square pattern with $12''$ offsets or dithers between positions. The pattern was observed such that the telescope was not offset in the same direction twice. Once the 9 dithered positions were observed, the telescope was offset by $5''$ and the pattern was repeated. The integration time at each dither position was 10 seconds ($0.1 \text{ second} \times 100 \text{ coadditions}$) with a total integration time for each field of 3 minutes. Our 3σ and 5σ sensitivity limits for these data are 13.2 and 12.7 respectively.

In the NGC 2024 cluster, four of the 25 fields, covering the inner ~ 20 square arcminutes of the cluster, were observed for a total integration time of 18 minutes. These fields were observed using the method described above with the inclusion of a $7''$ dither between each 3 minute sequence. The 3σ and 5σ sensitivity limits are 14.3 and 13.8 respectively.

Nine fields in the NGC 2264 and NGC 1960 clusters were observed in a 3×3 square that covered an area of $\sim 42 \text{ arcmin}^2$. Each field in the square was observed for a total integration time of 18 minutes using the method described for the four clusters above with the inclusion of a $7''$ dither between each 3 minute sequence. For NGC 2264, our 3σ and 5σ sensitivity limits are 13.6 and 13.2 respectively. These sensitivity limits are 14.3 and 13.8 for NGC 1960.

The *L*-band observations of the Trapezium cluster were graciously obtained by João Alves. The acquisition of these data is described in Lada et al. (2000).

2.1.2 Deeper *L*-Band Survey of NGC 2024 and NGC 2362

Additional *L*-band observations of the NGC 2024 and NGC 2362 clusters were made with NSFCAM on the NASA Infrared Telescope Facility (IRTF) 3.0 meter telescope on Mauna Kea, Hawaii. The NSFCAM array consists of a single 256×256 InSb detector array. Three different magnifications can be selected by rotating different cold lens assemblies into the beam. For our deep study, we used a plate scale of $0.3''$ per pixel with a corresponding field of view of approximately $1.25' \times 1.25'$.

Four fields centered on the NGC 2024 cluster were observed in a 2×2 square covering an area of $\sim 6.25 \text{ arcmin}^2$. The fields were observed using the same method described above for the STELIRCAM observations of this cluster with the exception that, between each dither position, the telescope was nodded to separate sky positions $300''$ east of the cluster. The total integration time for each field was ~ 4.6 minutes.

For the NGC 2362 cluster, twenty-five fields arranged in a 5×5 square covering an area of $\sim 28 \text{ arcmin}^2$ were observed using NSFCAM. The individual images were overlapped by $15''$ in both Right Ascension and Declination to provide redundancy for the photometric measurements of sources located in the overlapped regions and enabled an accurate positional mosaic of the cluster to be constructed. Each individual field in the mosaic was observed in a 3×3 square pattern with $12''$ dithers between positions. The pattern was observed such that the telescope was not offset in the same direction twice. Once the 9 dithered positions were observed, the telescope was offset by $5''$ and the pattern was repeated. The integration time for a single position was 0.1 second with 100 coadditions. The total integration time for each field was ~ 4.6 minutes. The 3σ and 5σ sensitivity limits for our NSFCAM L -band data are 14.9 and 14.6 respectively.

Two fields in the Trapezium cluster also were acquired at L -band with NSFCAM to internally calibrate our STELIRCAM L -band data (see next chapter). Both fields were observed in a 3×3 square pattern with $12''$ dithers between positions. The pattern was observed such that the telescope was not offset in the same direction twice. Once the 9 dithered positions were observed, the telescope was offset by $5''$ and the pattern was repeated. The integration time for a single position was 0.1 second with 100 coadditions. The total integration time for each field was ~ 4.6 minutes. The 3σ and 5σ sensitivity limits for these fields are 14.9 and 14.6 respectively.

2.2 The *JHK* Observations

The *JHK* observations for the NGC 2024, NGC 2071, NGC 2068 and IC 348 clusters were taken with the Simultaneous Quad Infrared Imaging Device (SQIID) at Kitt Peak National Observatory on the 1.3 meter telescope by Dr. Elizabeth Lada. The SQIID array consists of four 256×256 PtSi detector arrays that are mounted to permit simultaneous observations at *J*, *H*, *K*, and *L*-bands. The *L*-band saturates quickly because of the high sky background, so only the *J*, *H*, and *K*-bands were used. On the 1.3 meter telescope, SQIID provides an imaging scale of $1.36''$ per pixel at *K*-band with a field of view of $5.5' \times 5.5'$.

For the NGC 2024, NGC 2071 and NGC 2068 clusters, twenty-five SQIID fields were observed in a 5×5 mosaic covering an area of $\sim 450 \text{ arcmin}^2$ on the sky. Each SQIID field was overlapped by 1.5 arcminutes in both Right Ascension and Declination, allowing for both redundancy of photometric measurements of sources located in the overlapped regions and accurate positional placement of the mosaicked fields. Note that in all subsequent analysis, we only considered the respective areas included in our *L*-band surveys. The remaining *JHK* data for these clusters are analyzed in Dahari & Lada (2001). Eighteen control fields (covering an area of $\sim 545 \text{ arcmin}^2$) located well away from the cluster were observed to account for the distribution of foreground/background field stars. These fields were found to be free of significant molecular material by examination of the Palomar Sky Survey Prints. The integration time in each filter was 3 minutes for observations of both cluster and control fields. Each field was observed twice with a $15''$ dither between observations. Each pair of dithered images was combined to produce images with an effective integration time of 6 minutes in each filter.

Acquisition of the IC 348 *JHK* data is discussed in Lada & Lada (1995). The *JHK* observations of the Trapezium cluster were carried out by August Muench using STELIRCAM at the FLWO as discussed in Lada et al. (2000), and graciously

provided to the author for integration into this work. August Muench also carried out the *JHK* observations of the NGC 2264 cluster at FLWO. The *J*, *H* and *K_s* (2.1 μm) observations of the NGC 1960 cluster were taken from the 2MASS data archive (see <http://pegasus.astro.umass.edu>). The *JHK* observations of the NGC 2362 cluster were graciously obtained at the European Southern Observatory (ESO) 2.3 meter telescope by João Alves and provided to the author in advance of publication.

2.3 Standard Star Observations and Dark Frames

Infrared standard stars selected from the Elias list (Elias et al. 1982) were observed during each observing run to properly calibrate the *JHKL* band photometry for all sources in each cluster, with the exception of NGC 1960 (see next chapter for details regarding calibration and photometry procedures). In particular, the following standard stars from the Elias list were observed on each night of all observing runs: HD 1160, HD 22686, HD 40335, HD 77281 and HD 106965. All infrared standards were selected based on their proximity to the target cluster, their ability to be followed over a wide range of airmasses and their reliability as true photometric standards. The standards for the *L*-band data were observed in a 3 \times 3 square pattern with 12" dithers between positions. The pattern was observed such that the telescope was not offset in the same direction twice. At *L*-band, the integration time for each dither position was 1 second (0.1 second with 10 coadditions), with a total integration time of 9 seconds. Acquisition of the *JHK* standards for the SQIID data is discussed in Lada & Lada (1995). A discussion of the calibration procedure for the *JHK_s* data for NGC 1960 can be found at the 2MASS website (<http://pegasus.astro.umass.edu>).

In addition to the cluster, control field and standard star observations, we also obtained the necessary data to account for dark current. Charge accumulation occurs in each pixel of the detector, even when the detector is not exposed to photons. Because each pixel in the infrared detectors used is essentially independent of

the others, dark current can vary from pixel to pixel (linearity also is affected in the same way and is discussed in the next section). Thus, it is necessary to obtain dark frames to calibrate this effect. Dark frames were observed at the beginning and end of each night, using the same combinations of integration times and coadditions as the observed images. Because dark current is directly proportional to the integration time, and read noise is independent of integration time, we cannot scale a long exposure dark frame since zero point offsets and readout noise are not treated correctly by the scaling procedure. Taking darks at both the beginning and end of each night also allows a check of the dark stability. No significant difference was observed among the dark frames taken over the course of all observations.

2.4 Further Details Regarding the Obtention of Near-Infrared Data

Before we discuss the reduction of the data, it is instructive to examine the two readout methods by which the data were obtained. The *JHK* observations were made using a readout procedure called correlated double sampling. This mode involves making two measurements: one at the beginning of the integration and another at the end. The voltages of all the pixels in the array are reset in sequence without reading the output voltages. The first measurement is made immediately afterwards, and the second is made at the end of the integration time, just before the voltages are reset again. The difference between the two reads yields the desired signal. By taking the difference between the two measurements, one reduces the effects of the inherent uncertainty in the initial voltage level (the bias) and also the long-term (e.g., low frequency) drifts.

Correlated double sampling was also used in the acquisition of the *L*-band NSFCAM data. However, because the background is much higher at *L*-band, our integration times are significantly shorter (i.e., 0.1 second vs. a few seconds or more at *JHK*) to avoid saturation. In addition, the bias across the array (and thus the

well depth) is increased allowing one to reach higher counts before detector non-linearity (discussed later) becomes a factor. This also helps to mitigate the problem of saturation due to the high background.

The *L*-band STELIRCAM data were taken using a single readout mode in which each pixel in the array is reset and, at the end of the integration time, the voltages are read out. However, since there is only one read, the bias is still present. As we will see, this affects the way that we correct the data for non-linearity.

2.5 Data Reduction

In this section, we discuss the procedure for the reduction of the *L*-band data. The *H*-band data obtained with STELIRCAM were reduced in an identical fashion. The *JHK* SQUID data were reduced by Elizabeth Lada using Image Reduction and Analysis Facility (IRAF) routines as described in Lada & Lada (1995). A similar method of reduction was used by João Alves for the NGC 2362 *JHK* data. The reduction of the *JHK* Trapezium data was performed by August Muench as discussed in Lada et al. (2000).

2.5.1 Reduction of the STELIRCAM Data

All *L*-band data were reduced using IRAF. With the exception of the Trapezium cluster, all STELIRCAM data was reduced as follows. First, an average dark frame was constructed from the dark frames taken at the beginning and end of each night's observations. This dark frame was subtracted from all target observations to yield dark subtracted images.

As noted in the last section, we must account for detector non-linearity. When a pixel is reset, the voltage difference between the pixel and detector substrate creates a depletion region which acts as a potential well for the collection of (mostly) photogenerated charge carriers (this can be considered a capacitor). As charge is accumulated in the pixel, the depletion region fills in, thus increasing its capacitance.

This, coupled with the steadily decreasing bias on the pixel, creates a sublinear charge-voltage relationship, which saturates when the pixel voltage reaches that of the detector substrate. Corrections for linearity are especially important for observations using broad-band filters where the integration time is limited by the sky background and where most of the data is taken at a significant fraction of the full well capacity.

The linearity properties of a given detector are determined by obtaining a linearity sequence. This is determined by taking a series of images at increasing integration times. The actual/expected count ratio is plotted against the actual counts obtained, and a linear least squares fit to the data is performed. The effects of detector non-linearity have been well characterized for STELIRCAM. We linearize our dark subtracted data by first dividing each frame by the number of coadditions used when the frame was taken, and then running these frames through a routine in IRAF called IRLINCOR. We note here that typically linearization is the first step of the data reduction process. However, since the STELIRCAM data were taken in single readout mode, the bias is still present in each frame. Dark subtraction removes this bias and allows proper linearization. The input to the IRLINCOR routine are three coefficients that were determined when the linearity of the detector was characterized. For the red array, the linearity coefficients are: $c1 = 1.0001711$, $c2 = 0.18473091$ and $c3 = 0.087063988$. For the blue array, the linearity coefficients are: $c1 = 0.99984394$, $c2 = 0.16569205$ and $c3 = 0.032897034$.

Our next step is to sky subtract all of the images. Because of the extreme sensitivity of *L*-band observations to changes in atmospheric water vapor content, sky subtraction must be done with great care. Sky frames were individually made for each observation by median combining the nearest nine frames in time to the target observation, allowing for pixel clipping (at the 3 sigma level) and median scaling to eliminate all features that are not unique to the detector (e.g., stars, nebulosity and

brightness gradients not inherent to the detector). Each sky frame was individually inspected to confirm that all stars and nebulosity had been removed by this process. The sky frames were then subtracted from the appropriate target frames.

Our images must now be divided by normalized flat fields. Flat fields are necessary to account for the detector's spatially varying response to light. The flat fields are produced directly from the sky frames. Not only is this an efficient use of the data, but any temperature changes (which can affect both the dark current and linearity) or changes in the sky conditions will also be inherent in both the target and sky frames. Each individual sky frame was normalized using the NORMALIZE task within IRAF to produce flat fields for each target frame. An examination of the resulting flat fields revealed them to be truly "flat" to within 2%. All dark and sky subtracted target frames were divided by the normalized flat fields.

It is quite common for near-infrared arrays to exhibit many bad pixels. We used the dithering technique described earlier when making observations of the target objects to prevent features from always falling on bad pixels or low-sensitivity regions of the detector. However, not all bad pixels are removed by dithering, and therefore it is necessary to create bad pixel masks. These masks are included during the final combination of the target frames.

Masks are created from both the dark frames and the flat fields. We identify all hot pixels in the dark frames, and all dead pixels that are not registering flux in the flat fields. In each case, we use the IRAF task IMREPLACE to assign a value of zero to all bad pixels and a value of one to all good pixels, thus creating two individual masks. The final mask for the target observations is created by multiplying the two individual masks created from the darks and flats.

Finally all target frames for a given position in the cluster were registered and combined (including the bad pixel mask) to produce the final image of each field. Stars common to all frames in a given field were used to calculate the offsets

between them. In some cases, no stars could be seen in the reduced frames. When this occurred, we used the *H*-band frames to calculate the offsets for each frame. All frames were shifted onto a reference frame using these offsets and were averaged together.

The observations of the Trapezium cluster were reduced in essentially the same manner as discussed above, with one major difference. All frames were first dark subtracted and linearized as discussed above. For the Trapezium data, however, the sky frames were constructed by median combining the nearest 9 *sky* positions in time to the target observations, rather than the nearest 9 *target* positions as before. The sky frames were normalized to produce flat fields for each target frame. The dark subtracted and linearized frames were then sky subtracted, flat fielded and combined to produce the final images of each field.

2.5.2 Reduction of the NSFCAM Data

The NSFCAM data were reduced in the same manner as the STELIRCAM observations (except the Trapezium), with one major difference. Linearization is not performed on the NSFCAM data since we did not have time to determine the linearity of the array. Thus observers typically keep the number of counts in each pixel at about half of the saturation value when obtaining data. In this way, the data are only a few percent non-linear. Otherwise, the procedure for dark subtraction, sky subtraction, flat fielding and registration of the individual frames for a given field is identical to that used for the STELIRCAM data.

2.6 Tests of the Near-infrared Data Reduction Procedure

In the final section of this chapter, we discuss tests of various steps in the data reduction procedure to ensure that we performed the best possible reduction. Among the steps that were tested are the sky subtraction step, flat fielding and the effect of the flat fielding on the photometry (photometry is discussed in detail in

the next chapter). These tests were performed on the data acquired at FLWO since STELIRCAM is a relatively new instrument, and we felt it necessary to more fully characterize the system. The properties of NSFCAM are already well understood.

We median combined the nearest nine frames in time to the target observation to create our sky frames for performing sky subtraction. Could we have used a smaller number of frames to create the sky frames? If the number of frames median combined together is too small, bright stars and strong nebulosity will leave imprints of themselves on the resulting sky frame. These frames will not only leave “holes” at the position of the imprints when used in the sky subtraction step, but, because the sky frames were used to make the flat fields, the flat fielding step will also be affected.

We tested the sky subtraction step using sky frames created by median combining the nearest 3 to 9 frames in time to the target observation and examining the resulting sky subtraction. Each sky frame was individually inspected for the presence of any bright stars or residual nebulosity. Stars could still be seen when fewer than 9 frames were used to create sky frames. Therefore, we concluded that a minimum of 9 frames must be used to create the sky frames for each target frame.

To test our flat fielding procedure, we observed the standard star HD 106965 in both the *H* and *L*-bands at 100 separate positions arranged in a 10×10 grid across the detector, and reduced the data using flats created using two different methods. The first method consisted of flat fields produced by normalizing the individual sky frames for each object. In the second method, a single flat field for each night was created from 18 individual sky frames taken at three separate airmasses (1.0, 1.5 and 2.0). At each airmass, the 18 separate frames were median combined to produce a single sky frame. The three resulting sky frames were subtracted and normalized to produce a single flat field.

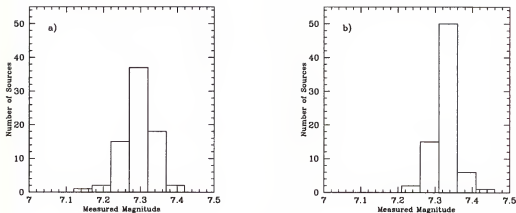


Figure 2-1: Tests of photometric reproducibility. The histograms show the reproducibility of standard star L- and H-band magnitudes as a function of location on the detector. a) L-band; b) H-band.

We performed aperture photometry of all 100 sources in the two resulting datasets, and investigated both the quality of the flat fielding and the reproducibility of the stellar photometry for the 100 target observations taken on different regions of the detector. In Figure 2-1, we show the results of the aperture photometry for each position in both filters. The bin width in both plots is 0.05 magnitudes. In each case, the distribution of the magnitudes exhibits a strong peak around the published H - and L -band magnitudes ($m_H = 7.335$ and $m_L = 7.295$) for the star, with a spread of ~ 0.1 magnitudes at H -band and ~ 0.15 magnitudes at L -band. Subtracting the average intrinsic photometric errors of 0.01 and 0.05 magnitudes at H - and L -band respectively, we are left with errors due to flat fielding of 0.09 and 0.05 magnitudes. In addition, no gradients were observed across the array. We therefore conclude that our photometry is very reproducible across the detector, and errors due to flat fielding amount to only a few percent.

CHAPTER 3 NEAR-INFRARED CALIBRATION AND SOURCE PHOTOMETRY

3.1 Near-Infrared Source Extraction and Photometry

For all of our near-infrared datasets, sources were identified using the DAOFIND routine (Stetson 1987) within IRAF. The full width at half maximum (FWHM) of the point spread function (PSF) for the SQUIID data was typically ~ 2.0 pixels while the FWHM of the PSF for the STELIRCAM and NSFCAM data ranged from 2.3 to 2.8 pixels. The DAOFIND routine was run on each individual image in each dataset using a FWHM of the PSF between 2.0 and 2.5 pixels and a single pixel finding threshold equal to 3 times the mean noise of each image. Each frame was individually inspected and the DAOFIND coordinate files were edited to remove bad pixels and any objects misidentified as stars, as well as add any missed stars to the list. For all data except the Trapezium cluster, aperture photometry was performed using the task PHOT within IRAF. We used an aperture of 4 pixels in radius for the STELIRCAM and NSFCAM photometry and a 3 pixel radius aperture for the SQUIID photometry. Aperture diameters were selected such that they were at least twice the FWHM of the PSF of the stars. The sky values around each source were determined from the mode of intensities in an annulus with inner and outer radii of 10 and 20 pixels respectively. Our choice of aperture sizes ensured that the flux from at least 90% of the stars was not contaminated by the flux from neighboring stars, however they are not large enough to include all the flux from a given source. To account for this missing flux, aperture photometry was performed on all bright, isolated sources using the same aperture used for the photometry of the standard stars, 10 pixels for each dataset. Fluxes in both the large and small apertures were compared and the

instrumental magnitudes for all sources were corrected to account for the missing flux.

Since the Trapezium cluster contains significant amounts of bright nebulosity, aperture photometry is not very reliable. Therefore, photometry of all sources in the Trapezium cluster was obtained using PSF fitting routines in the DAOPHOT package within IRAF (Stetson 1987). By using special sky fitting routines within the DAOPHOT package, PSF fitting photometry mitigates the effect of small scale variations in the background “sky” due to the extended nebulosity in the Trapezium. PSF photometry was conducted for the Trapezium cluster by August Muench, the details of which are described in Lada et al. (2000).

We note here that the NGC 2024 cluster also contains extended emission, and therefore one might question our use of aperture photometry in this cluster rather than PSF fitting. The nebulosity in the NGC 2024 cluster is much fainter than in the Trapezium, and contributes very little flux to the aperture photometry. Indeed, as we discuss later, the completeness limit of our NGC 2024 data is the same in regions with and without extended emission. Thus our choice of aperture photometry for the NGC 2024 cluster is validated.

3.2 Photometric Calibration

Photometric calibration of all near-infrared datasets, from both STELIRCAM and NSFCAM, was accomplished using the list of standard stars of Elias et al. (1982). The standards were observed on the same nights, and through the same range of airmasses, as the cluster fields. Aperture photometry was performed on all standards using an aperture of 10 pixels in radius. This aperture size was selected to extend to where the stellar profiles blend with the background noise.

For all clusters except the Trapezium, zero points and extinction coefficients were established for each filter for a given night using the FITPARAMS task within

IRAF. Three separate files are input to this task: (1) a file containing the true magnitudes and errors for all standard stars from the Elias et al. (1982) list, (2) a file containing the star name, airmass, instrumental magnitude and photometric error for each standard star measured using PHOT, and (3) a file containing the transformation equation fitted to the data. The best fit line to the data was examined. Any points that were found to lie off this line by more than their intrinsic photometric errors were rejected and the line fit again. In Table 3-1, we present the photometric solutions for all STELIRCAM *L*-band data. Table 3-2 lists the photometric solutions for the NSFCAM *L*-band data. In both tables, we list the date of observation, standards used in the final fit, zero points (in magnitudes), and extinction coefficients (in magnitudes/airmass). The zero point and airmass corrections were applied to the instrumental, aperture corrected magnitudes determined from PHOT to yield the true magnitudes of all sources in the clusters.

No *L*-band standards were obtained for the Trapezium data. The *L*-band photometry was therefore calibrated internally using 34 stars whose *L*-band magnitudes were independently obtained from the February 2000 IRTF observations. The resulting uncertainty in the calibrated photometry was 0.05 magnitudes. We checked our internal calibration by comparing observations of 14 stars within the mosaicked image for which there existed previous *L*-band photometry from the literature. The magnitudes of these stars agreed to within the 0.05 magnitude calibration uncertainty.

3.3 Near-Infrared Photometric Accuracy

We can test the reliability of the stellar photometry for each cluster by investigating its internal consistency. This is accomplished by examining the reproducibility of the photometry for stars in the overlap regions of the different cluster fields. In Figure 3-1, we plot the STELIRCAM *L*-band photometry for all duplicate stars in

Table 3-1: Photometric Solutions for STELIRCAM *L*-Band Data

Date (UT)	Standards Fit	Zero Point (mag)	Ext. Coeff. (mag/am)
01/06/98	HD 22686, 40335	18.318 ± 0.050	-0.110 ± 0.035
01/07/98	HD 22686, 40335	18.226 ± 0.099	-0.050 ± 0.070
01/08/98	HD 22686, 40335	18.189 ± 0.092	-0.096 ± 0.070
12/03/98	HD 22686, 40335	18.193 ± 0.063	-0.090 ± 0.046
12/04/98	HD 22686, 40335	18.109 ± 0.089	-0.031 ± 0.070
12/07/98	HD 22686	18.300 ± 0.043	-0.143 ± 0.028
01/26/99	HD 22686, 40335	18.283 ± 0.092	-0.144 ± 0.070
01/27/99	HD 22686, 40335	18.296 ± 0.020	-0.167 ± 0.014
01/29/99	HD 22686, 40335	17.853 ± 0.102	0.139 ± 0.080
01/30/99	HD 22686, 40335	18.304 ± 0.021	-0.140 ± 0.015
02/01/99	HD 22686, 40335	18.042 ± 0.118	-0.034 ± 0.094
02/02/99	HD 22686	18.318 ± 0.215	-0.101 ± 0.175
11/22/99	HD 22686, 40335	18.337 ± 0.012	-0.117 ± 0.008
11/23/99	HD 22686, 40335	18.280 ± 0.038	-0.121 ± 0.026
11/24/99	HD 22686	18.590 ± 0.066	-0.337 ± 0.047
11/25/99	HD 22686	18.888 ± 0.189	-0.662 ± 0.152
11/26/99	HD 22686, 40335	18.526 ± 0.116	-0.380 ± 0.089
01/14/00	HD 22686, 40335, 77281	18.464 ± 0.165	-0.375 ± 0.135

Photometric Solutions for STELIRCAM *L*-Band Data. The columns are as follows: (1) Observation Date, (2) standard star(s), (3) zero points in magnitudes, and (4) extinction coefficients in magnitudes/airmass.

Table 3-2: Photometric Solutions for NSFCAM *L*-Band Data

Date (UT)	Standards Fit	Zero Point (mag)	Ext. Coeff. (mag/am)
02/06/00	HD 22686, 40335	20.375 ± 0.006	-0.105 ± 0.006
02/07/00	HD 22686, 40335	20.402 ± 0.065	-0.181 ± 0.053
02/08/00	HD 40335	20.621 ± 0.271	-0.398 ± 0.237

Photometric Solutions for NSFCAM *L*-Band Data. The columns are as follows: (1) Observation Date, (2) standard star(s), (3) zero points in magnitudes, and (4) extinction coefficients in magnitudes/airmass.

the NGC 2024, NGC 2071 and NGC 2068 clusters. In Figure 3-2, we show the accuracy of the STELIRCAM *L*-band photometry for the IC 348, NGC 2264 and NGC 1960 clusters, as well as the NSFCAM *L*-band photometry of NGC 2362. In both figures, the stellar magnitudes in one of the overlap frames are plotted against the difference in magnitudes between the two overlapping frames. A comparison of the *L*-band magnitudes for thirty-one stars from our STELIRCAM and NSFCAM surveys of NGC 2024 is shown in Figure 3-3. As discussed in Lada et al. (2000), the photometry of the Trapezium cluster was done on the entire mosaic, and therefore no overlap regions are defined. Recall, however, that comparisons of the photometry, both internally and with the literature, agreed to within 0.05 magnitude. Inspection of Figures 3-1 and 3-2 reveals very good agreement between the duplicate star magnitudes in each cluster. Indeed, for our entire STELIRCAM *L*-band survey, 67% of the stars have magnitudes that differ by ≤ 0.1 magnitude and 88% have magnitudes that differ by ≤ 0.2 magnitude. Inspection of Figure 3-3 shows that our STELIRCAM and NSFCAM *L*-band photometry for NGC 2024 agrees to ≤ 0.2 magnitude. Similar tests of the accuracy of the *JHK*-band photometry for each cluster shown in Figure 3-1 were performed by Elizabeth Lada and João Alves, and all photometry agrees to $\leq 10\%$. The STELIRCAM and NSFCAM photometry is found to agree to within ~ 0.15 magnitude. The *JHK_s*-band data from the 2MASS archive has a photometric accuracy of 0.155 magnitude in each band.

3.4 Completeness Limits for Near-infrared Data

The completeness limits of all observations were determined by adding artificial stars to each of the images and counting the number of sources recovered by DAOFIND. In regions where source crowding was not a problem, artificial stars were added at random positions to each image in ten separate half magnitude bins with each bin containing one hundred stars. The ten bins covered a magnitude range

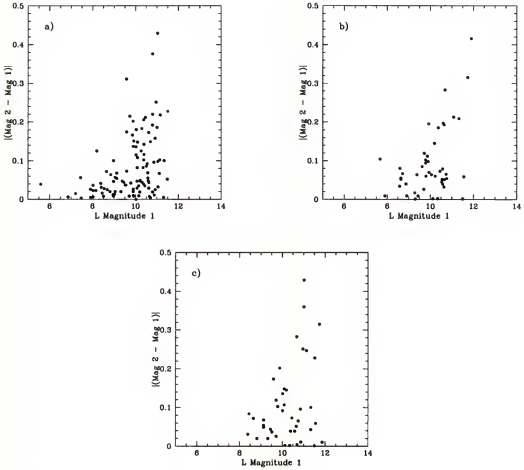


Figure 3-1: Accuracy of the L -band photometry for the Orion clusters. Plots are shown for the photometry of the stars in the overlap regions of the a) NGC 2024, b) NGC 2071 and c) NGC 2068 clusters.

from 10.0 to 15.0. The artificial stars were examined to ensure that they had the same FWHM of the PSF as the real sources in the image.

Aperture photometry was performed on all sources to confirm that the magnitudes assigned to the added sources agreed with those returned by PHOT. All photometry agreed to within 0.1 magnitude. The DAOFIND and PHOT routines were then run and the number of identified artificial sources within each half magnitude bin was tallied. This process was repeated 20 times. In the central regions of the NGC 2024 cluster, where source crowding was a concern, fifty sources were added

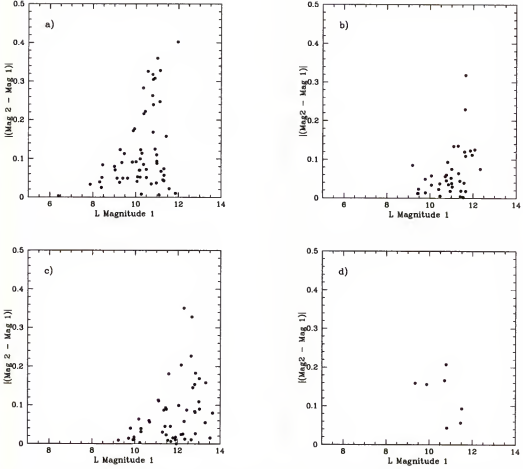


Figure 3-2: Accuracy of the L -band photometry for the older clusters. These clusters have ages ≥ 2 Myr. Plots are shown for the photometry of the stars in the overlap regions of the a) IC 348, b) NGC 2264 South, c) NGC 2362 and d) NGC 1960 clusters.

at random positions to each image. The procedure for estimating the completeness limit was the same as described above, however the process was repeated 40 times.

In Figures 3-4 to 3-7, we show histograms of the completeness for the JHK -band SQUIID and NGC 2264 STELIRCAM data, and the L -band STELIRCAM and NSFCAM data respectively. A summary of the completeness limits for each cluster is given in Table 3-3. The identification of sources in our SQUIID survey, averaged over regions without nebulosity, is estimated to be 90% complete to $m_J=16.5$, $m_H=15.5$, and $m_K=14.5$. In the central 18% of the NGC 2024 cluster, where nebulosity is a concern, the completeness limits are 0.5 magnitudes brighter at J, H , and

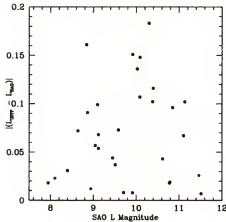


Figure 3-3: Comparison of the L -band STELIRCAM and NSFCAM photometry in NGC 2024. The magnitudes of thirty-one stars in the cluster are compared. All photometry agrees to within ~ 0.15 magnitude.

K -bands. The completeness limits for the NGC 2264 JHK STELIRCAM data are: $m_J=18.0$, $m_H=17.0$ and $m_K=16.0$. For our STELIRCAM L -band data, the estimated 3 and 18 minute integration completeness limits are $m_L=12.0$ and $m_L=13.0$ ($m_L=12.5$ for NGC 2264) respectively, while our NSFCAM observations are complete to $m_L=14.0$. The JHK -band and JHK_s -band completeness limits listed in Table 3-3 for the Trapezium, NGC 2264, NGC 2362 and NGC 1960 clusters were obtained from August Muench (Trapezium), João Alves (NGC 2362) and the 2MASS home page (<http://pegasus.astro.umass.edu>) respectively.

3.5 Astrometry of the Near-infrared Data

Absolute α and δ positions were determined for all L band sources in each cluster, and matched with existing JHK coordinates. A centering algorithm within APPHOT was used to obtain center positions for the sources in pixels. Many sources were present in the overlap regions of each cluster field. Duplicate stars on adjacent frames were used to register the relative pixel positions of the individual frames in each cluster onto a single positional grid. Pixel positions were converted to equatorial

Table 3-3: Cluster Completeness Limits

Cluster	<i>J</i>	<i>H</i>	<i>K</i>	<i>L</i>	References
NGC 2024	16.5	15.5	14.5	12.0, 13.0, 14.0	1
NGC 2024 inner 18%	16.0	15.0	14.0		1
NGC 2071	16.5	15.5	14.5	12.0	2
NGC 2068	16.5	15.5	14.5	12.0	2
Trapezium	18.5	17.7	16.8	12.0	3
IC 348	16.5	15.5	14.5	12.0	4
NGC 2264	18.0	17.0	16.0	12.5	5
NGC 2362	18.0	17.0	16.0	14.0	5
NGC 1960	15.8	15.1	14.3	13.0	5

Cluster Completeness Limits. The *J*, *H*, *K* and *L*-band completeness limits for our sample clusters. The columns are as follows: (1) Cluster name, (2) *J*-band completeness limit, (3) *H*-band completeness limit, (4) *K*-band completeness limit, (5) *L*-band completeness limit, and (6) Reference for photometry. The multiple *L*-band completeness limits quoted for NGC 2024 correspond to the STELIRCAM 3 and 18 minute and NSFCAM surveys respectively. NOTE: References for photometry are as follows: (1) Haisch, Lada, & Lada (2000), (2) Dahari & Lada (2001), (3) Lada et al. (2000), (4) Haisch, Lada, & Lada (2001), and (5) Data obtained from August Muench, João Alves and 2MASS (<http://pegasus.astro.umass.edu>).

coordinates using the positions of the brightest stars in each cluster as references, and the known plate scales of 0.6"/pixel, and 0.3"/pixel for STELIRCAM and NSFCAM respectively. A comparison of the *JHK* and *L* source coordinates yields an agreement to within 1". A check was also made by eye to ensure that the stars were correctly paired up. Therefore, we are quite certain of the stellar matches between the datasets.

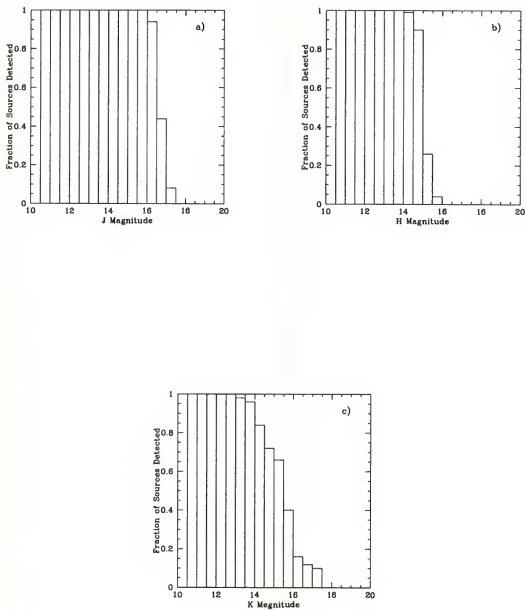
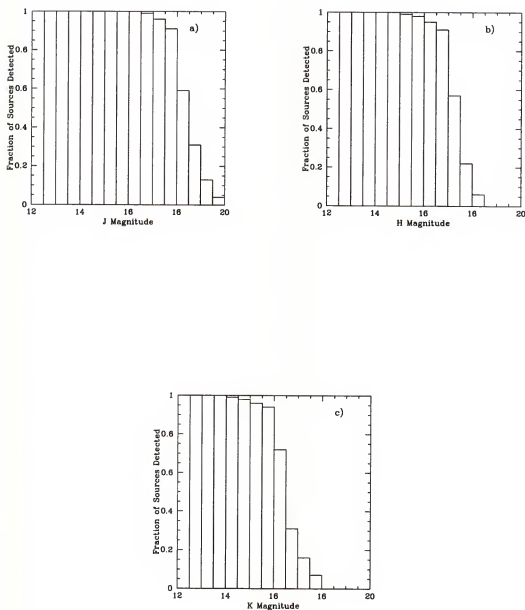


Figure 3-4: Completeness limits of the SQUID data. The plots are labelled as a) *J*-band, b) *H*-band and c) *K*-band. The completeness limits in each filter are m_J , m_H , $m_K=16.5$, 15.5 , and 14.5 respectively.



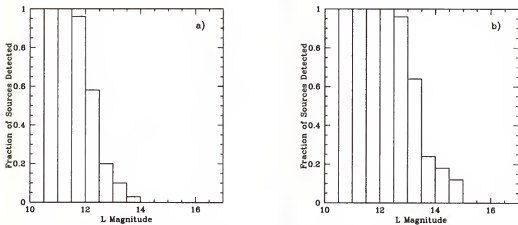


Figure 3-6: Completeness limits of the STELIRCAM data. The plots are labelled as a) 3 minute and b) 18 minute STELIRCAM L -band data. The completeness limits at 3 and 18 minutes are $m_L=12.0$ and 13.0 respectively.

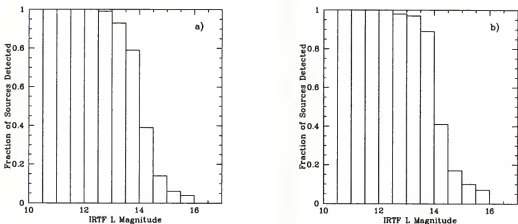


Figure 3-7: Completeness limits of the IRTF data. The plots are labelled as a) NGC 2024 and b) NGC 2362 IRTF L -band data. The observations for both clusters are complete to $m_L=14.0$.

CHAPTER 4 THE TRAPEZIUM AND NGC 2024 CLUSTERS

4.1 Results and Spatial Distribution

We detected 257 and 107 sources in NGC 2024 at L -band with STELIRCAM to the completeness limits of our ~ 110 and ~ 20 arcmin² surveys ($m_L=12.0$ and 13.0 respectively). All of these sources were detected in at least one other band (typically K -band). Within the same area covered by our STELIRCAM observations (~ 110 arcmin²), we detected a total of 286 J -band sources ($m_J<16.5$), 311 H -band sources ($m_H<15.5$) and 343 K -band sources ($m_K<14.5$) in our SQIID survey. Our NSFCAM observations of the central ~ 6.25 arcmin² region of the NGC 2024 cluster reveal 26 additional sources with $12.0<m_L<14.0$. Four of these had $12.0<m_L<13.0$, and were thus detected in our ~ 20 arcmin² STELIRCAM survey region. Of the 26 additional sources detected with NSFCAM, 20 sources were not detected to the completeness limit of our SQIID observations. However, Levine, Lada, & Elston (2000, in preparation) recently obtained K -band tip-tilt data of the NGC 2024 cluster using the 4m telescope at Cerro Tololo Interamerican Observatory (CTIO). This dataset extends to a K -band completeness limit of $m_K\simeq 16.5$. From these observations, we can identify K -band counterparts for all but one of the NSFCAM L -band sources.

Within the region surveyed in the Trapezium cluster, we detected 548 L -band sources ($m_L<12.0$), 779 K -band sources ($m_K<16.8$), 695 H -band sources ($m_H<17.7$) and 600 J -band sources ($m_J<18.5$) to our completeness limits. Of these, 595 were simultaneously detected at JHK , 490 simultaneously at $JHKL$ and 46 at HK . Five of the sources were detected only at L -band. A summary of all source detections is given in Table 4-1.

Table 4-1: Number of Source Detections in Each Filter

Cluster	<i>J</i>	<i>H</i>	<i>K</i>	<i>L</i>
NGC 2024	286	311	343	257, 107, 133
Trapezium	600	695	779	548

Number of Source Detections in Each Filter. The number of *J*, *H*, *K* and *L*-band sources detected to the completeness limits in the NGC 2024 and Trapezium clusters. The columns are as follows: (1) Cluster name, (2) number of *J*-band sources, (3) number of *H*-band sources, (4) number of *K*-band sources, and (5) number of *L*-band sources detected. The multiple *L*-band source numbers quoted for NGC 2024 correspond to the STELIRCAM 3 and 18 and NSFCAM surveys respectively.

In Figure 4-1, we present an *L*-band mosaic and a *JHK* color mosaic of the NGC 2024 cluster. These images are displayed with north at the top and west on the right. The spatial distribution of all sources to $m_K=14.5$ in our SQIID/STELIRCAM survey is shown in Figure 4-2 (a). Sources that are detected at both *K*- and *L*-bands are plotted using a point while those sources that are visible only at *K*-band in our SQIID data are shown with a star. A slight central condensation of sources may be present, otherwise the distribution is fairly uniform with no obvious differences in the locations of sources detected and not detected at *L*-band. In Figure 4-2 (b), we plot the inner $2' \times 2'$ region of the cluster observed in our NSFCAM survey. All sources that were detected to the SQIID completeness limit in the central frame ($m_K=14.0$) are shown by a point. Sources having *K*-band magnitudes fainter than $m_K=14.0$ (obtained from Levine et al. (2000, in preparation)) are shown by a triangle. A star denotes the position of the source detected only at *L*-band.

Figure 4-3 (a) shows an *L*-band mosaic of the Trapezium cluster. Extended emission is observed throughout the region with the well known bright bar prominent in the southeast. Figure 4-3 (b) shows a *JHK* false color mosaic with *K*-band coded red, *H*-band coded green and *J*-band coded blue. In both mosaics, the Trapezium stars are visible in the center of the fields. The spatial distribution of all cluster members is shown in Figure 4-4. Cluster members are shown as open circles and

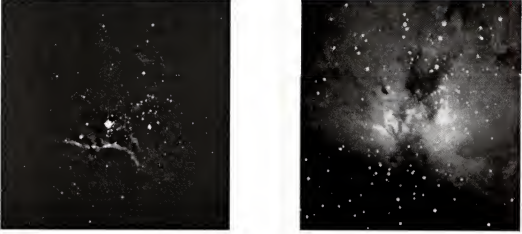


Figure 4-1: The *JHKL* images of the NGC 2024 cluster. The a) *L*-band and b) *JHK* color mosaics of the NGC 2024 cluster are displayed with north at the top and west toward the right. In the *JHK* image, *K*-band emission is color coded as red, *H*-band emission as green and *J*-band emission as blue.

candidate protostellar objects (discussed below) are shown as filled circles. The protostellar candidates appear more spatially confined than the cluster population as a whole. Also labelled in Figure 4-4 are bright stars with spectral types of B3 and earlier (large white stars) and sources detected only in the *L*-band (filled stars).

4.2 Color-Color Diagrams

In Figure 4-5, we present the *JHK* and *JHKL* color-color diagrams for the NGC 2024 cluster. Figure 4-6 shows the *JHK* and *JHKL* color-color diagrams for the Trapezium cluster. In the diagrams, we included only those 142 and 391 sources in NGC 2024 and the Trapezium respectively, with *K*-band magnitudes equal to or brighter than the completeness limit of our STELIRCAM *L*-band surveys (i.e., $m_K \leq 12.0$). Examining only those sources for which we are sensitive to stellar photospheres (i.e., $K - L = 0.0$), allows meaningful comparisons between the color-color diagrams to be made for the purpose of obtaining the fraction of the sources having an infrared excess, and thus the circumstellar disk fractions (see Section 4.3). Figure 4-7 presents the *JHK* color-color diagram for the 77 SQUID control field sources that

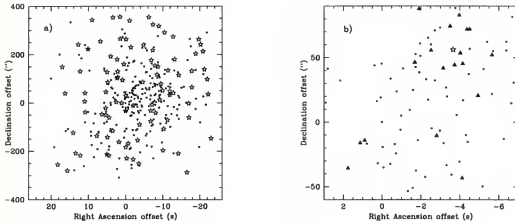


Figure 4-2: Source distribution in NGC 2024. a) The distribution of K -band sources to the completeness limit of our SQIID survey ($m_K=14.5$) in NGC 2024. Positions of sources detected at both K - and L -bands are plotted with a point while sources detected only at K -band are shown with a star. The offsets are referred to the position $\alpha=5^h39^m13^s.79$, $\delta=-1^\circ55'56''.68$ (1950). b) The distribution of sources from our NSFCAM L -band survey. Positions of sources detected that are brighter than our SQIID completeness limit for the central frame ($m_K=14.0$) are plotted with a point while sources having magnitudes fainter than $m_K=14.0$ are shown with a star. A triangle is used to denote the position of the NSFCAM source detected only at L -band.

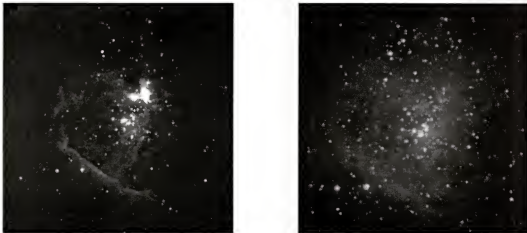


Figure 4-3: The JHK images of the Trapezium cluster. The a) L -band and b) JHK color mosaics of the Trapezium cluster are displayed with north at the top and west toward the right. In the JHK image, K -band emission is color coded as red, H -band emission as green and J -band emission as blue.

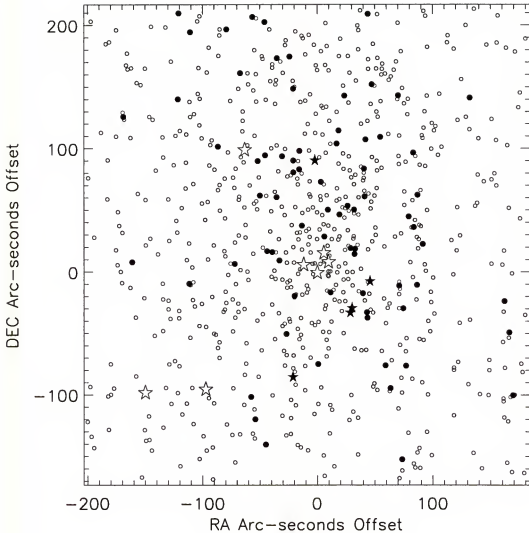


Figure 4-4: Source distribution in the Trapezium cluster. Spatial distributions of cluster members (open circles) and candidate protostars (filled circles). The protostellar candidates appear to be more spatially confined than the main cluster population. Large white stars denote the bright stars with spectral types of B3 and earlier. Filled black stars label the positions of sources detected only at L -band. Figure adapted from Lada et al. (2000).

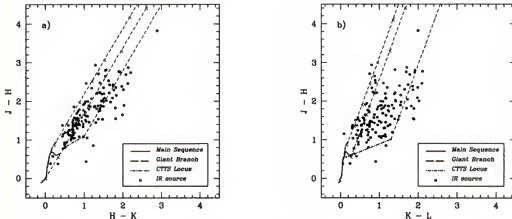


Figure 4-5: The JHK and $JHKL$ color-color diagrams for NGC 2024. The diagrams are shown as a) JHK and b) $JHKL$. Only those sources extracted from our SQUIID survey with $m_K \leq 12.0$ and $JHKL$ photometric errors less than 10% are plotted. In the diagrams, the locus of points corresponding to the unreddened main sequence is plotted as a solid line, the locus of positions of giant stars is shown as a heavy dashed line and the CTTS locus as a dot-dashed line. The two leftmost dashed lines define the reddening band for main sequence stars and are parallel to the reddening vector. Crosses are placed along these lines at intervals corresponding to 5 magnitudes of visual extinction. The rightmost dashed line is parallel to the reddening band.

match the above criteria. In all of the color-color diagrams, we plot the locus of points corresponding to the unreddened main sequence as a solid line and the locus of positions of giant stars as a heavy dashed line (Bessell & Brett 1988). The two leftmost parallel dashed lines define the reddening band for main sequence stars and are parallel to the reddening vector. Crosses are placed along these lines at intervals corresponding to 5 magnitudes of visual extinction. The classical T Tauri star (CTTS) locus is plotted as a dot-dashed line (Meyer, Calvet, & Hillenbrand 1997). The reddening law of Cohen et al. (1981), derived in the CIT system and having slopes in the JHK and $JHKL$ color-color diagrams of 1.692 and 2.750 respectively, was adopted.

4.2.1 Average Extinction

Clear differences exist between the JHK cluster and control field diagrams. The stars in the JHK control fields are tightly concentrated near the unreddened

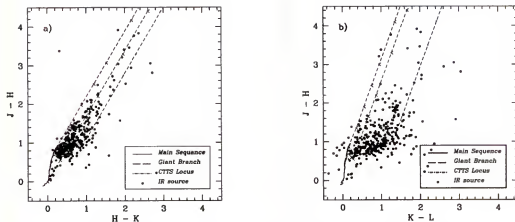


Figure 4-6: The JHK and $JHKL$ color-color diagrams for the Trapezium. The diagrams are shown as a) JHK and b) $JHKL$. Only those sources extracted from our SQUID survey with $m_K \leq 12.0$ and $JHKL$ photometric errors less than 10% are plotted. In the diagrams, the locus of points corresponding to the unreddened main sequence is plotted as a solid line, the locus of positions of giant stars is shown as a heavy dashed line and the CTTS locus as a dot-dashed line. The two leftmost dashed lines define the reddening band for main sequence stars and are parallel to the reddening vector. Crosses are placed along these lines at intervals corresponding to 5 magnitudes of visual extinction. The rightmost dashed line is parallel to the reddening band.

main sequence with spectral types corresponding to late G to late M stars. A smaller portion of stars are found around the giant branch. This indicates that the control fields consist of field stars that possess very little interstellar reddening. In contrast, the stars in the NGC 2024 and Trapezium clusters are displaced from the main sequence and spread over a larger area of the reddening band. This displacement is due to extinction by the molecular cloud associated with each cluster. Comparison of the mean $H-K$ colors of the cluster and control field stars yields an average extinction of $A_V = 10.4 \pm 1.9$ for all sources in the reddening band of the JHK color-color diagram for NGC 2024 and $A_V = 6.0 \pm 1.1$ for the Trapezium. Furthermore, the spread of the cluster stars within the reddening band indicates that there is differential extinction with a range corresponding to roughly 0 to 30 visual magnitudes. This range in extinction toward each cluster, combined with the fact that statistically most of the stars observed in the cluster field are actual cluster members (as determined from K -band luminosity function studies of each cluster (Hillenbrand 1997; Dahari & Lada 2000, in preparation), suggests that our estimate of the extinction to the background stars is likely an underestimate and that the cluster stars themselves are typically extinguished by $A_V \simeq 10.5$ and 6.0 in the NGC 2024 and Trapezium clusters respectively.

4.2.2 Near-Infrared Excess Fractions

A significant fraction of the NGC 2024 and Trapezium cluster sources fall outside and to the right of the reddening lines in the infrared excess region of the color-color diagrams. In the $JHKL$ diagram, a total of 112/142 (79% \pm 8%) and 312/391 (80% \pm 7%) of the sources in NGC 2024 and the Trapezium respectively lie in the infrared excess region. Inspection of the JHK color-color diagram for the cluster reveals a smaller fraction of infrared excess sources. Indeed, 76/142 (54% \pm 6%) and 195/391 (50% \pm 7%) of the NGC 2024 and Trapezium sources respectively lie in the infrared excess region of the JHK diagram.

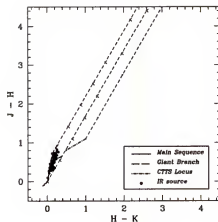


Figure 4-7: The JHK color-color diagram for the SQUIID control fields. Only those sources extracted from our SQUIID and STELIRCAM surveys with $m_K \leq 12.0$ and $JHKL$ photometric errors less than 10% are plotted. In the diagram, the locus of points corresponding to the unreddened main sequence is plotted as a solid line, the locus of positions of giant stars is shown as a heavy dashed line and the CTTS locus as a dot-dashed line. The two leftmost dashed lines define the reddening band for main sequence stars and are parallel to the reddening vector. Crosses are placed along these lines at intervals corresponding to 5 magnitudes of visual extinction. The rightmost dashed line is parallel to the reddening band.

Table 4-2: Background Corrected Excess Fractions for the NGC 2024 Cluster

Area (arcmin ²) ²	<i>JHK</i> Fraction	<i>JHKL</i> Fraction
Complete $m_L = 12.0$ ³		
110.25	76/131 (58±7%)	112/131 (86±8%)
20.25	58/82 (71±9%)	68/82 (83±10%)
6.25	28/32 (88±17%)	30/32 (94±17%)
Complete $m_L = 13.0$ ⁴		
20.25	58/90 (64±9%)	76/90 (84±10%)
6.25	33/38 (87±15%)	36/38 (95±16%)
Complete $m_L = 14.0$ ⁵		
6.25	34/38 (90±15%)	33/38 (87±15%)

²Area centered on the cluster for which infrared excess fractions were determined.

³Completeness limit for 3 minute SAO data.

⁴Completeness limit for 18 minute SAO data.

⁵Completeness limit for IRTF data.

We must correct these fractions for field star contamination. Because we are only considering those stars to $m_K=m_L=12$, the correction is the same for the *JHK* and *JHKL* fractions. We first consider the NGC 2024 cluster. The foreground/background contamination was determined by first counting the total number of stars observed in the control fields to $m_K=12$. Scaling this number to the cluster area observed and accounting for the average extinction in NGC 2024 ($A_K \simeq 1.0$ magnitudes), we find a field star contamination of eleven stars. Applying this correction to the infrared excess fractions, we estimate that $86\% \pm 8\%$ and $58\% \pm 7\%$ of the sources in the NGC 2024 cluster have respective *JHKL* and *JHK* colors suggestive of infrared excess emission. A similar difference in the *JHKL* and *JHK* excess fractions ($84\% \pm 10\%$ versus $64\% \pm 9\%$) is observed in our deeper ($m_K=m_L=12.9$) STELIRCAM data. On the other hand, the *JHKL* and *JHK* excess fractions are the same within the errors ($90\% \pm 15\%$ and $87\% \pm 15\%$) for our NSFCAM survey that covers a much smaller region and extends to $m_K=m_L=14.0$ (the completeness limit in the central region of the cluster). A list of the *JHK* and *JHKL* infrared excess fractions for the three areas and completeness limits of our survey is given in Table 4-2.

In the Trapezium cluster, an examination of the control fields suggests that field star contamination by sources with $m_K \leq 12.0$ is insignificant, especially given the large extinction provided by the Orion Molecular Cloud. Thus the excess fractions we measured correspond to the excess fractions of the cluster membership.

The derived fraction of excess sources is sensitive to the location of the boundary of the reddening band. This depends on the adopted intrinsic colors of the latest spectral type stars. The dwarf main sequence colors used by different authors become disparate at the latest spectral types, starting at about M3 (e.g., Koornneef 1983; Bessell & Brett 1988). By spectral type M5, a comparison of the $H - K$ and $K - L$ colors from Koornneef (1983) and Bessell & Brett (1988) yields differences of 0.03 and 0.11 magnitudes respectively. Our derived excess fractions were calculated assuming the boundary of the reddening band in the $JHKL$ and JHK diagrams passes through M5 and A0 colors from Bessell & Brett (1988) respectively. We used A0 rather than M5 colors in the JHK diagram because if one extends the righthand reddening line from an M5 spectral class toward bluer colors, some of the earlier type main sequence stars fall in the infrared excess region of the diagram. This reddening line extends through main sequence colors that are somewhat later than M5.

We consider the $JHKL$ fractions as derived above to be a lower limit on the true excess fractions. In NGC 2024, the average extinction in the cluster is $A_K \simeq 1.0$, and therefore the unextincted magnitudes of the sources at the completeness limit of our largest survey region are in fact $m_K = 11.0$ rather than $m_K = 12.0$. At the distance and age of NGC 2024 (~ 1 Myr), this implies spectral types of M0 to M3 from K -band luminosity function models (A. Muench, private communication). This is consistent with the near-infrared spectral types from Meyer (1996) for 33 sources having $m_K \leq 12.0$. All sources had spectral classes earlier than M4 (including errors in spectral type). If we assume M4 colors for the right-hand reddening vector, the $JHKL$ fraction in our largest survey region increases to $92 \pm 8\%$.

In the Trapezium cluster, published spectral types are available for 283 stars within our survey region (Hillenbrand et al. 1998). The vast majority (84%) of these spectroscopically observed stars are characterized by spectral types of M3 and earlier, similar to that in NGC 2024. Again because we set the boundary of the reddening band at M5 colors, we likely underestimate the true excess fraction. The fraction of stars with spectral types from O to M3 that fall in the infrared excess region of the *JHKL* color-color diagram is $84\% \pm 8\%$.

The magnitude and frequency of near-infrared excess sources determined from color-color diagrams also depends on the adopted reddening law and to a lesser extent on the photometric system used to plot the positions of the main sequence stars and the reddening bands. Our adopted reddening law of Cohen et al. (1981) is strictly true for the CIT photometric system, because this is the system in which this reddening law was derived. For each cluster, we determined *JHK* and *JHKL* excess fractions for two other reddening laws (obtained in different photometric systems)[Koornneef 1983; Rieke & Lebofsky 1985]. In our largest survey area in NGC 2024, we find *JHKL* excess fractions of $58\% \pm 7\%$ and $57\% \pm 7\%$ and *JHK* excess fractions of $85\% \pm 8\%$ and $82\% \pm 8\%$ respectively. In the Trapezium cluster, we find *JHKL* excess fractions of $50\% \pm 7\%$ and $49\% \pm 7\%$ and *JHK* excess fractions of $78\% \pm 7\%$ and $75\% \pm 7\%$ respectively. Within the quoted (statistical) errors, these fractions are the same as those we derived using a Cohen et al. (1981) reddening law. In summary, although the *absolute* excess fractions derived for a given cluster will depend somewhat on the choice of the boundary, comparisons of the *apparent* excess fractions with other clusters are valid as long as we are consistent in selecting reddening laws and main sequence colors, and as long as the reddening law is the same for the clusters being compared. This latter condition is likely to hold because at infrared wavelengths, the extinction law is generally not observed to vary from place to place in the Galaxy (Mathis 1990).

Finally, we note that photometry at L -band might be affected for heavily obscured sources if the source spectrum contains a $3.08\ \mu\text{m}$ ice absorption feature. The effects of this feature on near-infrared photometry were investigated by a number of authors (e.g., Whittet et al. 1988; Sato et al. 1990; Aspin et al. 1994; Aspin & Sandell 1997). The ice feature suppresses the flux in the L -band, thereby making the $K - L$ color too blue. In the NGC 2024 and Trapezium clusters, most of the stars are extinguished by $A_V \leq 15$ magnitudes. Sato et al. (1990) defined an empirical relationship between the optical depth of the ice feature, τ_{ice} , and A_V for the Taurus region, namely: $\tau_{ice} = 0.093(A_V - A_{vc})$, where $A_{vc} = 1.6$. Under the assumption that this equation is valid in the Orion Molecular Clouds, we find that most of the stars in the cluster have $\tau_{ice} \leq 1.25$. Aspin & Sandell (1997) calculated the narrow-band L magnitude correction due to ice absorption in the NGC 1333 cluster using the Sato et al. (1990) τ_{ice} - A_V relation. For a source with $\tau_{ice} = 1.25$, the narrow-band L correction is ~ 0.30 magnitude. The correction to our broad-band L photometry in NGC 2024 and the Trapezium is even smaller due to the increased continuum flux from the stellar source, which would dilute the line strength of the ice feature relative to that observed in a narrow-band L filter. We therefore do not expect the ice feature to produce a large effect on our L -band photometry. Nevertheless, we consider the excess fractions quoted above to be lower limits, and the true $JHKL$ excess fraction may be somewhat higher.

4.2.3 Sources with Anomalous $K - L$ Colors

In the $JHKL$ color-color diagrams, approximately 4 sources (3% of the sample) in NGC 2024 and 27 sources (7% of the sample) in the Trapezium have colors that place them in the “forbidden” regions either to the left of the main sequence reddening band or to the right and below the CTTS locus. Typical causes for the presence of stars in these forbidden regions are source variability and large photometric errors. In NGC 2024, none of the 4 anomalous sources have large photometric errors. Of

the 27 anomalous sources in the Trapezium, five are near our L -band detection limit, and likely characterized by relatively large photometric L -band errors. Most of these sources are in the forbidden zone to the left of the main sequence reddening band. Therefore, large photometric errors account for at least one-fifth of the anomalous sources in the Trapezium.

Because the L -band observations were taken a year or more after the JHK data, source variability could also cause a star's placement in one of the forbidden regions. To test this possibility in NGC 2024, we compared the JHK magnitudes of the 40 sources in common to both our survey and that of Meyer 1996. Less than 10% were found to have magnitudes that differed by more than 0.2 magnitudes in all three bands. This can account for all the sources with anomalous colors in our $JHKL$ color-color diagram. In the Trapezium, we compared our JHK observations with those in the compilation of Hillenbrand et al. (1998). Of the 256 sources with JHK magnitudes in both our catalog and the Hillenbrand et al. (1998) compilation, 25 (10%) had fluxes that differed in all three bands by more than 0.2 magnitudes. Of these, 12 (5%) differed by more than 0.5 magnitudes in all three bands. Thus, source variability could be responsible for placing as many as 5% to 10% of the sources in the Trapezium cluster in the anomalous regions of the $JHKL$ color-color diagram, and could account for all the sources with anomalous colors in the $JHKL$ diagram. In addition, in both the NGC 2024 and Trapezium clusters, variability would cause an equal number of sources to be pushed into the forbidden and excess regions of the color-color diagrams. However, the vast majority of the sources in both clusters exhibit infrared excesses. Finally, variability has a negligible effect on the infrared excesses found in other star forming regions (e.g., Barsony et al. 1997; Herbst et al. 2000; Lada et al. 2000, in preparation). Therefore, we find it very unlikely that source variability is a major factor in producing infrared excesses in both clusters.

4.2.4 Infrared Excess Fraction as a Function of Cluster Radius

In Figures 4-8(a) and (b), we present the infrared excess fractions determined from both *JHKL* and *JHK* color-color diagrams as a function of projected cluster radius as determined from our $m_K=m_L=12.0$ completeness limit data in NGC 2024 and the Trapezium. The diagrams were constructed by calculating the excess fractions in successively larger areas, increasing the projected radius by 0.1 pc each time. The excess fractions were corrected for field star contamination. The dot-dashed line indicates the excess fraction as determined from the *JHKL* colors while the dashed line represents the excess fraction determined from the *JHK* colors. The error bars indicate \sqrt{N} errors in the excess fractions. In both NGC 2024 and the Trapezium, the *JHKL* infrared excess fractions as a function of projected cluster radius are the same to within the errors. In the Trapezium, there is a decrease in the *JHK* excess fraction with projected cluster radius, but it is not significant to within the errors. In NGC 2024, the decrease observed in the *JHK* excess fractions is significant. The excess fraction declines out to a radius of ~ 0.4 pc, and remains constant thereafter. These trends in the infrared excess fractions with projected cluster radius also hold if we consider the case in which the extinction in the outer regions of the cluster is lower than that near the center (e.g., $A_V=5$ magnitudes rather than the average for the cluster of $A_V \sim 10$ magnitudes); that is, if the correction for background star contamination were larger in the outer regions of the cluster than in the inner regions.

4.2.5 Distribution of $K-L$ Colors

In Figure 4-9, we present the $K-L$ frequency distributions for the NGC 2024 (185 sources) and Trapezium (603 sources) clusters for which $K-L$ colors could be determined. The shaded region in the NGC 2024 distribution represents those sources in our NSFCAM survey for which K -band magnitudes were obtained from Levine et al. (2000, in preparation) (i.e., $14.0 < m_K < 16.5$). The shaded region in the

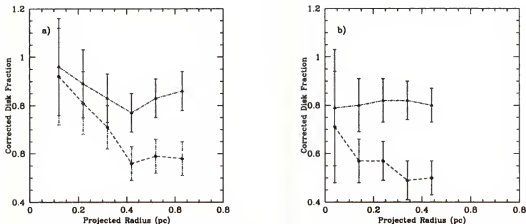


Figure 4-8: Disk fraction vs. projected cluster radius. The circumstellar disk fraction vs. projected cluster radius in the a) NGC 2024 and b) Trapezium clusters as determined from our $m_K=m_L=12.0$ completeness limit data. The dot-dashed line indicates the disk fraction as determined from *JHKL* colors while the dashed line represents the disk fraction determined from *JHK* colors. The disk fractions were corrected for foreground/background star contamination. The error bars represent \sqrt{N} errors in the disk fractions. The *JHKL* circumstellar disk fractions as a function of projected radius are the same to within the errors in both clusters. A decrease in the *JHK* disk fractions is observed in the Trapezium, however it is not significant to within the errors. In NGC 2024, however, the decrease observed in the *JHK* disk fraction is significant. There is a steady decline in the disk fraction to a radius of ~ 0.4 pc, at which point the circumstellar disk fraction remains constant.

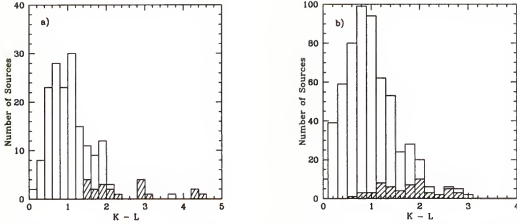


Figure 4-9: Distribution of $K-L$ colors. The $(K-L)$ frequency distributions in the NGC 2024 Trapezium clusters. a) The shaded region in the NGC 2024 distribution represents those sources from our NSFCAM survey for which K -band magnitudes were obtained from Levine et al. 2000 (ie. $14.0 < m_K < 16.5$). The total number of sources in the distribution is 185. b) The shaded region in the Trapezium cluster represents those sources lacking J and H -band photometry. The total number of sources in the distribution is 603.

Trapezium distribution represents those 57 objects that were not detected at either J -band or H -band. These objects represent the reddest sources in both surveys. A broad peak, centered around $K-L \approx 0.8$ to 1.0 appears in both distributions, with only a small fraction of the sources having $K-L \geq 2.0$. Neither distribution displays the feature near $K-L=0.0$ found by Kenyon & Hartmann (1995) for YSOs in Taurus and characteristic of non-excess or diskless stars. The shift of this peak to relatively large $K-L$ color is due to the effects of both reddening and infrared excess emission. To produce a $K-L$ color of 1.0 in a diskless star requires a visual extinction of $A_V \approx 25$. An examination of the $JHKL$ color-color diagrams for both clusters shows that most of the stars have extinctions of $A_V \leq 20$. Therefore, the primary cause of the shift of the $K-L$ color to larger values is the presence of infrared excess emission.

4.3 A Circumstellar Disk Census

The infrared excess fractions determined from the $JHKL$ color-color diagrams for the overall areas surveyed in the NGC 2024 and Trapezium clusters ($\geq 86\% \pm 8\%$

and $80\% \pm 7\%$ respectively) are much larger than the $58\% \pm 7\%$ and $50\% \pm 7\%$ derived from the *JHK* diagrams. Predictions from both observations and modelling suggest that this is what one would expect from excess emission from circumstellar disks (Lada & Adams 1992; Meyer et al. 1997). Taken together, this suggests that most, if not all, stars in the NGC 2024 and Trapezium clusters form with circumstellar disks.

Kenyon & Hartmann (1995) compiled observations of a sample of ~ 170 YSOs in the Taurus-Auriga dark cloud, that include the spectral energy distribution (SED) classification for each source as either Class I (YSOs surrounded by massive circumstellar envelopes of infalling material), Class II (YSOs surrounded by optically thick circumstellar disks) or Class III (diskless sources with no infrared excess emission)(ALS87). In Figure 4-10, we present the *JHK* and *JHKL* color-color diagrams for those 136 sources with $m_K \leq 9.5$, the completeness limit of our NGC 2024 sample corrected for the distance to Taurus ($d=140$ pc). Only 59/86 ($69\% \pm 9\%$) of the Class II sources lie in the infrared excess region of the *JHK* color-color diagram, whereas *all* of the Class II sources have colors indicative of excess emission in the *JHKL* diagram. Therefore, the *JHKL* colors are more robust for identifying circumstellar disks than *JHK* colors.

The measured overall *JHK* and *JHKL* excess fractions in Taurus are $49\% \pm 6\%$ and $69\% \pm 7\%$. Thus, in Taurus, the *JHKL* excess fraction for all sources with $m_K \leq 9.5$ is higher than the *JHK* fraction, similar to our observations of NGC 2024 and the Trapezium. This closely resembles the expected behavior of infrared excess emission produced by a population of sources characterized by a high disk fraction. Therefore, these measurements strengthen the suggestion that the infrared excesses we observe in NGC 2024 and the Trapezium originate in circumstellar disks. Moreover, the disk fraction derived from our *JHKL* observations is a relatively accurate representation of the disk fraction in both clusters.

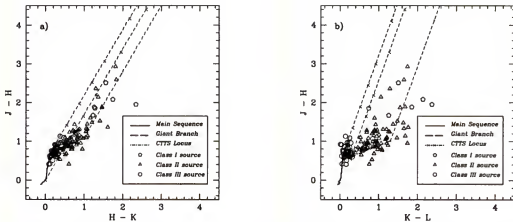


Figure 4-10: The JHK and $JHKL$ color-color diagrams for Taurus. The diagrams are shown as a) JHK and b) $JHKL$. The locations of the Class I, II and III sources in Taurus are labelled as follows: The Class I sources are denoted by a pentagon, Class II sources are shown with a triangle and Class III sources are shown with a circle. The data are taken from Kenyon & Hartmann (1995).

Further support for the disk interpretation in the Trapezium cluster derives from the $JHKL$ colors we observe for the well known proplyd sources. Proplyds are small, resolved sources seen in silhouette against the background nebulosity in optical Hubble Space Telescope (HST) images (O'Dell et al. 1993; O'Dell & Wong 1996). Theoretical considerations indicate that the proplyds are likely photoevaporating envelopes of circumstellar disks (Johnstone et al. 1998; Bally et al. 1998). We found 112/139 infrared sources associated with proplyds in our Trapezium survey. In Figure 4-11, we plot the color-color diagram for the 96 sources that were detected at $JHKL$. We find 97% of the proplyds have infrared excesses in the $JHKL$ color-color diagram, compared to only 70% in the JHK diagram. This confirms our earlier assertions that $K-L$ colors very effectively identify circumstellar disks.

Also plotted in Figure 4-11 are the locations of 33 radio sources that were within the boundaries of our survey (Churchwell et al. 1987; Felli et al. 1993). The emission from these sources is thought to arise in the ionized envelopes of photoevaporated disks. A large fraction ($\sim 64\%$) of these sources are associated with proplyds, independently confirming the identification of the radio sources as photoevaporating

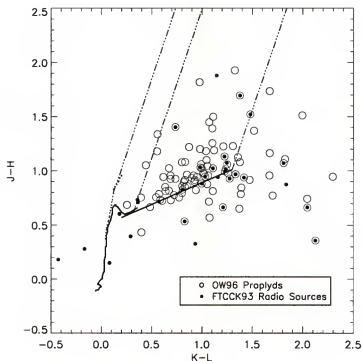


Figure 4-11: The $JHKL$ color-color diagram for the Trapezium proplyds. Also shown are the locations of the 33 radio sources that were detected in all four bands. In the diagram, the locus of points corresponding to both the unreddened main sequence and the CTTS locus, is plotted as a solid line, while the locus of positions of giant stars is shown as a dotted line. The two leftmost triple-dot-dashed lines define the reddening band for main sequence stars and are parallel to the reddening vector. Crosses are placed along these lines at intervals corresponding to 5 magnitudes of visual extinction. The rightmost triple-dot-dashed line is parallel to the reddening band. Figure adapted from Lada et al. (2000).

disks. Not surprisingly, we find that 87% have *JHKL* infrared excess emission. This fraction is somewhat lower than that for the proplyd population and may indicate that some of the radio sources are associated with diskless stars. Indeed, none of the radio sources without infrared excess emission is associated with a proplyd. The thermal radio sources not associated with proplyds are thought to be neutral condensations whose outer envelopes are ionized by ultraviolet radiation from $\theta^1\text{C Ori}$ (so-called partially ionized globules or PIGs). Pre-main sequence flaring activity may be the source of the non-thermal radio emission from the non-proplyd objects (Felli et al. 1993).

The large *JHKL* excess fractions ($\geq 80\%$) in the NGC 2024 and Trapezium clusters suggests that most of the sources that formed in the clusters were initially surrounded by disks, and remain surrounded by disks to the present time. Such large disk fractions argues for very young ages for both clusters, consistent with the young cluster ages (mean age $\simeq 0.3$ Myr and $\simeq 0.8$ Myr for NGC 2024 and Trapezium respectively) obtained by Meyer (1996) and Hillenbrand et al. (1998). Furthermore, a very large *JHKL* excess fraction ($\geq 84\%$) is observed in NGC 2024 even if we consider our deeper surveys (c.f., Table 4-2). Recall that in both NGC 2024 and the Trapezium, we are detecting sources to spectral types of at least M3, consistent with the observations of Meyer (1996) and Hillenbrand et al. (1998) for the sources common to all surveys. The fact that the infrared excess fraction remains very high to within the errors at the faintest *L* band magnitudes in NGC 2024, and over the range of spectral types from O to at least M3 in both clusters, suggests that disks form around most of the stars in very young clusters such as NGC 2024 and the Trapezium *independent* of mass.

The excess fractions measured for both NGC 2024 and the Trapezium are formally higher than that in Taurus. Nevertheless, the excess fractions in all three

regions are quite high. The NGC 2024 and Trapezium clusters represent an environment with at least an order of magnitude higher stellar density relative to Taurus, where star formation occurs in relative isolation (Lada 1999). This suggests that a high stellar density does not appear to inhibit the formation of circumstellar disks.

4.4 Disk Fraction vs. Projected Cluster Radius

In Figure 4-8, we see that the *JHKL* infrared excess fraction in the NGC 2024 and Trapezium clusters is relatively constant, within the errors, as a function of projected cluster radius. The decrease in the *JHK* excess fraction in the Trapezium is not significant to within our computed statistical errors, however Hillenbrand et al. (1998) observed a decrease in the disk fraction with radius in the Trapezium based on $I_C - K$ colors. We *do* observe a significant decrease in the *JHK* excess fraction in NGC 2024. Because the $K - L$ color is apparently able to identify *all* sources with candidate circumstellar disks in a *JHKL* color-color diagram, we can determine when the disk fraction begins to decrease. The fact that the *JHKL* excess fraction remains constant with projected radius implies that the disk fraction does not decrease in either cluster to the boundary of our survey. The observed trend in the *K*-band excess fractions appears to depend on projected cluster radius, perhaps suggesting that *JHK* observations underestimate the true disk fraction to increasingly large degrees with cluster radius.

Lada & Adams (1992) and Meyer et al. (1997) show that disk orientation and accretion rate affects the observed *JHK* colors, and hence whether or not a source is identified as having an infrared excess. The disk orientation and accretion rates could be different in the cluster center where the stellar density is higher than in the outer regions. In particular, close encounters between stars in the central regions of the NGC 2024 and Trapezium clusters may lead to tidal effects that increase the disk accretion rates and thus the disk detectability (Ostriker 1994). Both clusters have

high central densities, and the effects of induced accretion may be a contributing factor to the high apparent K band disk fractions observed in the central regions of the clusters. Indeed, Hillenbrand et al. (1998) attributed the decrease in the disk fraction with radius in the Trapezium cluster to the effects of the high stellar density near the cluster center (the mean distance between stars is only ~ 1000 AU).

However, the NGC 2024 and Trapezium clusters contain large amounts of nebulosity, especially near the cluster center, and this may be responsible for the observed trend in the K -band excess fractions with cluster radius, rather than an increase in K -band efficiency in detecting disks in the central cluster regions. To test this, we added 300 artificial stars with $JHKL$ magnitudes from 9.0 to 14.0 and having main sequence colors to regions of the NGC 2024 cluster with and without nebulosity. Aperture photometry was performed on these sources and their colors were calculated. Approximately 23% of the sources, independent of magnitude, that were placed in regions with nebulosity exhibited colors indicative of infrared excesses in the JHK color-color diagram, while all sources placed in non-nebulous regions showed no excesses. Sources in non-nebulous regions also show no excesses in the $JHKL$ diagram. In nebulous regions, however, only sources with $m_L > 11.0$ exhibited $JHKL$ excess emission. Only 4 stars with $m_L > 11.0$ lie in regions with nebulosity, and this would change our derived excess fraction by only $\sim 3\%$, well within our errors. Therefore, the large JHK excess fraction observed in the cluster center relative to the outer regions may be due to contamination caused by the extended nebulosity. The $K - L$ color is less susceptible to this effect and hence better represents the observed trend in disk fraction with cluster radius.

It is also possible that the large amount of nebulosity in the Trapezium cluster may be producing artificial infrared excesses similar to that observed in NGC 2024, and hence a larger *apparent* disk fraction near the center of the Trapezium. Indeed, the JHK infrared excess fraction observed in our study of the Trapezium does decrease

with projected cluster radius, however the error bars are large. Nevertheless, the *JHKL* excess fractions remain constant with cluster radius and, as is the case with NGC 2024, better represent the trend in disk fraction with radius in the Trapezium. Therefore, we suggest that caution must be applied using only observations shorter than *K*-band to infer disk fractions in nebulous environments.

4.5 Nature of Very Red Sources: Candidate Protostars

In Taurus, Kenyon & Hartmann (1995) determined that all of the YSOs having $K - L \geq 1.5$ were Class I (protostellar) sources. To investigate the possible protostellar population in the NGC 2024 and Trapezium clusters, we consider those sources with similarly large $K - L$ colors. Thirteen sources in our STELIRCAM survey of NGC 2024 have $K - L$ colors ≥ 1.5 and lie in the region of the *JHKL* color-color diagram beyond the reddening line projected from the red edge of the CTTS locus (Meyer et al. 1997). An additional 14 very red sources also have $K - L \geq 1.5$ and are located for the most part high within the CTTS reddening band. Furthermore, 18 sources from our NGC 2024 NSFCAM survey have similar $K - L$ colors, however $J - H$ colors are not determined for these sources and hence they cannot be plotted on a color-color diagram. We consider these sources to be candidate protostars. It may be that some of these sources are simply objects that are more embedded than those stars with similar $K - L$ colors in Taurus, and not true protostars. However, it would take visual extinctions of approximately $A_V=40$ and $A_V=15$ to produce a $K - L$ color of 1.5 magnitudes for Class III and Class II stars respectively. Most of the sources in NGC 2024 have extinctions less than this. Finally, one source was detected only in the *L* band and limits on its $K - L$ color significantly exceed 1.5 magnitudes. Therefore, a total of 46 sources are identified as candidate protostellar objects in the NGC 2024 cluster.

In the Trapezium, we find 94 sources with $K - L \geq 1.5$. Of these, 59 are also detected in the J and H -bands. Twenty-one of these have anomalous colors (as discussed previously) and are not likely protostellar candidates. The remaining 38/59 very red sources detected at $JHKL$ are located either to the right of the CTTS reddening band above the termination of the unreddened CTTS locus, or high within the CTTS reddening band. These sources exhibit extreme excess emission often characteristic of Class I sources (Lada 1999a), and can be considered as candidate protostars. There are 35 sources with $K - L \geq 1.5$ that were not detected at either J or H -bands, and cannot be placed on the color-color diagram. These sources are considered to be candidate protostellar objects for the same reasons listed above for NGC 2024. Finally, there are five stars that were only detected in the L -band, and limits on their $K - L$ colors significantly exceed 1.5 magnitudes. Altogether, we identify 78 candidate protostars in the Trapezium cluster.

If the star-formation rate in NGC 2024 and the Trapezium is constant, and the age of a typical T Tauri star (TTS) is known, then an estimate of the Class I (protostellar) phase of pre-main sequence evolution can be obtained. The Class I lifetime is given by:

$$\tau_{Class I} = \frac{N_{Class I}}{N_{PMS}} \times \tau_{Cluster} \text{ yr.} \quad (4.1)$$

There are 46/328 and 78/603 candidate Class I sources identified in the NGC 2024 and Trapezium clusters respectively. If the ages of the NGC 2024 and Trapezium clusters are ~ 0.3 to 1 Myr (Meyer 1996) and ~ 0.8 to 1 Myr (Hillenbrand et al. 1998), then the Class I lifetimes are $\tau_{Class I} \sim 0.4$ to 1.4×10^5 yr in NGC 2024 and 1.0 to 1.3×10^5 yr in the Trapezium cluster. Our estimates of the Class I lifetimes are similar to the approximate Class I lifetime of 1 to 2×10^5 yr in Taurus-Auriga (e.g., Myers et al. 1987; Kenyon et al. 1990, 1994b; Kenyon & Hartmann 1995).

We must note, however, that a number of proplyd sources in the Trapezium cluster have $K - L$ colors ≥ 1.5 , and are likely not protostellar objects. Thus, our identifications of protostars in NGC 2024 and the Trapezium are not unambiguous. Longer wavelength, mid-infrared observations are required to obtain more accurate estimates of the protostellar populations in both clusters. Such observations were acquired for the NGC 2024 cluster, and the results are presented in the next chapter.

CHAPTER 5 MID-INFRARED OBSERVATIONS OF THE NGC 2024 CLUSTER

5.1 Motivation for Mid-Infrared Study

In the previous chapter, we presented *JHKL* photometry for a statistically significant fraction of sources in the NGC 2024 and Trapezium clusters. Very large *JHKL* infrared excess fractions ($\geq 80\%$) were obtained to our faintest completeness limits in both clusters. Assuming that these infrared excesses are produced by circumstellar disks implies that disks may have formed around most of the sources in NGC 2024 and the Trapezium cluster independent of stellar mass.

While it appears that the *JHKL* data are very efficient in identifying circumstellar disks, observations at *L*-band are still not at a long enough wavelength to unambiguously determine the evolutionary state of the YSOs as protostellar objects, star/disk systems or sources with no circumstellar material (the Class I, II and III YSOs of ALS87). However, because contamination from photospheric emission is minimized at mid-infrared wavelengths, the presence of a circumstellar disk can be ascertained from observations at $10\ \mu\text{m}$ with little ambiguity if near-infrared data is also available. Therefore, combining near-infrared and mid-infrared observations represents an extremely powerful method for unambiguously identifying stars surrounded by circumstellar disks.

We therefore conducted the first sensitive mid-infrared imaging survey of the NGC 2024 cluster. We conducted the mid-infrared imaging survey of NGC 2024 reported here to construct SEDs over a broad wavelength range to determine whether or not the excess sources identified in our previous *JHKL* study of the NGC 2024 cluster have the power law form predicted for circumstellar disks (Lynden-Bell &

Pringle 1974; ALS87). Thus we investigate the efficiency of detecting circumstellar disk sources from near-infrared *JHKL* color-color diagrams.

5.2 Observations and Data Reduction

We observed all sources in the NGC 2024 cluster with $m_K \leq 10.5$ at mid-infrared wavelengths. A total of 59 YSOs were included in our magnitude limited survey. Observations at *N*-band ($10.8 \mu\text{m}$) were conducted during the periods 1996 December 13 to 15 and 1997 September 3 to 11 with the 3 meter telescope at the NASA Infrared Telescope Facility (IRTF) on Mauna Kea using the University of Florida 8 to $25 \mu\text{m}$ (mid-infrared) imager and spectrometer OSCIR. The array consists of a Boeing 128×128 pixel Si:As Blocked Impurity Band detector. The plate scale of OSCIR at the IRTF in the imaging mode is $0.223 \text{ arcsec/pixel}$, giving a field of view of $28'' \times 28''$. Standard chopping and nodding techniques were used with a chop rate of 8 Hz and a $30''$ N-S chopper throw. For all observations, the on-source integration time was 0.75 min.⁴

Individual frames for each YSO were registered and combined using Interactive Data Language (IDL) routines. Many of the resulting images contained extended spatial structure due either to extended thermal emission in the source field and/or incomplete subtraction of telescope and sky background emission. This structure was modelled by masking the sources in each field and fitting a seventh order polynomial in both right ascension and declination to the unmasked portion of the image. The polynomial model was then subtracted from the image. At the time of both observing runs, thermal control of the detector array in OSCIR was achieved via closed loop heater control using a temperature sensor mounted in the cold finger assembly that attaches the detector array to the optics bench. Due to the large thermal path

⁴Further information about OSCIR is available at www.astro.ufl.edu/iag/.

between the cold-finger assembly and the detector array, large variations in temperature (up to 1 K in some cases) at the array were observed using the on-array temperature sensor. This produced variations of as large as $\sim 10\%$ in the flat fields, although no gradients in the flat fields were obvious. (Subsequently, the closed loop temperature control was modified to use the on-array temperature sensor rather than the cold-finger temperature sensor, resulting in ~ 10 mK temperature stability and stable flat-fields). The calibration and cluster sources were always centered in the same region of the chip, therefore errors introduced in the photometry by not flat fielding the data are estimated to be no more than a few percent. It was therefore determined that flat fielding would not improve the data and thus flat fields were not used in the reduction.

Flux calibration was performed using α Tau as our primary standard star and NGC 2024 IRS 2 as an internal 'standard'. The in-band flux for α Tau was determined by integrating the spectral irradiance model from Cohen et al. (1995) through the N -band filter passband using the OSCIR filter transmission curve and an ATRAN atmospheric model for Mauna Kea. The computed in-band flux was combined with observations of α Tau at various airmasses to derive our flux calibration and airmass corrections. This flux was then applied to our internal 'standard' star. We observed α Tau at least twice on a given night. Assuming the flux of the internal 'standard' remains the same at all airmasses, we calculate the calibration factors for the range of airmasses through which the cluster was observed. The fluxes were then determined for all sources detected in the cluster. The errors in the absolute flux were typically $< 10\%$. Given that our observations were background limited, the 3σ and 5σ detection limits are 26.8 mJy and 44.7 mJy respectively.

5.3 Spatial Distribution of Mid-Infrared Sources

We detected 35/59 (59%) of the sources in our mid-infrared survey of the NGC 2024 cluster. Fluxes at J , H , K , L -bands, and $10\ \mu\text{m}$ are listed in Table 5-1. It is possible that some of the 24 nondetections are the result of limitations in the sensitivity of our survey, a point that we will examine later. The spatial distribution of all sources having $m_K = m_L \leq 12.0$ from our $JHKL$ survey is shown in Figure 5-1. Three of the 59 sources were outside our L band survey region and are therefore not included in Figure 5-1. Superimposed on this plot is the distribution of sources from our mid-infrared survey that were detected at both L band and $10\ \mu\text{m}$ (star symbol) and those that were not detected at $10\ \mu\text{m}$ (denoted by a pentagon). Figure 5-2 shows the radial surface density profile for all mid-infrared sources from our survey, both detections and nondetections, of the NGC 2024 cluster. The profile was created by counting the number of detected and nondetected sources in successive $20''$ annuli around the cluster center, taken to be the position of IRS 2, and normalizing by the annulus area. Within the errors, the spatial distribution of the sources with mid-infrared detections is similar to the distribution of sources not detected at $10\ \mu\text{m}$.

5.4 Spectral Energy Distributions and Spectral Indices

We constructed SEDs for the 35 YSOs with $10\ \mu\text{m}$ detections, and each source was classified using the least squares fit to the slope between 2.2 and $10\ \mu\text{m}$. In Figure 5-3, we present the SEDs of all sources in Table 5-1.

We calculated the spectral indices from 2.2 to $10\ \mu\text{m}$ for all observed sources from the relation:

$$\alpha = \frac{d\log(\lambda F_\lambda)}{d\log\lambda} \quad (5.1)$$

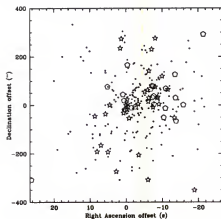


Figure 5-1: Distribution of mid-infrared sources in the NGC 2024 cluster. Positions of sources detected at both 3.4 and $10\ \mu\text{m}$ are shown by a star while sources not detected at $10\ \mu\text{m}$ are shown by a pentagon. The offsets are referred to the position $\alpha=5^{\text{h}}41^{\text{m}}45^{\text{s}}.28$, $\delta=-1^{\circ}54'31''.47$ (2000).

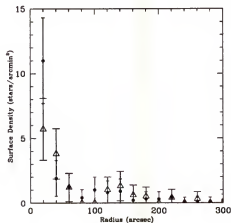


Figure 5-2: Radial surface density profile of mid-infrared sources. Sources detected at $10\ \mu\text{m}$ are plotted with a filled dot and nondetected sources are plotted with a triangle. The error bars represent \sqrt{N} errors in each bin.

Table 5-1: The *JHKL* and $10\mu\text{m}$ Fluxes for Sources Surveyed in NGC 2024

ID	RA (2000)	Dec (2000)	α^1	J (mJy)	H (mJy)	K (mJy)	L (mJy)	N (mJy)
1	5 41 45.79	-01 54 31.43	0.2	60.1	910.4	3078.9	41917.8	19152.9
2	5 41 37.79	-01 54 39.05	-0.4	1073.3	1045.3	1557.4	1668.8	3783.0
4	5 41 39.04	-01 52 09.74	-0.4	43.1	222.4	655.2	1508.0	2079.6
6	5 41 49.79	-01 54 30.92	0.2	124.4	330.5	576.0	522.9	3369.6
12	5 41 37.28	-01 49 55.71	-0.3	29.6	101.7	256.1	451.2	805.4
14	5 41 37.22	-01 53 15.51	-1.2	131.4	192.0	246.8	202.5	187.9
22	5 41 44.79	-01 54 26.56	-0.7	9.7	61.8	192.5	415.3	381.2
23	5 41 46.68	-01 49 58.79	-1.3	66.5	132.8	192.5	241.2	139.6
24	5 41 39.00	-01 54 00.54	-1.9	21.8	79.3	185.5	204.4	53.9
26	5 41 36.19	-01 54 26.83	-0.7	19.2	61.8	166.1	382.3	318.1
29	5 41 50.98	-01 55 07.61	1.0	23.3	67.8	154.3	382.3	3946.8
33	5 41 38.27	-01 50 40.88	-1.1	21.2	73.0	142.0	184.7	134.6
38	5 41 41.73	-01 57 56.54	-0.2	16.4	60.7	134.4	195.2	480.3
39	5 41 33.71	-01 53 26.25	-1.1	42.3	88.6	131.9	179.6	117.4
40	5 41 39.09	-01 59 38.85	-1.2	80.7	122.2	129.5	108.2	100.7
44	5 41 45.09	-01 54 48.28	-0.2	3.4	23.3	120.3	300.9	488.8
45	5 41 39.20	-01 54 16.15	-0.9	3.6	31.9	119.2	306.5	183.4
48	5 41 47.90	-01 59 04.79	0.0	11.3	42.8	109.7	309.3	610.4
49	5 41 39.41	-01 53 28.86	-1.2	5.2	39.7	104.8	159.4	88.1
53	5 41 36.80	-01 54 00.78	-1.2	22.0	60.7	101.0	81.4	71.0
54 ²	5 41 26.28	-02 00 20.62	-0.6	41.9	71.0	100.1	–	176.4
56	5 41 36.50	-01 53 56.85	-1.1	26.0	72.3	97.4	62.3	71.6
58	5 41 44.38	-01 55 24.73	-1.6	9.6	34.0	95.6	153.6	46.5
61	5 41 40.11	-01 53 36.02	-0.8	4.4	23.9	93.0	200.6	154.9
64	5 41 31.98	-01 55 22.03	-0.9	19.2	49.6	80.2	83.6	94.4
73	5 41 44.79	-01 54 37.06	-1.0	3.6	15.0	57.1	101.5	63.5
74	5 41 45.00	-01 54 07.57	-0.9	<3.2	4.7	57.1	193.4	88.3
75	5 41 52.24	-01 57 17.60	-0.9	12.0	31.9	56.5	70.9	68.2
78	5 41 53.23	-01 57 43.57	-0.4	7.0	21.8	54.0	110.3	167.7
80	5 41 41.89	-01 54 25.95	-0.6	3.2	15.7	53.5	126.6	121.8
88	5 41 53.88	-01 55 16.82	-0.8	4.2	17.2	46.6	122.0	75.7
90	5 41 46.87	-01 50 36.90	-0.9	14.3	31.6	45.8	55.3	59.3
92	5 41 45.98	-01 55 03.04	-0.6	<3.2	9.7	44.5	97.8	95.0
98	5 41 50.23	-01 57 45.15	-1.0	6.3	19.7	41.7	52.3	44.0
100	5 41 35.33	-01 52 31.87	-0.9	7.9	23.1	40.6	68.9	54.2

¹Slope is computed using the least squares fit between the *K*-band and $10\mu\text{m}$ points.²Source is not in our *L*-band survey region.

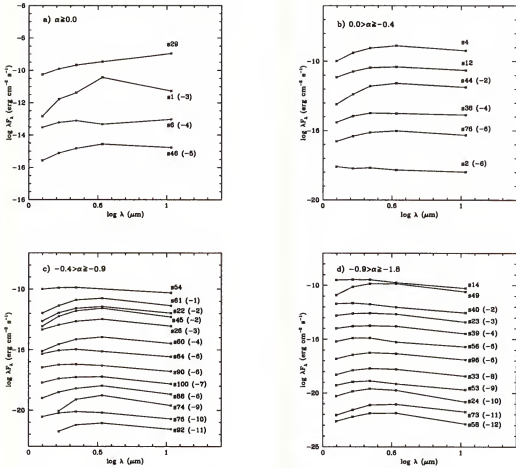


Figure 5-3: Spectral energy distributions of detected mid-infrared sources. The SEDs are shown for a) $\alpha > 0.0$, b) $0.0 > \alpha \geq -0.4$, c) $-0.4 > \alpha \geq -0.9$ and d) $-0.9 > \alpha \geq -1.6$. Fluxes are given in Table 5-1. The source ID numbers are as referenced in Table 5-1, and the numbers in parentheses next to each source name are the powers of 10 used to scale the SED.

to quantify the natures of their SEDs (Young et al. 1986). We adopted the classification scheme of Greene et al. (1994) in our analysis as it is believed to correspond well to the physical stages of evolution of YSOs (e.g. André & Montmerle 1994). Class I sources have $\alpha > 0.3$, $0.3 > \alpha \geq -0.3$ are “flat spectrum” sources, $-0.3 > \alpha \geq -1.6$ are Class II sources and $\alpha < -1.6$ are Class III YSOs. Table 5-1 lists the 2.2 to $10 \mu\text{m}$ spectral indices, α , for all sources and the distribution of spectral indices for the sample is shown in Figure 5-4.

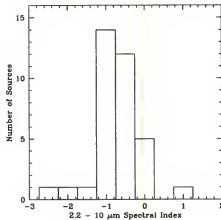


Figure 5-4: Distribution of the 2.2 to 10 μm spectral indices. The distribution is strongly peaked around $-1.0 < \alpha < 0.0$ indicating that most of the detected sources are Class II objects.

An analysis of the spectral indices for the YSOs detected in NGC 2024 reveals 1 Class I source, 6 “flat spectrum” sources, 27 Class II sources and 1 Class III source. As noted in Greene et al. (1994), we must consider the NGC 2024 environment when classifying YSOs based on near-infrared spectral indices as calculated above. The slopes of the SEDs can be steepened in regions of high extinction. Because of this, there may be more Class II and III YSOs and fewer Class I and flat spectrum YSOs in the NGC 2024 sample than calculated using our spectral index classification scheme. We calculated the extinction toward each object (except the Class I source) from its location in the *JHKL* color-color diagram (see Figure 5-7) assuming the extinction law of Rieke & Lebofsky (1985; hereafter RL85) as discussed in section 5.6. Only sources 12 and 58, which become Class II and III YSOs respectively, would be reclassified. This will have a very small effect on our derived mid-infrared disk fraction (see section 5.6) because only 1 source ($\sim 2\%$ of the sample) would no longer appear to have a disk.

5.5 Nondetections and Sensitivity Considerations

A total of 24/59 sources were not detected in our mid-infrared survey. Three of these were not within the boundary of our L -band survey. An additional source was not detected at L -band and cannot be placed in the $JHKL$ color-color diagram (see Section 5.6). We therefore only consider the 20 remaining sources. We must determine whether these sources were not detected due to sensitivity limitations or because they do not have a mid-infrared excess. A Class I source with $\alpha=0.3$, the boundary between Class I and flat spectrum sources, would have K -band magnitudes of $m_K \simeq 13.1$ and $m_K \simeq 12.6$ respectively at our 3σ and 5σ $10\ \mu\text{m}$ sensitivity limits. Therefore, because our survey included all sources brighter than a K -band magnitude of 10.5, we detected all Class I sources present in our sample. In Figure 5-5, we present a plot of the expected N -band flux as a function of K -band magnitude for a Class II source with a spectral index of $\alpha=-1.6$ (the boundary between Class II and Class III sources). At our 3σ and 5σ $10\ \mu\text{m}$ sensitivity limits, a Class II source with $\alpha=-1.6$ would have K -band magnitudes of $m_K \simeq 9.9$ and $m_K \simeq 9.3$ respectively. These limits are labelled in Figure 5-5. In Figure 5-6, we present the distribution of sources detected at $10\ \mu\text{m}$ as a function of K -band magnitude. The fraction of sources with mid-infrared detections begins to decrease at a K -band magnitude of ~ 9.0 . A comparison of Figures 5-5 and 5-6 shows that the decrease in the fraction of $10\ \mu\text{m}$ excess sources begins at approximately our 5σ mid-infrared detection limit. Therefore, for sources fainter than $m_K \simeq 9.3$ our nondetections may be due to sensitivity limitations rather than the YSOs not having a mid-infrared excess.

Five of the 20 sources that were not detected are brighter than $m_K=9.3$. All of these sources have colors that place them in the reddening band of the $JHKL$ color-color diagram (see Figure 5-7 in next section) for the NGC 2024 cluster and are therefore classified as Class III YSOs. An examination of the K -band luminosity function for our cluster and control fields reveals that these sources are likely *not*

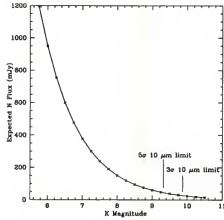


Figure 5-5: Expected N -band flux vs. K -band magnitude. The diagram is plotted for Class II sources having a spectral index of $\alpha=-1.6$. The 3σ and 5σ sensitivity limits of our observations are indicated.

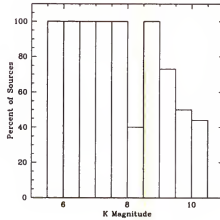


Figure 5-6: Percentage of $10\ \mu\text{m}$ sources detected vs. K -band magnitude. Bin size is 0.5 mag. All sources brighter than $m_K=8$ were detected at N band. The fraction of sources detected decreases for $m_K>9$ due to sensitivity limitations.

foreground/background stars. Fifteen sources with $m_K > 9.3$ were not detected in our survey. These objects are likely either Class II or Class III, however given our sensitivity limitations, it is not possible to discriminate between the two classifications based on our mid-infrared data alone. Because we are able to unambiguously detect Class I YSOs to a K -band magnitude of $m_K \sim 13.0$, the nondetections are not Class I sources. We can speculate on the nature of the 15 $m_K > 9.3$ nondetections by examining their near-infrared colors. Eight of the fifteen sources have JHK_L colors that place them in the infrared excess region of the color-color diagram (see Figure 5-7 in the next section). Because a near-infrared excess is evidence of a YSO possibly surrounded by a circumstellar disk, these sources are candidate Class II objects. The other seven sources all lie in the reddening band and are therefore candidate Class III sources, although a Class II designation cannot be unambiguously ruled out, especially for sources that lie near the right side of the reddening band.

5.6 Color-Color Diagrams

In Figure 5-7, we present the JHK_L color-color diagram for the sources, both detections and nondetections, in our mid-infrared survey of the NGC 2024 cluster that were within the boundaries of our near-infrared JHK_L survey. All sources are plotted showing their SED classifications. Class I sources are designated with a pentagon, flat spectrum sources with a square, Class II sources with a star and Class III sources with a triangle. The five sources determined to be Class III from our nondetections are also plotted in Figure 5-7. The remaining sources that were not detected in our survey are shown with a point. As noted in the previous section, these sources are likely either Class II or Class III, however an unambiguous determination cannot be made. In the diagram, we plot the locus of points corresponding to the unreddened main sequence as a solid line and the locus of positions of giant stars as a heavy dashed line (Bessell & Brett 1988). The Classical T Tauri star (CTTS)

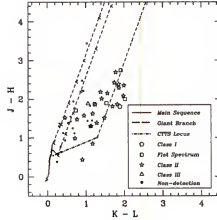


Figure 5-7: Color-color diagram for mid-infrared sources. The JHK_L color-color diagram shows all sources, both detected and not detected, in our $10\ \mu\text{m}$ survey of NGC 2024. The sources detected at $10\ \mu\text{m}$ are plotted showing their SED classifications. Class I sources are designated with a pentagon, flat spectrum sources with a square, Class II sources with a star and Class III sources with a triangle. Sources that were not detected in our survey are shown with a point. In addition, we plot the locus of points corresponding to the unreddened main sequence as a solid line, the locus of positions of giant stars as a dashed line and the CTTS locus as a dot-dashed line. The two leftmost parallel dashed lines define the reddening band for main sequence stars and are parallel to the reddening vector. Crosses are placed along these lines at intervals corresponding to 5 magnitudes of visual extinction. The rightmost dashed line is parallel to the reddening band.

locus (Meyer et al. 1997) is shown as a dot-dashed line. The two leftmost parallel dashed lines define the reddening band for main sequence stars and are parallel to the reddening vector. Crosses are placed along these lines at intervals corresponding to 5 magnitudes of visual extinction. The reddening law of RL85 was adopted. The adopted intrinsic colors of the latest spectral type stars observed in NGC 2024 (M5) and the location of the righthand reddening line was selected as in the last chapter.

All of the Class I and flat spectrum sources lie in the infrared excess region of the JHK_L color-color diagram. In addition, all but one (25/26; 96%) of the Class II sources lie in the infrared excess region of the color-color diagram. In Figure 5-8 we show the variation of $K - L$ with $K - N$. Sources are labelled with their SED

classifications as in Figure 5-7. The horizontal dashed line corresponds to the photometric colors of an M5 main sequence star ($K - L = 0.29$; Bessell & Brett 1988). Class I sources lie to the right of the vertical dashed line, which represents sources with $\alpha = 0.3$, while the flat spectrum and Class II sources lie to the left of this line and have $K - L \geq 0.29$. Class III YSOs have $K - L \leq 0.29$ and $K - N \leq 1.0$. The length of the arrow above the horizontal dashed line corresponds to the displacement produced by 10 magnitudes of visual extinction. Before being plotted in Figure 5-8, all sources except the Class I source were dereddened using the extinction law of RL85. For sources in the infrared excess region of the diagram, we dereddened each source to the CTTS locus. For sources to the right of the termination point of the CTTS locus, we used adopted intrinsic colors for the Class II and flat spectrum sources. Accurate dereddened colors cannot be derived for the Class I source via this method. For Class III sources in the reddening band of Figure 5-7, median intrinsic colors of $(J - H)_o = 0.62$ and $(H - K)_o = 0.1$ were adopted (Strom et al. 1993; hereafter SSM). For Class II sources, we adopted intrinsic colors of $(J - H)_o = 0.8$ and $(H - K)_o = 0.5$, while for flat spectrum sources $(H - K)_o = 0.75$ was used (SSM; Greene & Meyer 1995). Arrows are placed on the 5 nondetected sources that were determined to be Class III YSOs to indicate upper limits on the $K - N$ colors.

There is a clear progression from the very red Class I YSO \rightarrow flat spectrum \rightarrow Class II \rightarrow Class III. A similar trend has been observed in ρ Oph and Taurus (Wilking et al. 1989; Kenyon & Hartmann 1995). An examination of Figures 5-7 and 5-8 shows that source 24, the Class III source that was detected at $10 \mu\text{m}$, has both near- and mid-infrared colors indicative of a Class II YSO and may indeed be a circumstellar disk source. If this is the case, 28/40 ($70\% \pm 13\%$) of the sources for which SED classes could be determined are Class II YSOs. In addition, a significant fraction of the mid-infrared flux in the flat spectrum sources (which represent a transition between Class I and Class II YSOs) can be attributed to the presence of a circumstellar disk.

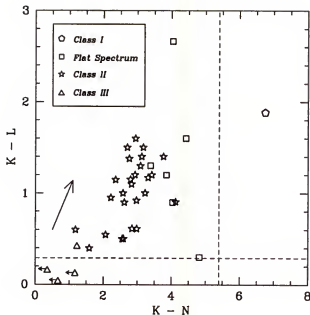


Figure 5-8: Color-color diagram of $K-L$ vs. $K-N$. The diagram shows the variation of $K-L$ with $K-N$ for the sources with K -band magnitudes brighter than our 10 μm sensitivity limit. Class I sources are designated with a pentagon, flat spectrum sources with a square, Class II sources with a star and Class III sources with a triangle. All sources except the Class I source were dereddened. The horizontal dashed line corresponds to a star with M5 main sequence colors. The vertical line represents the $K-N$ color for a source with $\alpha=0.3$. The length of the arrow above the horizontal dashed line corresponds to the displacement produced by 10 magnitudes of visual extinction. Arrows on the 5 nondetected sources that were determined to be Class III YSOs indicate upper limits on the $K-N$ colors. There appears to be a smooth trend from the Class I source to the bluest Class II sources. The Class III source that has near-infrared colors indicative of circumstellar disks lies within the region occupied by the Class II sources and should likely be reclassified (see text).

Therefore, including the flat spectrum sources among the circumstellar disk YSOs yields a disk fraction of 34/40 (85% \pm 15%) for the NGC 2024 cluster.

5.7 Luminosity and Extinction Estimates for Class II Sources

In Table 5-2, we present bolometric luminosity and visual extinction estimates for all Class II sources in our sample. We note here that we cannot determine an accurate luminosity for the Class I and flat spectrum sources in our sample due to the paucity of our long wavelength ($\lambda \leq 20 \mu\text{m}$) data. We can, however, calculate bolometric luminosities for the Class II sources using the correlation between the bolometric luminosities of the Class II sources and their dereddened *J*- and *K*-band fluxes as derived in Greene et al. (1994). The bolometric luminosity of each source is computed by correcting the observed fluxes for interstellar extinction (A_V), which is particularly important in the NGC 2024 cluster. The A_V values (Table 5-2) were calculated using the extinction law of RL85 and each source was dereddened to the CTTS locus. As in Greene et al. (1994), the Class II bolometric luminosities in Table 5-2 were calculated by taking the mean of the luminosities computed from the absolute *J*- and *K*-band fluxes. The errors in the bolometric luminosities, δL , are equal to 1/2 the absolute value of the difference between the *J*- and *K*-band luminosity estimates. No *J*-band magnitude could be determined for source 74, hence the luminosity estimate for this source is based only on the dereddened *K*-band fluxes.

Using the empirical relationship between bolometric luminosity and *K*-band absolute flux from Greene et al. (1994), we find that, at the distance of NGC 2024, a 1 L_\odot Class II source would have a *K*-band magnitude of $m_K \simeq 9.9$, equivalent to our 3σ 10 μm sensitivity limit. Therefore, our observations are sensitive to the detection of a 1 L_\odot Class II source near the front of the HII region. However, a similar Class II source embedded halfway into the HII region has $m_K \simeq 11.0$ (average $A_V \simeq 10.9$), and therefore is not detected in our mid-infrared survey. We estimate that throughout

Table 5-2: Luminosities and A_V for Class II Sources

Source ID	A_V (mag)	L (L_\odot)	δL (L_\odot)
2	8.7	35.0	11.0
4	14.0	30.0	0.2
14	0.8	3.3	0.3
22	13.0	7.5	0.9
23	4.0	4.0	0.7
24	8.5	5.0	0.3
26	7.5	3.5	0.8
33	9.4	4.7	0.8
39	5.4	3.2	0.6
40	1.6	2.5	0.6
45	12.0	3.7	0.8
49	12.0	4.3	0.2
53	5.6	2.3	0.3
54	4.6	2.8	0.6
56	5.6	2.8	0.9
58	8.8	2.3	0.6
61	11.0	2.2	0.7
64	7.1	2.5	0.5
73	11.0	1.8	0.5
74 ¹	42.8	60.8	—
75	7.1	1.6	0.1
78	6.5	1.1	0.3
80	12.0	1.7	0.5
88	9.8	1.3	0.3
90	4.9	1.1	0.1
92	14.0	1.7	0.5
98	6.1	1.0	0.7
100	5.5	1.0	0.1

¹Luminosity calculated using only K -band.

most of the region surveyed, we are sensitive to the detection of Class II YSOs with $L \geq 3 L_{\odot}$.

5.8 Comparison of Near-Infrared and Mid-Infrared Disk Fractions

We find a circumstellar disk fraction in the NGC 2024 cluster of $85\% \pm 15\%$. This is consistent with the disk fraction of $(86\% \pm 8\%)$ inferred from the *JHK*L color-color diagram. In addition, all but one of the disk sources identified in our sample lie in the infrared excess region of the *JHK*L color-color diagram. Indeed, an almost unambiguous discrimination between disk (Class I, flat spectrum, Class II) and diskless (Class III) YSOs can be made from the *JHK*L colors. These results confirm that most, if not all, of the stars in the NGC 2024 cluster formed with disks, and these disks still exist at the present time. Our results also imply that *JHK*L colors are a very efficient means to determine circumstellar disk fractions in cluster environments.

One of our Class II sources (source 56) lies within the reddening band of the *JHK*L color-color diagram. It is unlikely that the colors for this source are in error because this requires larger photometric errors than those measured. It is also unlikely that variability is responsible for the location of this source in the *JHK*L color-color diagram because this YSO is also located in the reddening band of the *JHK* color-color diagram, and the *JHK* data were taken simultaneously. That this object possesses a mid-infrared excess suggests the presence of an inner hole in the circumstellar dust distribution. Such an object is indicative of a transition source between Class II and Class III YSOs. The lack of a near-infrared excess in this source could also be due to inclination effects instead of, or in addition to, its disk having an inner hole (Meyer et al. 1997). Source 24, the Class III YSO ($\alpha = -1.9$) detected at $10 \mu\text{m}$, not only has near-infrared colors that signify the presence of an infrared excess, but also combined near- and mid-infrared colors typical of Class II objects (Figure 5-8). We consider this object to indeed be a Class II YSO, and

suggest that the criterion for discriminating between Class II and Class III YSOs from SEDs needs to be reconsidered. In the classification scheme of Lada (1987), the boundary between Class II and III YSOs is $\alpha=-2.0$. Given that our Class III source has $\alpha=-1.9$ suggests that the Lada (1987) criterion may be more appropriate in making a distinction between Class II and Class III sources.

5.9 Nature of the Very Red $K-L$ Sources

Among the Taurus population of YSOs, all sources that have $K-L \geq 1.5$ are almost always Class I objects (Kenyon & Hartmann 1995). In our mid-infrared survey of NGC 2024, we find 14 sources with $K-L \geq 1.5$. Eight of these sources lie in the region of the *JHKL* color-color diagram beyond the termination of the unreddened CTTS locus, and possess extreme infrared excess emission attributed to the presence of candidate protostellar objects (e.g., Meyer et al. 1997; Lada 1999a; Lada et al. 2000). An additional 6 sources, located for the most part high within the CTTS reddening band, also have $K-L \geq 1.5$ and are thus consistent with protostellar objects.

Of the 14 sources in our survey with $K-L \geq 1.5$, ten sources are unambiguously identified as Class II objects and another three as flat spectrum YSOs. Therefore, of the sources with $K-L$ colors indicative of candidate protostellar objects, *only one* is indeed a true Class I source, while 3 are found to be flat spectrum sources. This suggests that $\sim 29\%$ of the $K-L$ candidates are protostellar in nature, while $\sim 7\%$ are true Class I YSOs. This may be due to the effects of extinction. It would take $A_V \simeq 40$ to produce a $K-L$ color of 1.5 magnitudes for a Class III YSO, and at least $A_V = 15$ for a Class II source. Indeed 8 of the Class II sources in our sample have visual extinctions greater than $A_V = 15$ (c.f., Table 5-2), consistent with the number of Class II YSOs that were identified as candidate protostars based on $K-L$ colors alone. Therefore, while an almost unambiguous identification between sources with

and without disks can be made from *JHKL* colors, mid-infrared data are required to identify true protostellar objects. This suggests that any estimate of the numbers and lifetimes of protostellar sources based on near-infrared $K - L$ colors should be viewed with caution.

5.10 Comparison with ρ Oph and Taurus-Auriga

We find 1 Class I source, 6 flat spectrum, 28 Class II and 5 Class III sources among the YSOs surveyed in the NGC 2024 cluster. Greene et al. (1994) completed a mid-infrared survey of 56 YSOs with $m_K < 10$ in the ρ Oph cluster. This work supplements previous studies of ρ Oph by Wilking & Lada (1983) and Wilking, Lada, & Young (1989). Before we compare our results with the stellar population in ρ Oph, we must account for the difference in distance between the clusters. We place the three ρ Oph samples at the distance of NGC 2024 (~ 415 pc) and include only those sources brighter than $m_K = 10.5$, as was done with our mid-infrared sample. Twenty-two sources fit these criteria.

The ratio of the number of Class I + flat spectrum sources to the number of Class II + Class III YSOs in NGC 2024 ($21\% \pm 8\%$) is the same, within the errors, as that in ρ Oph ($29\% \pm 13\%$). This indicates that NGC 2024 and ρ Oph are similar in age, consistent with the comparison of T Tauri star (TTS) ages in both NGC 2024 and ρ Oph by Meyer (1996). Similarly, NGC 2024 and ρ Oph are likely both younger than Taurus-Auriga because the ratio of Class I to Class II YSOs in Taurus-Auriga is smaller by at least a factor of 2 than in either NGC 2024 or ρ Oph (Kenyon et al. 1990), thus indicating that Taurus-Auriga may have a mean age that is older than both NGC 2024 and ρ Oph. This is consistent with published mean ages of CTTS stars in NGC 2024 and Taurus (~ 0.3 Myr and ~ 0.7 Myr) derived from the H-R diagram.

There is a progression in the mean luminosities of the Class II sources in NGC 2024, ρ Oph and Taurus-Auriga. NGC 2024 has the highest mean luminosity of $7.0 \pm 2.5 L_{\odot}$, with smaller luminosities of $2.2 \pm 0.3 L_{\odot}$ and $1.3 \pm 0.2 L_{\odot}$ in ρ Oph and Taurus-Auriga respectively. We note that the mean luminosity for NGC 2024 was calculated including sources 2, 4 and 74, the three sources with luminosities much larger than the others. These three sources may be skewing the mean to anomalously high values. The median luminosity, that may be more representative of the true Class II luminosity in NGC 2024, is $2.5 \pm 0.3 L_{\odot}$. If we exclude sources 2, 4 and 74, the mean luminosity is $2.8 \pm 0.3 L_{\odot}$, similar to the median value. This is still higher than the Class II luminosity in Taurus-Auriga but similar to that in ρ Oph. The mean luminosities in all three star forming regions were computed following the method of Greene et al. (1994). The mean luminosities in ρ Oph and Taurus-Auriga were calculated using data from Greene et al. (1994) and Kenyon & Hartmann (1995) respectively.

The difference in Class II luminosities between NGC 2024 and Taurus-Auriga can be understood given the difference in mean ages between the two regions. As a result of their pre-main sequence evolution, the most luminous Class II YSOs are found in the youngest region of star formation, and the least luminous in the oldest region. Indeed, the difference in the observed luminosities ($\Delta \log(L/L_{\odot}) \simeq 0.3$) roughly corresponds to that expected ($\Delta \log(L/L_{\odot}) \sim 0.3$ to 0.4) given the difference in the mean ages of the two regions based on the pre-main sequence models of D'Antona & Mazzitelli (1998). A higher mean luminosity in NGC 2024 relative to ρ Oph can be understood if the mass distributions in the two regions are different. A comparison of the mass functions of Class II YSOs in NGC 2024 and ρ Oph by Meyer (1996) reveals that NGC 2024 is forming more massive stars. If the median luminosity in NGC 2024 is more representative, then the similarity in the Class II luminosities of

NGC 2024 and ρ Oph would not be surprising given that they have similar ages and accretion properties (Meyer 1996).

CHAPTER 6 CIRCUMSTELLAR DISKS IN THE IC 348 CLUSTER

In Chapter 4, we presented the results of our L -band surveys of the NGC 2024 and Trapezium clusters. These observations clearly established that the vast majority of the stars ($\geq 80\%$) in these clusters, independent of stellar mass and stellar environment, formed with circumstellar disks. In this chapter, we present the results of an L -band imaging survey of the somewhat older IC 348 cluster.

6.1 Spatial Distribution

We detected 107 sources at L -band with STELIRCAM to the completeness limit of our survey ($m_L=12.0$). All of these sources were detected in the J -, H - and K -bands in the SQUID survey of Lada & Lada (1995). In Figure 6-1, we present the spatial distribution of all sources in our STELIRCAM survey. Overall, the source distribution is fairly uniform with a slight central concentration.

6.2 The JHK_L Infrared Excess Fraction

In Figure 6-2, we present the JHK_L color-color diagram for the IC 348 cluster. In the diagram, we included only those 107 sources from our STELIRCAM survey which have $m_K=m_L\leq 12.0$. Thus, we only include those sources for which we are sensitive to stellar photospheres (i.e., $K-L=0.0$). This insures a meaningful determination of the fraction of the sources having an infrared excess, and thus the circumstellar disk fraction. In the diagram, we plot the locus of points corresponding to the unreddened main sequence as a solid line and the locus of positions of giant stars as a heavy dashed line (Bessell & Brett 1988). The two leftmost parallel

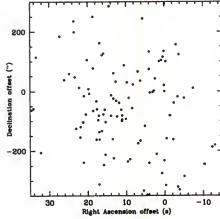


Figure 6-1: Distribution of L -band sources in IC 348. Sources are plotted to the completeness limit of our STELIRCAM survey ($m_L=12.0$). The offsets are referred to the position of BD+31°643 ($\alpha=3^h44^m34^s15$, $\delta=32^\circ09'44''.58$ (2000)).

dashed lines define the reddening band for main sequence stars and are parallel to the reddening vector. Crosses are placed along these lines at intervals corresponding to 5 magnitudes of visual extinction. The classical T Tauri star (CTTS) locus is plotted as a dot-dashed line (Meyer et al. 1997). The reddening law of Cohen et al. (1981), derived in the CIT system and having slopes in the JHK and $JHKL$ color-color diagrams of 1.692 and 2.750 respectively, was adopted.

A significant fraction of the cluster sources fall outside and to the right of the reddening lines in the infrared excess region of the $JHKL$ color-color diagram. Indeed, a total of 59/107 ($55\%\pm7\%$) of the sources lie in the infrared excess region. We must correct this fraction for field star contamination. The foreground/background contamination was determined by first counting the total number of stars observed in the control fields from the Lada & Lada (1995) JHK survey of IC 348 to $m_K=12$. Scaling this number to the cluster area observed and accounting for the average extinction in IC 348 ($A_K\approx0.5$ magnitudes; Lada & Lada 1995), we find a field star contamination of 16 stars. Applying this correction to the infrared excess fraction,

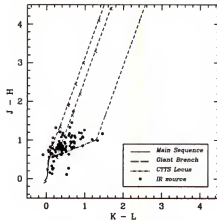


Figure 6-2: The $JHKL$ color-color diagram for IC 348. Only those sources with $m_L = m_K \leq 12.0$ and $JHKL$ photometric errors less than 10% are plotted. In the diagram, the locus of points corresponding to the unreddened main sequence is plotted as a solid line, the locus of positions of giant stars is shown as a heavy dashed line and the CTTS locus as a dot-dashed line. The two leftmost dashed lines define the reddening band for main sequence stars and are parallel to the reddening vector. Crosses are placed along these lines at intervals corresponding to 5 magnitudes of visual extinction. The rightmost dashed line is parallel to the reddening band.

we estimate that $65\% \pm 8\%$ of the sources in the IC 348 cluster have colors exhibiting $JHKL$ infrared excess emission.

As discussed in Chapter 4, the derived fraction of excess sources is sensitive to the location of the boundary of the reddening band. This depends on the adopted intrinsic colors of the latest spectral type stars. At our $m_K = m_L = 12.0$ completeness limit, we are sensitive to stars with spectral classes down to M5 (Luhman et al. 1998). Furthermore, this also corresponds to the boundary adopted in our previous L -band studies of the NGC 2024 and Trapezium clusters. The excess fraction for IC 348 is therefore calculated assuming the boundary of the reddening band in the $JHKL$ diagram passes through M5 colors from Bessell & Brett (1988).

The frequency of near-infrared excess sources determined from the color-color diagrams also depends on the adopted reddening law and to a lesser extent on the photometric system used to plot the positions of the main sequence stars and the

reddening bands. We calculated the *JHK*L infrared excess fraction for two other reddening laws obtained in different photometric systems (Koornneef 1983; Rieke & Lebofsky 1985), and find *JHK*L excess fractions of $65\% \pm 8\%$ and $60\% \pm 8\%$ respectively. These fractions are within the quoted (statistical) error of our determination using a Cohen et al. (1981) reddening law.

As was the case with NGC 2024 and the Trapezium, we note that photometry at *L*-band can be affected for heavily obscured sources if the source spectrum contains a $3.08 \mu\text{m}$ ice absorption feature. In the IC 348 cluster, most of the sources are extinguished by $A_V \leq 5$ magnitudes (Lada & Lada 1995). In IC 348, we find that most of the stars in the cluster have $\tau_{ice} \leq 0.32$. Aspin & Sandell (1997) calculated the narrow-band *L* magnitude correction due to ice absorption in the NGC 1333 cluster using the Sato et al. (1990) τ_{ice} - A_V relation discussed in Chapter 4. For a source with $\tau_{ice} = 0.32$, the narrow-band *L* correction is ~ 0.1 magnitude, less than that in NGC 2024 and the Trapezium. The correction to our IC 348 broad-band *L* photometry is even smaller due to the increased continuum flux from the stellar source, which would dilute the line strength of the ice feature relative to that observed in a narrow-band *L* filter. We therefore do not expect the ice feature to produce a large effect on our *L*-band photometry.

6.3 The H α Emission Stars and *JHK*L Colors

In Figure 6-3, we present the *JHK*L color-color diagram showing the location of those 60 sources in our survey which had unambiguous counterparts in the H α survey of Herbig (1998). Filled circles represent those sources with positive detections, that is sources which have equivalent widths $\text{EW}(\text{H}\alpha) \geq 2 \text{ \AA}$, and open circles denote sources with $\text{EW}(\text{H}\alpha) < 2 \text{ \AA}$. Among the H α detections, 24/32 ($75\% \pm 15\%$) lie in the infrared excess region of the *JHK*L color-color diagram. Of the sources which were not detected in H α , 7/26 (27%) lie in the infrared excess region of the color-color

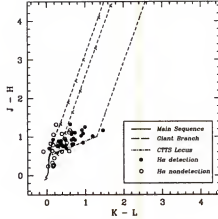


Figure 6-3: The $JHKL$ colors of the $H\alpha$ sources in IC 348. $H\alpha$ data were taken from Herbig (1998). Sources with $H\alpha$ detections are shown as a solid circle, while stars not detected in $H\alpha$ are shown as open circles.

diagram, similar to the number (8/32; 25%) of sources with $H\alpha$ detections which lie in the reddening band.

We divide the $H\alpha$ detections into classical T Tauri stars (CTTS; $EW(H\alpha) \geq 10$ Å) and weak-line T Tauri stars (WTTS; $EW(H\alpha) < 10$ Å) (e.g., Appenzeller & Mundt 1989, Ménard 1999) and show their locations in the $JHKL$ color-color diagram in Figure 6-4. CTTSs are denoted by a filled circle, while WTTSs are shown with an open circle. In the diagram we only plotted those WTTSs with $2 < EW(H\alpha) < 10$ Å. We adopt this range of $H\alpha$ equivalent widths for the WTTSs in our subsequent discussion. Among the $H\alpha$ detections, we identify 17 WTTS and 15 CTTS. All but one (14/15; 93%) of the CTTSs lie in the infrared excess region of the color-color diagram. Among the WTTSs, 10/17 (59%) have $JHKL$ colors indicative of an infrared excess.

6.4 Effects of Source Variability

The L -band observations of IC 348 were taken roughly seven years after the JHK data. Therefore, as was the case with NGC 2024 and the Trapezium, source

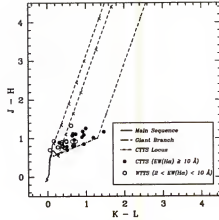


Figure 6-4: The JHK L colors of CTTS and WTTs stars in IC 348. CTTSs are shown as a solid circle, while WTTs are shown as open circles.

variability could affect our derived disk fraction. To investigate the overall effects of variability on our computed disk fraction, we compared the SQUID H -band magnitudes of the 107 sources in our survey with the STELLIRCAM H -band magnitudes acquired in conjunction with our L -band data. Sixteen ($\sim 15\%$) sources had fluxes that differed by more than 0.15 magnitudes. In addition, we matched 104 of our sources (which includes the 16 sources just discussed) with objects in the Herbst et al. (2000) study of variability in IC 348. Ten ($\sim 10\%$) of these were identified as likely variable stars by Herbst et al. (2000). Thus, variability could significantly affect the photometry of 10% to 15% of the sources in the cluster. However, variability would move equal numbers of sources to the right and to the left in the color-color diagram, and therefore one would lose, as well as gain, excess sources. Therefore, on average, this would have only a small effect on the excess fraction. Finally, variability is shown to have a negligible effect on the infrared excesses found in other star forming regions (e.g., Barsony et al. 1997; Lada et al. 2000). We therefore find it very unlikely that source variability is a major factor in producing infrared excesses, and thus has little effect on our derived disk fraction.

As noted in the previous section, eight of the sources detected in $H\alpha$ fall in the reddening band of the *JHK*L color-color diagram, and seven $H\alpha$ nondetections lie in the infrared excess region. Some of the $H\alpha$ detections may have disks, while the nondetections likely do not have disks (see Section 5). Source variability may be responsible for the location of these sources in the *JHK*L diagram. A comparison of the *H*-band STELIRCAM and SQUID magnitudes, in conjunction with the variability measure σ_{var} of Herbst et al. (2000), reveals that 3 of the $H\alpha$ detections and 4 of the $H\alpha$ nondetections have *H*-band magnitudes which differ by ≥ 0.1 magnitude or $\sigma_{\text{var}} > 0.15$ magnitude. Hence, source variability can account for the locations of 7 of the sources in the *JHK*L color-color diagram. Photometric error could be responsible for the location of the 3 remaining $H\alpha$ nondetections with infrared excesses since they are near the reddening band. The location of the remaining 5 sources with $H\alpha$ detections in the reddening band is likely the result of chromospheric activity rather than a disk as discussed in the next section.

6.5 A Disk Census in IC 348

Using our *L*-band photometry in combination with *JHK* observations obtained by Lada & Lada (1995) allowed us to determine a more robust estimate of the circumstellar disk fraction in the IC 348 cluster than previously possible. The infrared excess fraction determined from the *JHK*L color-color diagram for the IC 348 cluster is $65\% \pm 8\%$. Our previous *L*-band and mid-infrared studies of NGC 2024 and the Trapezium demonstrated that the most likely source of the *JHK*L infrared excesses is a circumstellar disk. That the *JHK*L disk fraction in IC 348 is much larger than that inferred from *JHK* colors (20% to 25%; Lada & Lada 1995; Luhman et al. 1998) is consistent with the predictions of circumstellar disk models (Lada & Adams 1992; Meyer et al. 1997) and confirms our results for the NGC 2024 and Trapezium clusters.

Further evidence of a significant circumstellar disk population in the IC 348 cluster comes from the fraction of the $H\alpha$ stars ($75\%\pm 15\%$) which have infrared excesses in the *JHK*L color-color diagram. Most (14/15; 93%) of the stars identified as CTTSs have *JHK*L colors indicative of circumstellar disks. It is interesting, however, that a large fraction (59%) of the sources identified as WTTSs (c.f., those with $2 < EW(H\alpha) < 10 \text{ \AA}$) display infrared excesses. The widely held view is that CTTSs are surrounded by accretion disks while WTTSs are not (e.g., Osterloh & Beckwith 1995; M  nard 1999). Nevertheless, the infrared excesses observed in some of the WTTSs suggests the presence of circumstellar disks surrounding these objects.

Walter & Barry (1991) have shown that, in low mass WTTSs in Taurus-Auriga, chromospheric activity produces $H\alpha$ emission with equivalent widths of ~ 2 to 10 \AA . These authors also show that, in low-mass PMS stars whose $H\alpha$ emission is attributed to circumstellar disks, the equivalent widths can vary widely, from $\sim 2 \text{ \AA}$ to greater than 10 \AA , and can thus have comparable $H\alpha$ equivalent widths to low mass WTTSs whose $H\alpha$ emission is produced by chromospheric activity. Therefore, while low mass PMS stars with $H\alpha$ equivalent widths $\geq 10 \text{ \AA}$ likely have disks, using $H\alpha$ as an indicator of the presence or absence of a circumstellar disk for low mass PMS stars with $2 < EW(H\alpha) < 10 \text{ \AA}$ is ambiguous (stars with $EW(H\alpha) < 2 \text{ \AA}$ probably do not have disks). A similar conclusion was reached by Mart  n (1997).

In Chapter 4, we have shown that $K - L$ colors will identify all disks in a population of young stars. Thus, L -band observations remove the ambiguity which is present in using $H\alpha$ as a disk indicator for stars with $2 < EW(H\alpha) < 10 \text{ \AA}$, and are therefore superior to $H\alpha$ in identifying the presence of disks around young stars. The presence of WTTSs in the infrared excess region of the *JHK*L color-color diagram demonstrates that stars with $2 < EW(H\alpha) < 10 \text{ \AA}$ can have circumstellar disks. The $H\alpha$ emission in the WTTSs which lie in the reddening band is likely due to chromospheric activity in diskless sources. Some WTTSs in Taurus-Auriga also lie in the infrared

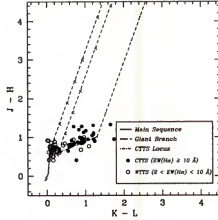


Figure 6-5: The JHK colors of CTTS and WTTS stars in Taurus-Auriga. CTTSs are shown as a solid circle, while WTTSs are shown as open circles. The data were taken from Strom et al. (1989) and Kenyon & Hartmann (1995).

excess region of the JHK color-color diagram. In Figure 6-5, we show the JHK color-color diagram for the CTTSs and WTTSs in the Taurus-Auriga region to the equivalent completeness limit of our IC 348 observations (i.e., corrected for distance). The data used in Figure 6-5 were taken from Strom et al. (1989) and Kenyon & Hartmann (1995). Filled circles represent CTTSs while open circles denote WTTSs (with $2 < EW(H\alpha) < 10 \text{ \AA}$). As in IC 348, some of the WTTSs have infrared colors signifying the presence of a disk. Taken together, these results confirm both earlier indications that WTTS stars are not necessarily diskless (e.g. Brandner et al. 2000), and that $K - L$ colors will identify all disks in a population of young stars, and hence is superior to $H\alpha$ in identifying the presence of disks. We note here that the WTTSs with disks in both IC 348 and Taurus-Auriga do not show infrared excesses in JHK color-color diagrams. Thus, while CTTSs and WTTSs both appear to have disks, the magnitude of the accretion taking place in the disks may differ.

The disk fraction ($65\% \pm 8\%$) in the IC 348 cluster is lower than the disk fractions ($86\% \pm 8\%$ and $80\% \pm 7\%$) in the NGC 2024 and Trapezium clusters respectively. The mean age of the stars in the core of the IC 348 cluster is either 2 Myr or 3 Myr

depending on the cluster distance (320 pc vs. 260 pc), while the NGC 2024 and Trapezium clusters are younger (mean ages of 0.3 Myr and 0.8 Myr respectively). Taken together, these results clearly indicate a decrease in the circumstellar disk fraction with cluster age.

Ages for the individual sources in the IC 348 cluster were determined by Kevin Luhman for cluster distances of 260 pc and 320 pc using the models of D’Antona & Mazzitelli (1997) and luminosities and dwarf temperatures from Luhman et al. (1998) and Luhman 1999. Depending on the adopted distance, sources with circumstellar disks have a median age of 0.9 or 1.7 Myr (± 0.2 Myr), while the diskless sources have a median age of 1.4 or 2.2 Myr (± 0.4 Myr), where the older age corresponds to the closer distance. A Kolmogorov-Smirnov (K-S) test indicates a probability of $p_{K-S} \simeq 0.26$ that the ages of the disk and diskless stars were drawn randomly from the same parent population. While this is only at the 1σ level of significance, this still suggests that the sources without disks are older than those with disks. Furthermore, our results suggest that the timescale for more than a third of the disks in the IC 348 cluster to disappear is ~ 2 to 3 Myr.

We find that 37/68 ($\sim 54\% \pm 9\%$) of the stars in IC 348 which have determined ages have circumstellar disks based on their *JHKL* colors. Strom et al. (1989) and Strom et al. (1993) investigated the disk evolution timescales in the Taurus-Auriga star forming region. Of the 83 sources in these studies with complete *JHKL* photometry and determined ages, 44/78 ($56\% \pm 8\%$) showed infrared excesses indicative of disks. This is the same, to within errors, as the fraction in IC 348. IC 348 represents an environment with a much higher stellar density relative to Taurus-Auriga, where star formation occurs in relative isolation. Furthermore, both regions have similar mean ages. In chapter 4, we have shown that high stellar density does not appear to inhibit the *formation* of circumstellar disks. A comparison of the disk fractions and

source ages in IC 348 and Taurus suggests that, at least in clusters with no O stars, the *disk dissipation timescale* is also independent of the star forming environment.

Published spectral types are available for 80 of the sources in our sample (Luhman et al. 1998). Table 6-1 lists the infrared excess fractions (not corrected for foreground/background contamination) as a function of spectral type (counting from the M5 boundary). Significantly, the circumstellar disk fraction appears to depend on the spectral type, or mass, of the stars in the cluster. None of the stars with spectral types earlier than G appear to have disks. In contrast, $\geq 50\%$ of all stars with spectral types of G and later appear to have disks, with the largest disk fraction (67%) found around the M type stars. A K-S test indicates a very low probability of $p_{K-S} \simeq 4 \times 10^{-8}$ that the disk fractions for the high and low mass stars were drawn randomly from the same parent population. In the younger Trapezium cluster, circumstellar disks appear to form with equally high frequency ($\sim 80\%$) around all stars with spectral types F and later, with a lower, but nevertheless significant, frequency (42%) around stars with earlier OBA spectral types (Lada et al. 2000). These results suggest that, in general, the rate of decline in the circumstellar disk fraction with cluster age is a function of stellar mass such that disks around stars with spectral types earlier than G have shorter lifetimes compared to disks surrounding stars of later spectral types.

Table 6-1: The *JHKL* Excess Fraction vs. Spectral Type

Spectral Type(s) ¹	N_{Region} ²	N_{Excess} ³	<i>JHKLE</i> _{Excess} (%) ⁴
OBAF	9	0	0
G	6	3	50
K	23	12	52
M	42	28	67
All	80	43	54

¹Spectral Types taken from Luhman et al. (1998).

²Number of stars with Spectral Types within survey boundaries.

³Number of stars with Spectral Types and *JHKL* excesses.

⁴Counting from the M5 boundary of the reddening band and using the Cohen et al. (1981) infrared extinction law.

CHAPTER 7

DISK FRACTIONS, LIFETIMES AND PLANET FORMATION

In the last three chapters, we showed that circumstellar disks are a common result of the star formation process. Indeed, most, if not all, stars independent of mass in very young clusters likely form with disks. As the stars in a given cluster age, the disk fraction decreases. The rate of this decrease appears to be a function of stellar mass, where the disks surrounding early spectral type stars have shorter lifetimes than the disks around stars of later spectral type. What is the disk dissipation timescale for young clusters in general?

In this chapter, we investigate the circumstellar disk fractions for our entire cluster sample (with the exception of NGC 2071 and NGC 2068; these clusters are discussed in the next chapter), and search for trends in disk frequency with cluster age and stellar content. We derive a preliminary timescale for disk evolution and examine the question of the overall likelihood of planetary formation in the Galaxy.

7.1 Spatial Distributions

We detected 60 and 37 sources in NGC 2264 and NGC 1960 at L -band with STELIRCAM to the completeness limits for each cluster ($m_L=12.5$ and $m_L=13.0$ respectively). Our NSFCAM observations of the central ~ 28 arcmin² region of the NGC 2362 cluster reveals 95 L -band sources to the completeness limit for the cluster ($m_L=14.0$). In Table 7-1, we summarize the total number of J -, H -, K - and L -band sources detected to the completeness limits of each survey, and which are within the L -band survey region of each cluster (c.f., Table 2-1). The spatial distributions of all

Table 7-1: Number of Sources Detected in Each Cluster

Cluster	<i>J</i> Number	<i>H</i> Number	<i>K</i> Number	<i>L</i> Number
NGC 2024	286	311	343	257
Trapezium	600	695	779	548
IC 348	252	253	242	107
NGC 2264	167	226	243	60
NGC 2362	223	198	176	95
NGC 1960	619	589	417 ¹	37

¹A K_s filter was used for the observations of NGC 1960.

sources to the *L*-band survey completeness limits in each cluster are shown in Figure 7-1.

7.2 Infrared Excess/Circumstellar Disk Fractions

7.2.1 Color-Color Diagrams

In Figures 7-2 – 7-4, we present the *JHK* and *JHKL* color-color diagrams for the NGC 2264, NGC 2362 and NGC 1960 clusters. In the diagrams, we included only those sources in each cluster, which have *K*-band magnitudes equal to or brighter than the completeness limits of the respective *L*-band surveys for each cluster. In all of the color-color diagrams, we plot the locus of points corresponding to the unreddened main sequence as a solid line and the locus of positions of giant stars as a heavy dashed line (Bessell & Brett 1988). The two leftmost parallel dashed lines define the reddening band for main sequence stars and are parallel to the reddening vector. Crosses are placed along these lines at intervals corresponding to 5 magnitudes of visual extinction. The classical T Tauri star (CTTS) locus is plotted as a dot-dashed line (Meyer et al. 1997).

The reddening law of Cohen et al. (1981), derived in the CIT system and having slopes in the *JHK* and *JHKL* color-color diagrams of 1.692 and 2.750 respectively, was adopted.

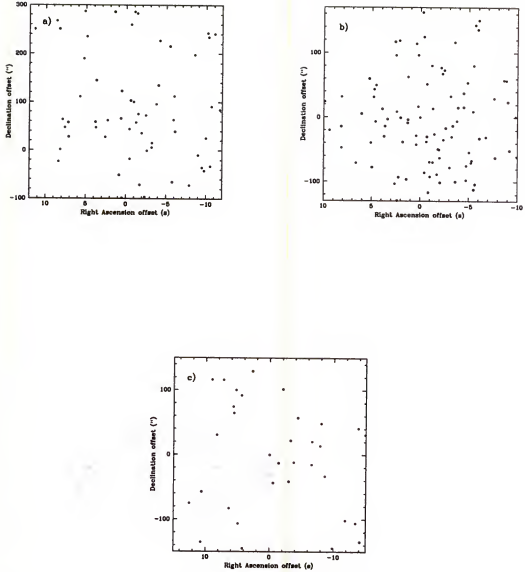


Figure 7-1: Source distributions in NGC 2264, NGC 2362 and NGC 1960. All sources are plotted to the L -band survey completeness limits for each cluster. The clusters are shown as a) NGC 2264, b) NGC 2362 and c) NGC 1960. The offsets are referred to the positions $\alpha=6^h41^m10^s.99$, $\delta=09^\circ56'01''.20$ (2000) for NGC 2264, $\alpha=7^h18^m44^s.25$, $\delta=-24^\circ57'08''.65$ (2000) for NGC 2362 and $\alpha=5^h36^m15^s.81$, $\delta=34^\circ08'36''.54$ (2000) for NGC 1960.

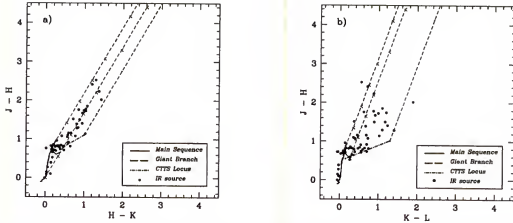


Figure 7-2: The JHK and $JHKL$ color-color diagrams for NGC 2264. The diagrams are shown as a) JHK and b) $JHKL$. Only sources extracted from our STELLRCAM survey with $m_K \leq 12.5$ and $JHKL$ photometric errors less than 10% are plotted. In the diagrams, the locus of points corresponding to the unreddened main sequence is plotted as a solid line, the locus of positions of giant stars is shown as a heavy dashed line and the CTTS locus as a dot-dashed line. The two leftmost dashed lines define the reddening band for main sequence stars and are parallel to the reddening vector. Crosses are placed along these lines at intervals corresponding to 5 magnitudes of visual extinction. The rightmost dashed line is parallel to the reddening band.

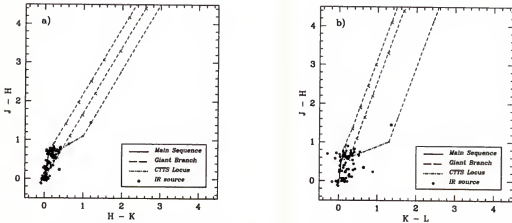


Figure 7-3: The JHK and $JHKL$ color-color diagrams for NGC 2362. The diagrams are shown as a) JHK and b) $JHKL$. Only those sources extracted from the IRAC survey with $m_K \leq 14.0$ and $JHKL$ photometric errors less than 10% are plotted. In the diagrams, the locus of points corresponding to the unreddened main sequence is plotted as a solid line, the locus of positions of giant stars is shown as a heavy dashed line and the CTTS locus as a dot-dashed line. The two leftmost dashed lines define the reddening band for main sequence stars and are parallel to the reddening vector. Crosses are placed along these lines at intervals corresponding to 5 magnitudes of visual extinction. The rightmost dashed line is parallel to the reddening band.

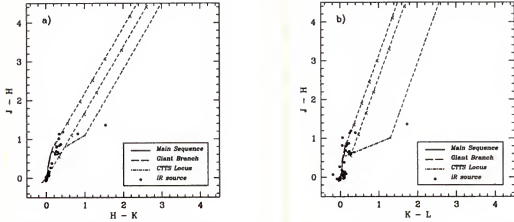


Figure 7-4: The JHK and $JHKL$ color-color diagrams for NGC 160. The diagrams are shown as a) JHK and b) $JHKL$. Only those sources extracted from the 2MASS survey with $m_K \leq 13.0$ and $JHKL$ photometric errors less than 10% are plotted. In the diagrams, the locus of points corresponding to the unreddened main sequence is plotted as a solid line, the locus of positions of giant stars is shown as a heavy dashed line and the CTTS locus as a dot-dashed line. The two leftmost dashed lines define the reddening band for main sequence stars and are parallel to the reddening vector. Crosses are placed along these lines at intervals corresponding to 5 magnitudes of visual extinction. The rightmost dashed line is parallel to the reddening band.

A significant fraction of the cluster sources fall outside and to the right of the reddening lines in the infrared excess region of the color-color diagrams. In Table 7-2, we present the JHK and $JHKL$ infrared excess fractions in each of our sample clusters, as well as the stellar mass (using D'Antona & Mazzitelli 1998 PMS tracks) corresponding to the respective completeness limits in each cluster. The excess fractions were corrected for field star contamination using control fields as described in Chapters 4 and 6, using mean extinctions of $A_K=0.5$, 0.0 and 0.0 for NGC 2264 (Lada et al. 1993), NGC 2362 and NGC 160 respectively. As was the case with NGC 2024, the Trapezium and IC 348, the excess fractions were calculated assuming the boundary of the reddening band in the $JHKL$ and JHK diagrams passes through M5 and A0 colors from Bessell & Brett (1988) respectively. Note that these colors were adopted for all of the sample clusters for consistency in comparing disk

fractions, although as we can see from Table 7-2, we are not complete to M5 colors in NGC 2264, NGC 2362 and NGC 1960.

Recall that the frequency of near-infrared excess sources determined from color-color diagrams also depends on the adopted reddening law and the photometric system used to plot the positions of the main sequence stars and the reddening bands. For each cluster, we calculated the *JHKL* infrared excess fraction for two other reddening laws obtained in different photometric systems (Koornneef 1983; RL85), and find that the *JHK* and *JHKL* excess fractions are within the quoted (statistical) error of our determination using a Cohen et al. (1981) reddening law. Finally, we note that since the extinctions in NGC 2264 are typically less than $A_V=10$ magnitudes, and those in NGC 2362 and NGC 1960 are essentially zero, the $3.08\ \mu\text{m}$ ice feature will produce little, if any, effect on our *L* band photometry.

7.2.2 Effects of Source Variability

The NGC 2264 *JHKL* data were taken simultaneously, so source variability will have a negligible effect on the derived disk fraction. However, variability could affect our derived disk fractions in NGC 2362 and NGC 1960 since the *L*-band observations were taken a year or more after the *JHK* data. In NGC 2362, there are a number of sources which lie to the right of the locus of main sequence colors in the *JHKL* diagram. Variability may be responsible for this, and hence the actual disk fraction may be somewhat lower than our derived disk fraction. To investigate the overall effects of variability on our computed disk fraction in NGC 1960, we compared the adopted *H*-band magnitudes of all sources in the cluster with STELIRCAM *H*-band magnitudes acquired in conjunction with our *L*-band data. Approximately 10% of the sources had fluxes which differed by more than 0.15 magnitudes. However, as we have previously noted, variability would cause an equal number of sources to be pushed into the forbidden and excess regions of the color-color diagram. As we can see from an examination of the color-color diagram for NGC 1960, this is not the

Table 7-2: The *JHK* and *JHKL* Infrared Excess Fractions

Cluster	<i>JHK</i> Excess Fraction ¹	<i>JHKL</i> Excess Fraction ¹	Mass (M_{\odot}) ²
NGC 2024	76/131 (58% \pm 7%)	112/131 (85% \pm 8%)	0.13
Trapezium	195/391 (50% \pm 4%)	312/391 (80% \pm 5%)	0.16
IC 348	19/91 (21% \pm 5%)	59/91 (65% \pm 8%)	0.19
NGC 2264	12/50 (24% \pm 7%)	26/50 (52% \pm 10%)	0.85
NGC 2362	3/75 (4% \pm 2%)	9/75 (12% \pm 4%)	1.00
NGC 1960	2/37 (5% \pm 4%)	1/37 (3% \pm 3%)	1.30

¹A K_s filter was used for the observations of NGC 1960.

²Mass of a star at the completeness limit for each cluster.

case. We therefore conclude that source variability has little effect on our derived disk fractions, except possibly the *JHKL* excess fraction in NGC 2362.

7.3 Disk Fractions, Lifetimes and Planet Formation

In Figure 7-5, we show the *JHK* and *JHKL* disk fractions for each cluster as a function of mean cluster age. The dot-dashed line in each plot represents a least squares fit to the data. The short dash - long dashed line represents the least squares fit to the data assuming an age of 2 Myr for NGC 2264 (the open triangle in each plot; Section 7.3.1). Vertical error bars represent the statistical errors in our derived disk fractions. Horizontal error bars show the errors of our adopted ages. NGC 1960 is not included in the figure since our observations of this cluster only extend to $>1 M_{\odot}$ stars, whereas in the other clusters we are complete to $\leq 1.0 M_{\odot}$. We also plot disk fractions in Taurus (open triangle) and λ Ori (open circle). The disk fractions for Taurus were derived in Chapter 4 from the data of Kenyon & Hartmann (1995). The disk fraction for the λ Ori cluster is based on $H\alpha$ data from Dolan & Mathieu (1999). Those sources with $EW(H\alpha) > 12 \text{ \AA}$ were counted as having disks. The *JHKL* disk fractions in each cluster are much larger than those inferred from *JHK* colors, consistent with the predictions of circumstellar disk models (Lada & Adams 1992; Meyer et al. 1997) and our previous results for the NGC 2024, Trapezium and IC

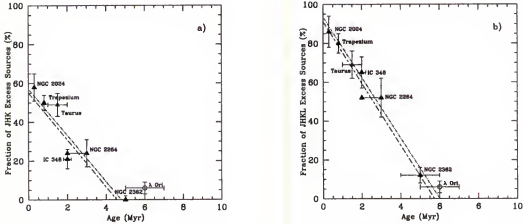


Figure 7-5: The *JHK* and *JHKL* excess fractions vs. cluster age. The diagrams are shown as a) *JHK* and b) *JHKL*. The dot-dashed line in each plot represents a least squares fit to the data. The short dash - long dashed line represents the least squares fit to the data assuming an age of 2 Myr for NGC 2264 (the open triangle in each plot). Vertical error bars represent the statistical errors in our derived disk fractions. Horizontal error bars show the errors of our adopted ages. NGC 1960 is not included in the figure since our observations of this cluster only extend to $>1 M_{\odot}$ stars, whereas in the other clusters we are complete to $\leq 1.0 M_{\odot}$. We also plot disk fractions in Taurus (open triangle) and λ Ori (open circle). The disk fractions for Taurus were derived in Chapter 4 from the data of Kenyon & Hartmann (1995). The disk fraction for the λ Ori cluster is based on $H\alpha$ data from Dolan & Mathieu (1999).

348 clusters. Before investigating disk lifetimes based on this diagram, we look more closely at the ages for each cluster and, more specifically, the methods by which the ages were determined.

7.3.1 Cluster Ages

All ages for the clusters in Figure 7-5 were extracted from the literature. Mean cluster ages are plotted in Figure 7-5 for the NGC 2024, Trapezium, IC 348 and NGC 2264 clusters. These ages were determined using published pre-main sequence (PMS) evolutionary tracks for stars of different masses. In particular, the ages of the NGC 2024 and Trapezium clusters were derived using the models of D'Antona & Mazzitelli (1994; hereafter DM94). The age of the IC 348 cluster was determined from the models of D'Antona & Mazzitelli (1997,1998; hereafter DM98), while the

age of NGC 2264 was determined using the models of Bernasconi & Maeder (1996; hereafter BM) for stars with $M > 0.8 M_{\odot}$ and Swenson et al. (1994; hereafter S94) (their model F) for stars with $M \leq 0.8 M_{\odot}$.

At this point, we note that Hillenbrand (1997) showed that these age determinations must be viewed with appropriate caution since absolute stellar age calibrations can be very uncertain due to (1) differences in the predictions of the various theoretical models (arising from differences in the input physics, such as convection models, opacities and equations of state between the models), and (2) uncertainties in the luminosity at which a star of a particular temperature (or the radius at which a star of a particular mass) begins its PMS contraction phase. Age differences of several Myr or more can be obtained depending on which PMS models are adopted. In addition, for a given cluster, stars having masses of 1 to $10 M_{\odot}$ appear systematically older (according to *any* adopted set of tracks) than those stars in the 0.1 to $1.0 M_{\odot}$ mass range.

The DM98 tracks incorporate advancements to the opacity table, the treatment of convection and the equation of state as compared to the models of DM94. The DM94 and DM98 models yield similar results until a stellar mass of $M \simeq 0.3 M_{\odot}$. For lower mass stars and young brown dwarfs, the DM98 tracks return larger luminosities (and hence younger ages) compared to DM94. However, the luminosity difference between the models for a 2 to 3 Myr old star (the mean age of IC 348) at the hydrogen burning limit is $\log(L/L_{\odot}) < 0.1$, which corresponds to an age difference of less than 1 Myr.

The ages derived using the tracks of BM and S94 are similar up to a $1 M_{\odot}$. For more massive stars, the BM tracks yield systematically greater ages (Sung et al. 1997). Hillenbrand (1997) derived a relationship between the S94 and DM94 tracks. To illustrate the age difference found using these tracks, the NGC 2264 cluster has a mean age of 3 Myr based on the S94 tracks. This translates into a mean age of 2

Myr using DM94. Thus it appears that we can compare the ages for the NGC 2024, Trapezium, IC 348 and NGC 2264 clusters to within about 1 Myr.

Finally we note that the the ages of NGC 2362 and NGC 1960 were determined from main sequence isochrone fitting in the H-R diagram. In particular, the age of NGC 2362 (5 ± 1 Myr) was determined by fitting an isochrone to the O7 star in the cluster (Balona & Laney 1996). The age of NGC 1960 (~ 30 Myr) was determined by fitting isochrones to the turn-off point of the stars on the main sequence (Barkhatova et al. 1985, Sanner et al. 2000). With the different methods and uncertainties in the age determinations for each cluster in mind, we now proceed to discuss the disk fractions and lifetimes for the cluster sample.

7.3.2 Disk Fractions and Lifetimes

As we can see from Figure 7-5, the disk fraction decreases with increasing cluster age. In the IC 348 cluster, and possibly even in the Trapezium, this rate of decrease was found to be a function of stellar mass. Is there evidence of this in the NGC 2264, NGC 2362 and NGC 1960 clusters as well? The most straightforward way to investigate this question is to examine the spectral types for the individual stars in each cluster. Spectral types are available for some of the stars in NGC 2264 (e.g. Perez et al. 1987; Walker 1956), however they do not correspond to the stars in our survey. Spectral types for the other two clusters are either unaccessible (for NGC 2362) or not available (for NGC 1960). However, J -band magnitudes are sensitive to the stellar photospheres (more so than either H or K -band magnitudes), and may therefore yield insight into the masses of the sources in each cluster. Is there a correlation between J -band magnitudes and spectral type?

Spectral types and J -band magnitudes are available for many sources in the IC 348 cluster. In Figure 7-6, we plot the spectral types of the stars in the IC 348 cluster as a function of J -band magnitude. In the left panel, we plot the stars with spectral types of OBAFG as an unshaded histogram and the stars of spectral type

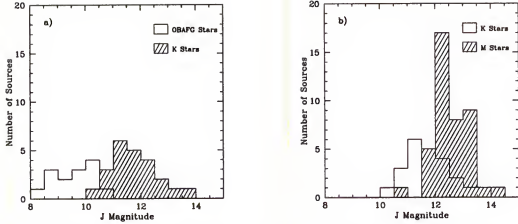


Figure 7-6: Plot of J -band magnitude vs. spectral type in IC 348. Plots are for the a) OBAFGK stars and b) KM stars in the cluster. The shaded region in a) represents stars with spectral type K, while in b) the shaded region represents the M stars. The stars with the latest spectral types have the faintest J -band magnitudes.

K as a shaded histogram. In the right panel, the stars of spectral type K are shown as an unshaded histogram, while the stars with M spectral types are plotted as a shaded histogram. We can see that the stars with the latest spectral types have the faintest J -band magnitudes. Thus, there does appear to be a correlation between the J -band magnitudes of cluster stars and their masses.

In Figure 7-7, we show the J -band luminosity functions of the NGC 2264 and NGC 2362 clusters. The shaded region in each diagram represents those sources which have circumstellar disks. We have not included the NGC 1960 cluster since our survey of this cluster is only complete to stars with masses of $\sim 1.3 M_{\odot}$, and the disk fraction is found to be 0%. Since the stars with disks in NGC 2264 span a large range in J -band magnitude, it is not clear whether most of the disked stars are of low mass. In NGC 2362, however, the stars with disks are among the faintest at J -band. Since the J -band magnitudes appear to be correlated with stellar mass, these stars have the lowest stellar masses in the NGC 2362 cluster. Thus, in conjunction with the results for IC 348 and the Trapezium, it appears that a shorter lifetime for

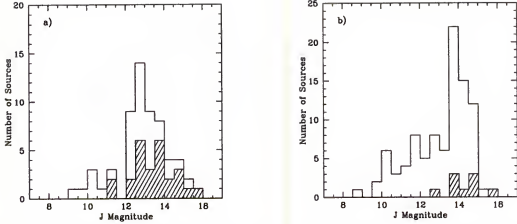


Figure 7-7: The J -band luminosity functions for NGC 2264 and NGC 2362. The plots are shown as a) NGC 2264 and b) NGC 2362. The shaded region in each diagram represents those sources which have circumstellar disks.

disks surrounding high mass stars as compared to lower mass stars may be a general property in young clusters.

The decrease in the disk fraction continues until about 6 Myr, at which point it appears that all of the stars have lost their disks. This age cannot be taken literally given the uncertainties in determining absolute cluster ages (as discussed previously), the paucity of older clusters in our sample and the fact that our adopted age for NGC 2362 is based on the age of the O star in the cluster rather than a mean age (which would make the cluster appear younger). Nevertheless, the very low disk fraction for λ Ori (mean age ~ 6 Myr) supports a disk lifetime of approximately 6 Myr. We therefore consider 6 Myr to be an approximate upper limit on the inner disk dispersal timescale in clusters.

We have already seen that, in IC 348, $\sim 35\%$ of the disks, independent of stellar mass, disappeared in ~ 2 to 3 Myr depending on the adopted distance to the cluster. Assuming a linear decline in the disk dispersal timescale implies a disk lifetime of ~ 5.5 to 8.5 Myr. Combined with our upper limit on the disk lifetime, we estimate that the inner disk dispersal timescale in young stellar clusters is ~ 5.5 to 6.0 Myr. As we can see from Figure 7-5, this timescale does not change if we use a mean age

of 2 Myr (derived using DM98 PMS tracks) for NGC 2264. Our derived timescale corresponds to the dissipation timescale for the optically thick disks around all stars in a given cluster (e.g., those in which most of the formation of planets takes place).

7.3.3 Implications for Planet Formation

To date, ~ 50 very low mass companions have been found in spectroscopic surveys of nearby solar-type stars (Marcy et al. 2000). These objects are thought to be gas giant planets similar to Jupiter, and many ($\sim 75\%$) have masses in the range 1 to 10 Jupiter masses (M_J). How does our inferred timescale for disk dissipation of 5.5 to 6.0 Myr compare to the timescale required for giant planet formation from theoretical models?

According to the leading model of giant planet formation, the core accretion model, a high density (rocky) core with a mass of ~ 10 Earth masses (M_\oplus) must form first. This requires at least 1 Myr, and another ~ 10 Myr are then required to accrete $\sim 300 M_\oplus$ of nebular gas (Lissauer 1987; Pollack et al. 1996). In a more recently reinstated model by Boss (1998, 2000), a gravitationally unstable protoplanetary disk (of $M_{disk} \sim 0.1 M_\odot$ within a radius of 20 AU) can fragment into self-gravitating clumps and form gas giant planets on timescales as short as 10^3 yr. However, we note that the calculations to date using this model assume “locally isothermal” thermodynamics (i.e., the initial radial temperature profile is held constant) which strongly favors clumping. The survival of these clumps likely depends on a proper treatment of their thermodynamical evolution (Boss 2000).

Clearly, the disk lifetime in clusters (5.5 to 6.0 Myr) is long enough for gas giant planets to form via the Boss model (keeping in mind that further work is needed on this model). However, the total time required to form the gas giant planets via the core accretion model is more problematical. The situation is even worse for the highest mass stars, since these stars appear to lose their disks on an even shorter timescale (< 2 to 3 Myr).

The disk dispersal timescale of 5.5 to 6.0 Myr is the timescale for the *inner* disk (less than about 1 AU) to disappear. The dispersal timescale for the *outer* disk (>10 AU), which contains the bulk of the mass available to form planets, may be different (e.g., Lada et al. 2001, in preparation). Millimeter observations of statistically significant samples of YSOs in a number of young clusters to determine outer disk lifetimes and disk masses would be very beneficial to providing further insight into the likelihood of planetary formation in the Galaxy.

CHAPTER 8

THE NGC 2071 AND NGC 2068 CLUSTERS

In this chapter, we briefly examine the NGC 2071 and NGC 2068 clusters. Since the ages of these clusters are not well known, we discuss them separately here. We examine the disk fraction in the clusters and infer ages based on the derived fractions.

8.1 Spatial Distribution

We detected 54 and 60 sources in NGC 2071 and NGC 2068 at L -band with STELIRCAM to the completeness limits for both clusters ($m_L=12.0$). We summarize in Table 8-1 the total number of J -, H -, K - and L -band sources detected to the completeness limit of both clusters, and which are within the region covered by our STELIRCAM observations (c.f., Table 2-1). The spatial distributions of all sources to the L -band survey completeness limit in both clusters are shown in Figure 8-1.

8.2 Infrared Excess/Circumstellar Disk Fractions

8.2.1 Color-Color Diagrams

In Figures 8-2 and 8-3, we present the JHK and $JHKL$ color-color diagrams for the NGC 2071 and NGC 2068 clusters. In the diagrams, we included only those sources in each cluster, which have K -band magnitudes equal to or brighter than the

Table 8-1: Number of Sources Detected in Each Cluster

Cluster	J Number	H Number	K Number	L Number
NGC 2071	110	138	150	54
NGC 2068	263	280	253	60

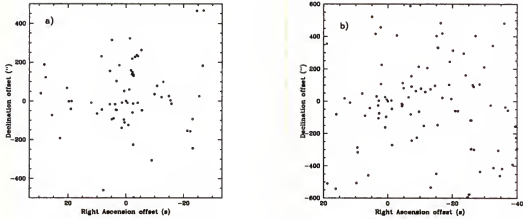


Figure 8-1: Source distributions in NGC 2071 and NGC 2068. Sources to the L -band survey completeness limits for both clusters are shown. The clusters are shown as a) NGC 2071 and b) NGC 2068. The offsets are referred to the positions $\alpha=5^h46^m57^s.32$, $\delta=00^\circ20'09''.62$ (2000) for NGC 2071 and $\alpha=5^h46^m45^s.28$, $\delta=00^\circ02'41''.99$ (2000) for NGC 2068.

completeness limits of the respective L -band surveys for each cluster. We plot the locus of points corresponding to the unreddened main sequence as a solid line and the locus of positions of giant stars as a heavy dashed line (Bessell & Brett 1988). The two leftmost parallel dashed lines define the reddening band for main sequence stars and are parallel to the reddening vector. Crosses are placed along these lines at intervals corresponding to 5 magnitudes of visual extinction. The classical T Tauri star (CTTS) locus is plotted as a dot-dashed line (Meyer et al. 1997). The reddening law of Cohen et al. (1981), derived in the CIT system and having slopes in the JHK and $JHKL$ color-color diagrams of 1.692 and 2.750 respectively, was adopted.

In Table 8-2, we present the JHK and $JHKL$ infrared excess fractions in each of our sample clusters, as well as the mass corresponding to the respective completeness limits in each cluster. The excess fractions were corrected for field star contamination using control fields as described in Chapters 4, 6 and 7, using a mean extinction of $A_K=1.5$, 0.0 and 0.0 for both clusters. Again, the excess fractions were calculated assuming the boundary of the reddening band in the $JHKL$ and JHK diagrams pass

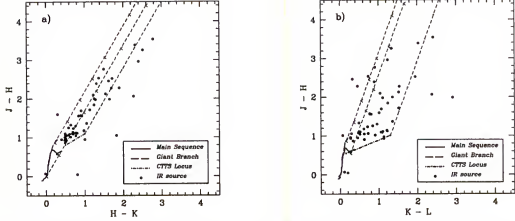


Figure 8-2: The JHK and $JHKL$ color-color diagrams for NGC 2071. The plots are shown as a) JHK and b) $JHKL$. Only those sources extracted from our STELIRCAM survey with $m_K \leq 12.0$ and $JHKL$ photometric errors less than 10% are plotted. In the diagrams, the locus of points corresponding to the unreddened main sequence is plotted as a solid line, the locus of positions of giant stars is shown as a heavy dashed line and the CTTS locus as a dot-dashed line. The two leftmost dashed lines define the reddening band for main sequence stars and are parallel to the reddening vector. Crosses are placed along these lines at intervals corresponding to 5 magnitudes of visual extinction. The rightmost dashed line is parallel to the reddening band.

through M5 and A0 colors from Bessell & Brett (1988) respectively. Note that these colors were adopted for consistency in comparing disk fractions.

8.2.2 Effects of Source Variability

Source variability could affect our derived disk fractions in NGC 2071 and NGC 2068 since the L -band observations were taken a year or more after the JHK data. To investigate the overall effects of variability on our computed disk fractions in these clusters, we compared the adopted SQIID H -band magnitudes of the 50 sources in our survey of both clusters with the STELIRCAM H -band magnitudes acquired in conjunction with our L -band data. Six (12%) of the NGC 2071 sources and 7 (14%) of the NGC 2068 sources had fluxes which differed by more than 0.15 magnitudes. However, as previously noted, variability would cause an equal number of sources to be pushed into the forbidden and excess regions of the color-color diagram. As we can see from an examination of the color-color diagrams, this is not the case in either

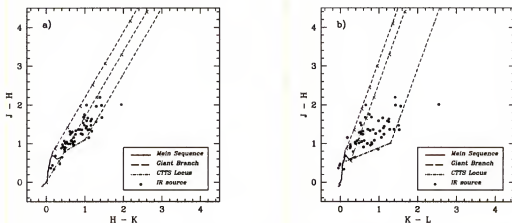


Figure 8-3: The JHK and $JHKL$ color-color diagrams for NGC 2068. The plots are shown as a) JHK and b). Only those sources extracted from our STELLRCAM survey with $m_K \leq 12.0$ and $JHKL$ photometric errors less than 10% are plotted. In the diagrams, the locus of points corresponding to the unreddened main sequence is plotted as a solid line, the locus of positions of giant stars is shown as a heavy dashed line and the CTTS locus as a dot-dashed line. The two leftmost dashed lines define the reddening band for main sequence stars and are parallel to the reddening vector. Crosses are placed along these lines at intervals corresponding to 5 magnitudes of visual extinction. The rightmost dashed line is parallel to the reddening band.

Table 8-2: The JHK and $JHKL$ Infrared Excess Fractions

Cluster	JHK Excess Fraction	$JHKL$ Excess Fraction	Mass (M_\odot) ¹
NGC 2071	26/50 (52% \pm 10%)	37/50 (74% \pm 12%)	0.17
NGC 2068	25/50 (50% \pm 10%)	35/50 (70% \pm 12%)	0.17

¹Mass of a star at the completeness limit for each cluster.

cluster. We therefore conclude that source variability has little effect on our derived disk fractions.

8.3 Inferred Ages for NGC 2071 and NGC 2068

The disk fractions we derive for the NGC 2071 and NGC 2068 clusters are intermediate to those of NGC 2024, Trapezium and IC 348. An examination of Figure 7-5 shows that a cluster with a disk fraction of 70% to 75% would have a mean age of ~ 1.5 Myr. We note that the disk fraction for NGC 2068 is slightly smaller than that for NGC 2071, suggesting that NGC 2068 may be somewhat older, although within

the errors their ages are the same. Thus, we infer a mean age of ~ 1.5 Myr for both NGC 2071 and NGC 2068.

These results are supported by the millimeter studies of Launhardt et al. (1996) and Lada et al. (1997). Multitransition CS observations of massive dense cores in the L1630 molecular cloud by Lada et al. (1997) show that NGC 2071 and NGC 2024 have both a high density and a large fraction of mass at high density, while NGC 2068 lacks these properties. In addition, NGC 2068 does not have the high column density of NGC 2024 or NGC 2071. It is possible that these observations could be due to differing evolutionary states among the regions. For example, the NGC 2068 core may be the remnant of the core that formed the cluster. This is supported by the lack of high density gas.

A difference in the evolutionary states between the clusters is also supported by the $\lambda=1.3$ mm dust emission survey of L1630 by Launhardt et al. (1996). The NGC 2071 cluster is found to contain less gas mass (ie. less mass available to form stars) than NGC 2024, and thus appears to be more evolved. Unlike these two clusters, NGC 2068 is found to have no intense dust emission, indicating that most of the gas mass of this core already was transformed into stars. This suggests that NGC 2068 is at a more advanced evolutionary state than either NGC 2071 or NGC 2024.

However, as previously noted, the disk fractions in the NGC 2071 and NGC 2068 clusters are the same within the errors, indicating that they may have similar ages. Clearly a determination of the mean ages of these clusters is desirable. This will be possible once spectra for many sources in both clusters are obtained from future observations with *Flamingos*, a new near-infrared imager and multi-object spectrometer designed and built at the University of Florida by Dr. Richard Elston.

CHAPTER 9 CONCLUSIONS

We conducted the first extensive program of L -band imaging surveys of eight nearby young clusters. The clusters span a range of ages (≤ 1 to 30 Myr) and environments (e.g., stellar density and stellar content). The aims of this study were to determine the circumstellar disk fraction in each cluster, investigate the dependence of the disk fraction on cluster age and environment, and evaluate the overall likelihood of planet formation in the Galaxy.

9.1 Disk Formation

Most of the stars which formed in the youngest clusters were surrounded by circumstellar disks, and these disks are still present around these sources. That the disk fractions remain very high to within the errors at the faintest L band magnitudes, and over a large range of spectral types, suggests that the disk formation occurs *independent* of stellar mass. A comparison of the disk fractions in the NGC 2024 and Trapezium clusters with the disk fraction in the Taurus star forming region (i.e., cluster vs. isolated environments) shows that disks also form around most of the YSOs in star forming regions *independent* of environment. Thus it appears that disk formation is quite common in the Galaxy, and therefore most stars are born with the potential of having future attendant planetary systems.

Our mid-infrared observations of NGC 2024 verify a high circumstellar disk fraction in this cluster demonstrating that JHK_L color-color diagrams are a very efficient tool in estimating circumstellar disk fractions in young clusters. In addition, we find that observations at L -band are not as susceptible as those at K -band to the

effects of bright nebulosity present in the central regions of the youngest clusters, and hence provide further evidence that *L*-band observations better represent the disk fractions in clusters.

9.2 Disk Evolution and Planet Formation

We find that the disk fraction for sources in the IC 348 cluster and Taurus-Auriga (which have similar mean ages) is the same, to within the errors. IC 348 represents an environment with a much higher stellar density relative to Taurus-Auriga, where star-formation occurs in relative isolation, suggesting that, at least in clusters with no massive stars, disks are not preferentially destroyed in dense cluster environments.

The overall disk fraction in each cluster decreases with increasing cluster age. Not only does the disk fraction decline with cluster age, but the rate of the decline also appears to be a function of stellar mass, such that disks surrounding high-mass stars have shorter lifetimes as compared to disks surrounding lower-mass stars.

The decrease in the disk fraction continues until an age of ~ 5.5 to 6.0 Myr, at which point it appears that all of the stars have lost their disks. This corresponds to the transition timescale for disks around all stars in a given cluster to evolve from optically thick disks, in which most of the formation of planets takes place, to optically thin disks. Our derived disk dissipation timescale is long enough for gas giant planets to form via the Boss (1998, 2000) model, however the total time required to form the gas giant planets via the more generally accepted core accretion model is more problematical. The situation is even worse for the highest-mass stars, since these stars appear to lose their disks on even shorter timescales (< 2 to 3 Myr).

Finally, we note that our derived disk dissipation timescale corresponds to that for the *inner* disk. The dispersal timescale for the *outer* disk, which contains the bulk of the mass available to form planets, may be different. Future millimeter

observations of statistically significant samples of YSOs in a number of young clusters to determine outer disk lifetimes and disk masses would be very beneficial to providing further insight into the likelihood of planetary formation in the Galaxy.

CHAPTER 10 FUTURE WORK

There is a need to continue this study by including *L*-band observations of more clusters with ages between 3 to 10 Myr. In addition, since there is much scatter in the *JHK**L* color-color diagram for NGC 2362, particularly around the main sequence, it would be useful to repeat the observations of this cluster. Knowledge of the disk fraction for NGC 2362, and for clusters in the 3 to 10 Myr age range, is particularly important since such clusters have ages very near our derived disk dissipation timescale. Further *L*-band observations of clusters in this age range are also needed to investigate the very interesting result that the decline in disk frequency may also be a function of stellar mass, because the statistics are not robust enough to be definitive on this point, particularly with regard to the higher-mass stars. Furthermore, our *L*-band observations of the NGC 1960 cluster should be extended to include fainter, lower-mass objects.

Accurate mean age estimates are crucial to determining the disk dissipation timescale. Observations with *Flamingos* will allow us to obtain spectra of a large number of sources in each of our sample clusters and determine mean cluster ages using the same set of PMS tracks. This is particularly important for the NGC 2362 cluster since its mean age is currently based on the turnoff point of the O star on the main sequence. These observations will yield a self-consistent determination of the cluster ages, and hence a more meaningful estimate of the disk lifetimes in young (≤ 10 Myr) clusters.

We identified many protostellar candidates in the NGC 2024 and Trapezium clusters, however an unambiguous identification of these objects as true protostars

cannot be made from our near-infrared data alone. Mid-infrared observations of these objects using, for example, OSCIR on Gemini North, would enable such a determination. This would allow an accurate assessment of the numbers and lifetimes of the protostellar population in each cluster. In addition, combined near- and mid-infrared data would make possible a study of the multiplicity of self-embedded young stars, about which little is currently known.

Extremely little is also known about the stellar properties of protostars. A high resolution spectroscopic survey of the protostars identified in the previously mentioned mid-infrared study could yield spectral types, surface gravities, rotation information and effective temperatures for each object. In conjunction with luminosities determined from the near-infrared photometry presented in this thesis, we could, for the first time, place these objects in the H-R diagram. This would allow us to perform a unique analysis of the masses, ages and radii of these objects.

Finally, millimeter observations of statistically significant samples of YSOs in a number of young clusters to determine outer disk lifetimes and disk masses would be very beneficial to providing further insight into the likelihood of planetary formation in the Galaxy.

APPENDIX A
THE *JHK*L POSITIONS AND PHOTOMETRY FOR NGC 2024

Table A-1: The *JHK*L Photometry of NGC 2024 Sources

ID	RA (2000) ¹	Dec (2000) ¹	J	H	K	L	(J-H)	(H-K)	(K-L)
1	5 41 45.78	-1 54 31.44	11.14	7.65	5.75	2.10	3.49	1.90	3.65
2	5 41 37.82	-1 54 38.65	7.99	7.55	6.50	5.60	0.44	1.05	0.90
3	5 41 39.00	-1 52 09.71	11.53	9.11	7.46	5.71	2.42	1.65	1.75
4	5 41 37.67	-1 53 53.50	10.71	9.16	8.30	7.70	1.55	0.86	0.60
5	5 41 50.49	-1 53 15.63	09.59	8.81	8.36	8.02	0.78	0.45	0.34
6	5 41 37.19	-1 49 55.38	11.88	9.99	8.56	7.02	1.89	1.43	1.54
7	5 41 38.50	-1 53 24.68	10.88	9.45	8.59	7.99	1.43	0.86	0.60
8	5 41 37.25	-1 53 15.38	10.26	9.27	8.61	7.89	0.99	0.66	0.72
9	5 41 46.71	-1 49 58.35	10.96	9.66	8.84	7.70	1.30	0.82	1.14
10	5 41 44.80	-1 54 26.48	13.02	10.59	8.85	7.11	2.43	1.74	1.74
11	5 41 39.03	-1 54 00.25	12.17	10.29	8.93	7.88	1.88	1.36	1.05
12	5 41 36.19	-1 54 26.58	12.38	10.51	9.01	7.20	1.87	1.50	1.81
13	5 41 51.02	-1 55 07.66	12.21	10.40	9.09	7.20	1.81	1.31	1.89
14	5 41 41.79	-1 57 55.99	12.30	10.43	9.15	7.93	1.87	1.28	1.22
15	5 41 55.59	-1 52 18.26	12.71	10.37	9.18	8.38	2.34	1.19	0.80
16	5 41 38.16	-1 53 11.07	11.95	10.18	9.20	8.51	1.77	0.98	0.69
17	5 41 38.23	-1 50 40.37	12.25	10.39	9.23	7.99	1.86	1.16	1.24
18	5 41 34.87	-1 55 21.27	10.75	9.82	9.27	8.81	0.93	0.55	0.46
19	5 41 33.73	-1 53 25.91	11.52	10.13	9.30	8.02	1.39	0.83	1.28
20	5 41 45.13	-1 54 48.41	14.32	11.57	9.37	7.46	2.75	2.20	1.91
21	5 41 39.14	-1 54 16.19	13.60	11.24	9.43	7.44	2.36	1.81	1.99
22	5 41 47.98	-1 59 04.74	12.89	10.89	9.45	7.43	2.00	1.44	2.02
23	5 41 39.41	-1 53 28.73	13.19	11.00	9.54	8.15	2.19	1.46	1.39
24	5 41 44.44	-1 55 24.52	13.19	11.17	9.60	8.19	2.02	1.57	1.41
25	5 41 36.53	-1 53 56.86	11.93	10.40	9.62	9.17	1.53	0.78	0.45
26	5 41 36.75	-1 54 01.18	12.07	10.59	9.65	8.88	1.48	0.94	0.77
27	5 41 37.82	-1 53 13.26	11.67	10.36	9.67	9.37	1.31	0.69	0.30
28	5 41 40.10	-1 53 35.95	14.11	11.72	9.76	7.90	2.39	1.96	1.86
29	5 41 31.91	-1 55 22.16	12.30	10.72	9.79	8.85	1.58	0.93	0.94
30	5 41 23.99	-1 49 38.79	10.37	9.98	9.85	9.61	0.39	0.13	0.24
31	5 41 34.46	-1 54 43.71	11.72	10.59	9.96	9.55	1.13	0.63	0.41
32	5 41 29.45	-1 54 29.07	11.73	10.61	10.00	9.30	1.12	0.61	0.74
33	5 41 46.19	-1 53 47.58	13.68	11.46	10.12	9.19	2.22	1.34	0.93

Table A-1-continued

ID	RA (2000) ¹	Dec (2000) ¹	J	H	K	L	(J-H)	(H-K)	(K-L)
34	5 41 45.74	-1 54 50.67	13.79	11.96	10.16	9.05	1.83	1.80	1.11
35	5 41 44.83	-1 54 37.22	14.18	12.02	10.20	8.64	2.16	1.82	1.56
36	5 41 52.27	-1 57 17.50	12.87	11.23	10.20	9.03	1.64	1.03	1.17
37	5 41 37.58	-1 54 26.98	12.51	11.12	10.24	9.70	1.39	0.88	0.54
38	5 41 53.31	-1 57 43.52	13.46	11.65	10.25	8.55	1.81	1.40	1.70
39	5 41 41.94	-1 54 25.68	14.32	12.03	10.26	8.40	2.29	1.77	1.86
40	5 41 44.95	-1 51 46.01	14.21	11.73	10.33	9.43	2.48	1.40	0.90
41	5 41 46.96	-1 50 36.52	12.54	11.23	10.41	9.30	1.31	0.82	1.11
42	5 41 34.31	-1 53 21.90	12.65	11.20	10.42	9.38	1.45	0.78	1.04
43	5 41 53.95	-1 55 16.42	14.03	11.95	10.42	8.44	2.08	1.53	1.98
44	5 41 42.79	-1 54 37.74	14.08	11.87	10.45	9.52	2.21	1.42	0.93
45	5 41 31.73	-1 52 23.50	12.27	10.90	10.46	10.15	1.37	0.44	0.31
46	5 41 45.98	-1 55 03.22	15.23	12.53	10.46	8.68	2.70	2.07	1.78
47	5 41 31.44	-1 55 36.21	13.23	11.78	10.48	9.32	1.45	1.30	1.16
48	5 41 38.01	-1 53 59.21	13.46	11.51	10.50	9.83	1.95	1.01	0.67
49	5 41 50.27	-1 57 45.16	12.62	11.77	10.53	9.36	0.85	1.24	1.17
50	5 41 35.37	-1 52 31.27	13.09	11.57	10.54	9.06	1.52	1.03	1.48
51	5 41 31.62	-1 54 00.41	12.43	11.18	10.55	9.89	1.25	0.63	0.66
52	5 41 44.20	-1 55 22.09	14.26	12.28	10.60	9.04	1.98	1.68	1.56
53	5 42 01.81	-1 56 29.17	13.14	11.66	10.61	9.62	1.48	1.05	0.99
54	5 41 46.23	-1 50 12.26	12.51	11.38	10.65	9.51	1.13	0.73	1.14
55	5 42 05.88	-1 52 52.03	12.59	11.32	10.71	10.16	1.27	0.61	0.55
56	5 41 42.20	-1 55 11.78	12.67	11.41	10.71	10.02	1.26	0.70	0.69
57	5 41 42.45	-1 54 11.33	13.87	12.13	10.75	10.02	1.74	1.38	0.73
58	5 41 44.35	-1 54 21.73	14.58	12.50	10.77	9.60	2.08	1.73	1.17
59	5 41 44.63	-1 57 41.56	13.67	11.76	10.79	10.15	1.91	0.97	0.64
60	5 41 36.83	-1 52 35.65	12.95	11.58	10.81	10.39	1.37	0.77	0.42
61	5 41 42.61	-1 54 47.39	14.97	12.44	10.81	9.92	2.53	1.63	0.89
62	5 41 41.47	-1 54 41.12	15.83	12.96	10.82	9.12	2.87	2.14	1.70
63	5 41 36.41	-1 55 57.46	12.78	11.53	10.93	10.49	1.25	0.60	0.44
64	5 41 36.63	-1 54 10.67	13.33	11.76	10.95	10.37	1.57	0.81	0.58
65	5 41 40.06	-1 50 54.28	13.95	12.07	10.95	9.93	1.88	1.12	1.02
66	5 41 37.31	-1 52 46.91	13.19	11.75	10.96	10.09	1.44	0.79	0.87
67	5 41 45.53	-1 56 18.46	11.73	11.16	10.97	10.56	0.57	0.19	0.41
68	5 41 53.04	-1 56 35.35	13.52	11.88	10.99	10.36	1.64	0.89	0.63
69	5 41 41.28	-1 53 34.31	17.72	13.90	11.01	9.02	3.82	2.89	1.99
70	5 41 26.87	-1 54 55.73	12.44	11.51	11.02	10.35	0.93	0.49	0.67
71	5 41 38.42	-1 54 27.37	11.74	11.36	11.03	10.98	0.38	0.33	0.05
72	5 41 36.62	-1 52 45.42	12.77	11.62	11.04	10.95	1.15	0.58	0.09
73	5 41 38.15	-1 54 57.30	13.19	12.13	11.06	10.29	1.06	1.07	0.77
74	5 41 42.45	-1 55 04.42	15.64	13.19	11.06	8.96	2.45	2.13	2.10
75	5 41 31.81	-1 54 56.95	13.39	11.81	11.07	10.62	1.58	0.74	0.45
76	5 41 28.58	-1 50 05.66	13.05	11.68	11.08	10.34	1.37	0.60	0.74

Table A-1-continued

ID	RA (2000) ¹	Dec (2000) ¹	J	H	K	L	(J-H)	(H-K)	(K-L)
77	5 41 35.98	-1 57 14.45	15.27	12.62	11.08	10.20	2.65	1.54	0.88
78	5 41 40.14	-1 52 22.85	14.94	12.59	11.09	9.89	2.35	1.42	1.20
79	5 41 46.81	-1 49 27.32	13.16	11.80	11.10	9.88	1.36	0.70	1.22
80	5 41 41.63	-1 54 14.29	15.41	13.11	11.10	9.45	2.30	2.01	1.65
81	5 41 39.11	-1 56 28.86	14.43	12.55	11.11	9.97	1.88	1.44	1.14
82	5 41 39.42	-1 53 35.50	14.03	12.49	11.12	9.73	1.54	1.37	1.39
83	5 41 40.60	-1 55 20.71	15.00	12.78	11.14	9.73	2.22	1.64	1.41
84	5 41 38.22	-1 55 38.64	13.08	11.89	11.15	10.24	1.19	0.74	0.91
85	5 41 32.72	-1 52 16.04	13.74	12.29	11.17	10.42	1.45	1.12	0.75
86	5 41 42.50	-1 54 04.47	15.10	13.20	11.18	9.85	1.90	1.25	1.33
87	5 42 04.85	-1 57 36.31	13.77	11.91	11.18	10.44	1.86	0.73	0.74
88	5 41 35.87	-1 56 24.77	14.70	12.71	11.20	9.78	1.99	1.51	1.42
89	5 41 25.68	-1 55 50.37	13.87	12.26	11.20	9.89	1.61	1.06	1.31
90	5 41 55.85	-1 55 09.17	12.99	11.95	11.23	10.91	1.04	0.72	0.32
91	5 41 43.52	-1 56 44.42	15.31	12.60	11.23	10.48	2.71	1.37	0.75
92	5 41 43.43	-1 53 25.95	15.38	12.98	11.24	9.72	2.40	1.74	1.52
93	5 41 38.79	-1 56 04.87	14.34	12.35	11.25	10.22	1.99	1.10	1.03
94	5 41 33.72	-1 56 10.19	14.96	12.77	11.26	10.11	2.19	1.51	1.15
95	5 41 25.92	-1 57 32.62	13.61	12.10	11.26	10.65	1.51	0.84	0.61
96	5 41 33.90	-1 53 53.77	13.84	12.11	11.27	10.03	1.73	0.84	1.24
97	5 41 54.83	-1 57 26.71	12.88	11.73	11.28	10.75	1.15	0.45	0.53
98	5 41 50.15	-1 57 31.03	13.41	11.99	11.28	10.67	1.42	0.71	0.61
99	5 41 33.23	-1 51 30.24	13.50	11.99	11.29	10.90	1.51	0.70	0.39
100	5 41 42.59	-1 56 19.59	13.63	12.15	11.30	10.81	1.48	0.85	0.49
101	5 41 37.14	-1 51 42.81	15.74	12.92	11.35	9.95	2.82	1.57	1.40
102	5 41 50.85	-1 53 15.65	14.87	12.40	11.35	10.25	2.47	1.05	1.10
103	5 41 55.96	-1 50 49.60	14.11	12.50	11.41	9.89	1.61	1.09	1.52
104	5 41 28.29	-1 50 37.29	13.22	12.12	11.43	10.33	1.10	0.69	1.10
105	5 41 36.81	-1 54 50.42	13.75	12.41	11.44	10.70	1.34	0.97	0.74
106	5 41 49.33	-1 53 32.49	13.55	12.46	11.48	10.43	1.09	0.98	1.05
107	5 41 36.25	-1 53 41.61	14.14	12.35	11.48	10.54	1.79	0.87	0.94
108	5 41 51.61	-1 52 08.86	14.70	12.89	11.49	10.12	1.81	1.40	1.37
109	5 41 54.38	-1 55 56.84	13.19	12.15	11.49	11.05	1.04	0.66	0.44
110	5 41 29.16	-1 51 34.21	13.03	11.94	11.50	10.97	1.09	0.44	0.53
111	5 41 49.64	-1 53 27.42	13.57	12.49	11.50	10.51	1.08	0.99	0.99
112	5 41 47.52	-1 59 40.09	15.16	12.93	11.53	10.69	2.23	1.40	0.84
113	5 41 26.85	-1 54 12.96	13.48	12.39	11.53	10.36	1.09	0.86	1.17
114	5 41 24.87	-1 52 31.00	13.64	12.28	11.54	11.01	1.36	0.74	0.53
115	5 41 36.87	-1 53 41.51	14.82	12.75	11.57	10.41	2.07	1.18	1.16
116	5 41 48.61	-1 53 50.08	14.68	12.82	11.57	10.60	1.86	1.25	0.97
117	5 41 45.82	-1 53 46.18	14.74	12.98	11.58	10.35	1.76	1.40	1.23
118	5 41 44.13	-1 58 47.34	13.48	12.29	11.59	10.26	1.19	0.70	1.33
119	5 41 38.73	-1 57 32.03	13.59	12.32	11.61	10.79	1.27	0.71	0.82

Table A-1-continued

ID	RA (2000) ¹	Dec (2000) ¹	J	H	K	L	(J-H)	(H-K)	(K-L)
120	5 41 59.50	-1 59 10.42	12.94	12.13	11.62	10.91	0.81	0.51	0.71
121	5 41 49.90	-1 56 28.09	13.95	12.60	11.63	11.34	1.35	0.97	0.29
122	5 41 33.76	-1 53 11.19	13.46	12.41	11.65	10.61	1.05	0.76	1.04
123	5 41 55.02	-1 56 47.99	14.14	12.46	11.65	10.57	1.68	0.81	1.08
124	5 41 36.46	-1 53 21.08	14.08	12.66	11.69	10.95	1.42	0.97	0.74
125	5 41 41.62	-1 51 47.76	13.77	12.39	11.69	11.00	1.38	0.70	0.69
126	5 41 45.49	-1 51 24.35	14.72	12.73	11.71	10.61	1.99	1.02	1.10
127	5 41 43.53	-1 51 37.20	15.97	13.03	11.74	10.95	2.94	1.29	0.79
128	5 41 43.28	-1 53 31.12	15.37	13.72	11.74	10.87	1.65	1.98	0.87
129	5 41 56.79	-1 50 33.33	13.88	12.50	11.77	10.81	1.38	0.73	0.96
130	5 41 35.26	-1 52 14.05	14.82	13.29	11.82	9.93	1.53	1.47	1.89
131	5 41 53.02	-1 56 29.97	15.18	13.64	11.82	9.95	1.54	1.82	1.87
132	5 41 57.71	-1 51 28.07	13.55	12.36	11.85	11.31	1.19	0.51	0.54
133	5 41 38.27	-1 58 20.06	14.16	12.59	11.86	11.01	1.57	0.73	0.85
134	5 41 48.70	-1 54 16.52	15.39	13.35	11.87	10.14	2.04	1.48	1.73
135	5 41 47.39	-1 58 21.26	16.55	13.77	11.88	9.77	2.78	1.89	2.11
136	5 41 56.73	-1 55 52.50	13.26	12.38	11.89	11.44	0.88	0.49	0.45
137	5 41 38.86	-1 51 47.79	14.81	13.02	11.90	10.85	1.79	1.12	1.05
138	5 41 33.45	-1 55 16.69	14.10	12.64	11.94	11.13	1.46	0.70	0.81
139	5 41 49.10	-1 54 09.21	13.99	12.92	11.95	10.92	1.07	0.97	1.03
140	5 41 41.32	-1 53 53.84	16.64	13.88	11.96	10.26	2.76	1.92	1.70
141	5 41 49.75	-1 52 56.93	16.33	13.53	11.98	10.07	2.80	1.55	1.91
142	5 41 26.96	-1 52 13.94	13.78	12.58	12.01	11.29	1.20	0.57	0.72

¹Coordinates are approximate, and accurate to only a few arcseconds.

APPENDIX B
THE *JHK*L POSITIONS AND PHOTOMETRY FOR TRAPEZIUM

Table B-1: The *JHK*L Photometry of Trapezium Sources

ID	RA (2000)	Dec (2000)	J	H	K	L	(J-H)	(H-K)	(K-L)
1	5 35 16.47	-5 23 22.91	4.63	4.48	4.41	4.27	0.15	0.07	0.14
2	5 35 22.90	-5 24 57.72	5.01	4.97	4.89	4.79	0.04	0.08	0.10
3	5 35 15.83	-5 23 14.24	6.09	5.81	5.65	5.76	0.28	0.16	-0.11
4	5 35 17.26	-5 23 16.60	6.01	5.84	5.69	5.46	0.17	0.15	0.23
5	5 35 20.22	-5 20 57.02	8.02	6.86	5.91	4.95	1.16	0.95	0.96
6	5 35 26.40	-5 25 00.79	6.46	6.39	6.32	6.10	0.07	0.07	0.22
7	5 35 16.10	-5 23 06.96	6.88	6.55	6.43	5.44	0.33	0.12	0.99
8	5 35 15.78	-5 23 09.90	7.54	7.15	6.90	6.55	0.40	0.25	0.35
9	5 35 13.80	-5 21 59.63	12.20	9.26	7.10	4.49	2.94	2.16	2.61
10	5 35 15.96	-5 23 49.96	8.69	7.75	7.13	5.65	0.94	0.62	1.48
11	5 35 18.67	-5 20 33.74	8.60	7.73	7.37	6.85	0.87	0.36	0.52
12	5 35 20.72	-5 21 44.37	8.05	7.69	7.49	7.14	0.36	0.20	0.35
13	5 35 18.67	-5 23 13.93	10.83	9.09	7.51	5.77	1.74	1.59	1.73
14	5 35 17.96	-5 22 45.46	8.60	7.89	7.58	7.15	0.71	0.31	0.42
15	5 35 05.64	-5 25 19.55	8.89	8.07	7.59	6.23	0.82	0.48	1.37
16	5 35 18.21	-5 23 35.89	9.68	8.61	7.75	6.44	1.07	0.85	1.31
17	5 35 17.08	-5 23 34.05	9.35	8.42	7.84	6.50	0.93	0.58	1.34
18	5 35 10.74	-5 23 44.78	8.87	8.12	7.89	7.57	0.76	0.22	0.32
19	5 35 15.35	-5 22 15.57	10.17	9.11	8.05	6.78	1.06	1.06	1.27
20	5 35 15.64	-5 22 56.47	9.35	8.55	8.10	6.80	0.81	0.45	1.30
21	5 35 13.21	-5 24 55.51	10.32	9.16	8.14	7.06	1.16	1.01	1.08
22	5 35 17.22	-5 21 31.71	9.34	8.54	8.19	7.89	0.80	0.35	0.30
23	5 35 13.63	-5 19 54.88	11.05	9.40	8.32	6.61	1.65	1.08	1.71
24	5 35 15.82	-5 23 22.49	10.54	9.14	8.37	7.57	1.40	0.77	0.80
25	5 35 20.06	-5 21 05.94	10.30	9.25	8.37	7.32	1.05	0.88	1.05
26	5 35 16.71	-5 23 24.85	8.68	8.50	8.38	8.75	0.18	0.12	-0.37
27	5 35 21.05	-5 23 49.00	9.39	8.79	8.46	8.22	0.60	0.33	0.24
28	5 35 18.38	-5 22 37.42	9.53	8.80	8.55	8.13	0.73	0.25	0.42
29	5 35 16.38	-5 24 03.33	10.05	9.17	8.61	7.78	0.88	0.56	0.83
30	5 35 15.20	-5 22 54.36	10.70	9.24	8.62	7.37	1.46	0.62	1.25
31	5 35 14.92	-5 22 39.20	10.18	9.30	8.66	7.57	0.88	0.64	1.09
32	5 35 12.61	-5 23 44.21	9.84	9.09	8.67	7.78	0.75	0.42	0.89
33	5 35 18.04	-5 24 03.05	11.77	9.96	8.68	7.26	1.81	1.28	1.42

Table B-1-continued

ID	RA (2000)	Dec (2000)	J	H	K	L	(J-H)	(H-K)	(K-L)
34	5 35 14.36	-5 22 32.73	14.22	11.42	8.71	5.66	2.81	2.71	3.05
35	5 35 15.56	-5 25 14.19	9.99	9.15	8.73	8.39	0.84	0.42	0.34
36	5 35 25.06	-5 22 58.56	10.56	9.37	8.74	7.81	1.19	0.63	0.92
37	5 35 17.36	-5 22 35.70	10.87	9.74	8.77	7.49	1.13	0.97	1.28
38	5 35 16.01	-5 23 52.92	10.65	9.70	8.79	7.70	0.95	0.91	1.09
39	5 35 26.35	-5 25 40.19	9.57	9.02	8.81	8.19	0.55	0.22	0.62
40	5 35 10.22	-5 23 21.61	11.06	9.64	8.81	7.39	1.42	0.83	1.42
41	5 35 18.71	-5 22 56.81	10.70	9.57	8.83	7.56	1.13	0.74	1.27
42	5 35 11.49	-5 26 02.68	9.91	9.06	8.84	8.41	0.86	0.22	0.42
43	5 35 13.81	-5 22 07.07	10.67	9.75	8.86	8.07	0.92	0.88	0.80
44	5 35 16.75	-5 23 16.48	11.83	10.14	8.88	7.44	1.70	1.26	1.44
45	5 35 16.99	-5 21 45.35	9.20	9.04	8.89	8.68	0.16	0.15	0.21
46	5 35 16.77	-5 24 04.27	9.99	9.34	8.90	8.59	0.66	0.43	0.31
47	5 35 14.67	-5 20 42.43	11.37	9.82	9.00	7.98	1.55	0.82	1.02
48	5 35 15.27	-5 22 56.87	9.96	9.28	9.03	8.85	0.68	0.25	0.18
49	5 35 17.57	-5 22 56.78	10.53	9.56	9.05	8.00	0.96	0.51	1.05
50	5 35 11.98	-5 20 33.18	10.74	9.59	9.10	8.15	1.15	0.49	0.95
51	5 35 19.31	-5 20 07.85	10.84	9.73	9.10	8.47	1.12	0.63	0.63
52	5 35 14.28	-5 24 24.68	10.27	9.48	9.11	8.25	0.79	0.37	0.86
53	5 35 24.44	-5 24 39.81	10.76	9.77	9.11	7.71	0.98	0.67	1.40
54	5 35 06.28	-5 22 02.63	11.40	9.86	9.11	8.64	1.53	0.75	0.47
55	5 35 13.76	-5 22 22.01	11.39	10.28	9.12	7.24	1.11	1.16	1.88
56	5 35 14.67	-5 22 33.70	10.35	9.51	9.14	9.10	0.84	0.36	0.04
57	5 35 19.66	-5 24 26.63	11.00	9.98	9.16	7.99	1.02	0.83	1.17
58	5 35 28.21	-5 24 58.14	11.63	10.14	9.18	8.01	1.50	0.96	1.17
59	5 35 19.14	-5 20 38.75	9.98	9.55	9.23	8.86	0.42	0.33	0.37
60	5 35 16.99	-5 23 37.06	11.25	10.24	9.23	7.93	1.02	1.01	1.30
61	5 35 16.00	-5 21 09.85	10.95	9.72	9.25	8.84	1.24	0.47	0.41
62	5 35 14.11	-5 22 36.75	11.05	10.17	9.25	7.36	0.87	0.92	1.90
63	5 35 27.31	-5 23 36.60	11.62	10.30	9.25	8.08	1.32	1.06	1.16
64	5 35 22.19	-5 24 24.87	10.70	9.71	9.27	8.89	0.99	0.45	0.37
65	5 35 16.99	-5 23 00.97	10.74	9.84	9.27	8.45	0.91	0.57	0.82
66	5 35 20.46	-5 23 29.78	10.89	9.91	9.30	8.22	0.98	0.61	1.07
67	5 35 26.07	-5 21 21.04	11.34	9.94	9.31	8.72	1.40	0.63	0.59
68	5 35 14.41	-5 23 33.66	10.75	9.84	9.32	8.34	0.92	0.52	0.99
69	5 35 11.90	-5 21 03.38	12.19	10.44	9.36	7.99	1.75	1.08	1.36
70	5 35 23.81	-5 23 34.27	11.32	10.09	9.37	8.10	1.23	0.71	1.27
71	5 35 22.81	-5 23 13.46	11.95	10.61	9.38	8.02	1.35	1.22	1.36
72	5 35 21.81	-5 23 53.89	10.35	9.69	9.39	8.84	0.67	0.30	0.54
73	5 35 09.77	-5 23 26.99	10.36	9.64	9.40	9.09	0.72	0.23	0.32
74	5 35 14.96	-5 23 39.26	10.55	9.78	9.43	9.05	0.77	0.35	0.37
75	5 35 13.31	-5 20 18.95	11.93	10.69	9.45	8.13	1.25	1.24	1.31
76	5 35 04.47	-5 23 56.63	11.14	10.19	9.46	8.48	0.96	0.73	0.98

Table B-1-continued

ID	RA (2000)	Dec (2000)	J	H	K	L	(J-H)	(H-K)	(K-L)
77	5 35 13.45	-5 23 40.29	11.17	10.30	9.46	8.47	0.87	0.84	0.99
78	5 35 16.07	-5 20 36.31	11.04	10.04	9.48	8.56	1.01	0.56	0.92
79	5 35 09.78	-5 21 28.42	11.57	10.12	9.48	9.06	1.45	0.65	0.41
80	5 35 10.51	-5 22 45.70	10.66	9.82	9.49	9.34	0.85	0.32	0.15
81	5 35 16.90	-5 22 22.45	10.76	9.86	9.51	9.21	0.90	0.35	0.30
82	5 35 17.56	-5 21 45.58	11.13	9.99	9.52	7.80	1.14	0.47	1.72
83	5 35 20.63	-5 24 46.46	11.38	10.41	9.52	8.20	0.97	0.89	1.32
84	5 35 05.73	-5 24 18.54	11.82	10.50	9.54	8.13	1.32	0.96	1.41
85	5 35 17.47	-5 23 21.02	10.87	10.16	9.55	8.28	0.71	0.62	1.26
86	5 35 16.30	-5 23 16.52	11.36	10.40	9.55	8.16	0.97	0.85	1.39
87	5 35 13.98	-5 21 23.37	12.74	10.81	9.56	8.13	1.93	1.25	1.43
88	5 35 10.95	-5 24 48.72	11.33	10.21	9.57	8.16	1.12	0.63	1.42
89	5 35 11.81	-5 21 49.33	15.59	11.82	9.58	8.32	3.77	2.24	1.25
90	5 35 15.81	-5 23 26.40	11.70	10.82	9.59	8.53	0.88	1.24	1.06
91	5 35 12.29	-5 23 48.17	10.62	9.89	9.61	8.89	0.73	0.27	0.73
92	5 35 14.06	-5 23 38.48	10.76	9.92	9.64	9.06	0.84	0.29	0.58
93	5 35 17.85	-5 20 54.06	11.13	10.15	9.66	8.58	0.98	0.49	1.08
94	5 35 21.29	-5 24 57.40	10.66	9.93	9.68	9.32	0.73	0.25	0.36
95	5 35 11.21	-5 22 37.85	14.02	11.40	9.68	7.65	2.62	1.72	2.03
96	5 35 17.01	-5 22 33.00	10.72	9.96	9.69	9.26	0.76	0.27	0.43
97	5 35 17.82	-5 23 15.57	10.80	10.17	9.69	9.08	0.63	0.48	0.61
98	5 35 20.14	-5 21 33.65	11.03	10.06	9.72	9.18	0.97	0.34	0.54
99	5 35 11.98	-5 22 54.21	12.40	10.78	9.73	8.41	1.62	1.05	1.32
100	5 35 20.40	-5 22 13.64	11.21	10.10	9.74	9.36	1.11	0.36	0.37
101	5 35 24.70	-5 24 35.68	11.61	10.39	9.76	8.83	1.22	0.63	0.93
102	5 35 14.76	-5 20 28.97	12.78	10.94	9.76	8.40	1.85	1.18	1.36
103	5 35 26.01	-5 25 47.84	11.46	10.33	9.77	8.99	1.13	0.55	0.78
104	5 35 15.49	-5 22 48.56	11.32	10.34	9.77	8.97	0.98	0.56	0.80
105	5 35 15.88	-5 23 01.86	11.38	10.43	9.77	8.55	0.94	0.66	1.22
106	5 35 26.18	-5 20 06.07	11.94	10.60	9.77	8.77	1.34	0.83	1.00
107	5 35 15.69	-5 25 33.23	11.60	10.64	9.77	8.79	0.96	0.87	0.98
108	5 35 14.99	-5 21 59.95	10.86	10.09	9.78	9.40	0.78	0.31	0.38
109	5 35 10.59	-5 21 56.35	11.03	10.22	9.78	9.08	0.81	0.44	0.70
110	5 35 15.41	-5 21 13.98	12.38	10.98	9.83	8.32	1.40	1.15	1.51
111	5 35 15.45	-5 23 45.48	11.36	10.62	9.86	8.98	0.74	0.76	0.87
112	5 35 21.68	-5 21 47.19	12.13	10.83	9.86	8.45	1.29	0.97	1.40
113	5 35 12.83	-5 20 43.70	11.34	10.43	9.87	8.98	0.91	0.56	0.89
114	5 35 18.03	-5 22 05.35	12.00	10.57	9.87	9.08	1.43	0.70	0.79
115	5 35 15.62	-5 24 03.08	11.02	10.23	9.89	9.25	0.78	0.35	0.63
116	5 35 28.14	-5 23 06.41	12.52	10.95	9.92	8.98	1.57	1.04	0.94
117	5 35 14.37	-5 22 54.18	13.26	11.27	9.92	8.44	2.00	1.35	1.48
118	5 35 10.33	-5 21 13.16	11.69	10.55	9.93	8.99	1.14	0.62	0.94
119	5 35 24.26	-5 25 18.74	11.44	10.52	9.94	9.19	0.92	0.58	0.75

Table B-1-continued

ID	RA (2000)	Dec (2000)	J	H	K	L	(J-H)	(H-K)	(K-L)
120	5 35 25.09	-5 23 46.74	10.91	10.15	9.95	9.76	0.76	0.21	0.19
121	5 35 25.48	-5 21 35.07	11.71	10.60	9.95	9.80	1.10	0.66	0.15
122	5 35 15.95	-5 22 21.16	12.04	10.84	9.95	8.57	1.20	0.89	1.37
123	5 35 12.88	-5 21 33.94	15.34	11.92	9.95	8.26	3.41	1.98	1.68
124	5 35 18.96	-5 22 18.74	11.96	10.63	9.97	9.51	1.33	0.67	0.45
125	5 35 25.72	-5 23 39.37	11.89	10.73	9.98	8.59	1.16	0.75	1.39
126	5 35 21.16	-5 25 57.09	11.84	10.77	9.98	8.54	1.08	0.79	1.44
127	5 35 17.39	-5 24 00.23	13.02	11.10	9.98	8.59	1.93	1.12	1.39
128	5 35 20.05	-5 25 37.67	11.46	10.53	9.99	8.91	0.93	0.54	1.08
129	5 35 20.94	-5 21 50.88	11.74	10.70	10.01	9.01	1.05	0.68	1.01
130	5 35 20.77	-5 21 55.08	11.62	10.60	10.04	9.16	1.03	0.55	0.88
131	5 35 25.44	-5 21 51.53	11.62	10.64	10.05	9.27	0.98	0.59	0.78
132	5 35 14.06	-5 19 52.08	11.38	10.60	10.06	9.28	0.78	0.54	0.78
133	5 35 17.07	-5 23 39.77	11.73	10.71	10.06	9.33	1.02	0.65	0.73
134	5 35 05.37	-5 24 10.73	11.90	10.76	10.10	8.46	1.14	0.67	1.64
135	5 35 18.96	-5 21 07.78	11.67	10.60	10.12	9.25	1.07	0.48	0.87
136	5 35 17.56	-5 25 42.86	12.36	10.91	10.12	8.98	1.45	0.80	1.13
137	5 35 22.55	-5 23 43.71	11.49	10.60	10.13	9.53	0.89	0.47	0.60
138	5 35 14.95	-5 23 29.03	11.97	10.94	10.13	9.08	1.02	0.81	1.06
139	5 35 13.18	-5 22 21.27	12.50	11.31	10.14	8.96	1.19	1.17	1.18
140	5 35 22.45	-5 22 01.10	11.79	10.83	10.15	9.52	0.96	0.68	0.64
141	5 35 21.36	-5 23 45.51	11.65	10.75	10.16	9.18	0.90	0.59	0.98
142	5 35 22.27	-5 20 29.28	10.80	10.29	10.20	10.02	0.51	0.10	0.18
143	5 35 16.21	-5 24 56.34	12.02	10.96	10.21	8.93	1.06	0.75	1.29
144	5 35 10.62	-5 22 56.09	13.80	11.52	10.21	8.94	2.27	1.31	1.27
145	5 35 17.37	-5 25 44.79	11.40	10.59	10.22	9.91	0.81	0.37	0.31
146	5 35 18.24	-5 23 15.69	12.03	10.97	10.22	9.17	1.06	0.75	1.05
147	5 35 19.07	-5 23 49.63	12.17	11.22	10.22	7.87	0.94	1.00	2.36
148	5 35 22.33	-5 24 14.22	11.31	10.86	10.23	8.78	0.45	0.63	1.46
149	5 35 14.72	-5 21 06.33	13.40	11.36	10.24	8.86	2.04	1.13	1.37
150	5 35 19.40	-5 25 42.42	15.95	12.90	10.24	7.37	3.05	2.66	2.87
151	5 35 14.88	-5 23 05.10	12.81	11.17	10.26	8.91	1.65	0.91	1.34
152	5 35 16.28	-5 21 09.14	12.15	10.91	10.28	9.35	1.24	0.63	0.93
153	5 35 22.98	-5 22 41.67	12.36	11.02	10.28	9.68	1.35	0.74	0.59
154	5 35 23.34	-5 21 25.42	12.47	11.14	10.28	9.16	1.33	0.87	1.11
155	5 35 14.32	-5 23 08.33	12.88	11.19	10.28	8.71	1.69	0.91	1.57
156	5 35 12.28	-5 20 45.26	12.13	10.98	10.30	9.51	1.15	0.68	0.79
157	5 35 25.38	-5 24 11.40	12.59	11.13	10.30	9.02	1.46	0.83	1.28
158	5 35 18.86	-5 21 41.17	11.49	10.62	10.31	9.86	0.87	0.32	0.45
159	5 35 20.09	-5 20 43.92	12.84	11.37	10.32	9.20	1.47	1.05	1.12
160	5 35 24.34	-5 22 32.30	13.68	11.71	10.32	9.02	1.98	1.39	1.30
161	5 35 18.76	-5 22 02.14	11.86	10.76	10.33	9.89	1.09	0.44	0.44
162	5 35 18.48	-5 24 07.00	11.85	10.91	10.33	9.44	0.94	0.59	0.89

Table B-1-continued

ID	RA (2000)	Dec (2000)	J	H	K	L	(J-H)	(H-K)	(K-L)
163	5 35 20.18	-5 23 08.53	12.42	11.05	10.33	9.22	1.37	0.72	1.11
164	5 35 16.29	-5 22 10.45	12.65	11.36	10.34	8.56	1.29	1.02	1.77
165	5 35 15.85	-5 22 45.76	11.65	10.81	10.35	9.81	0.83	0.46	0.54
166	5 35 13.22	-5 20 52.80	12.67	11.24	10.38	9.31	1.43	0.86	1.07
167	5 35 28.38	-5 25 03.40	11.46	10.63	10.39	9.82	0.83	0.24	0.57
168	5 35 23.65	-5 23 31.93	11.83	10.83	10.40	9.79	1.00	0.43	0.61
169	5 35 09.35	-5 21 41.72	13.64	11.54	10.40	9.36	2.10	1.14	1.04
170	5 35 19.22	-5 22 50.68	11.97	10.88	10.41	9.86	1.09	0.46	0.55
171	5 35 17.23	-5 20 27.74	11.58	10.92	10.41	9.71	0.67	0.51	0.70
172	5 35 14.73	-5 23 22.90	12.27	11.22	10.41	9.30	1.05	0.81	1.11
173	5 35 13.73	-5 21 35.95	16.59	12.76	10.41	8.39	3.83	2.36	2.02
174	5 35 13.05	-5 20 30.31	12.21	10.94	10.42	10.03	1.27	0.52	0.39
175	5 35 19.83	-5 22 21.60	12.53	11.37	10.42	8.69	1.16	0.95	1.73
176	5 35 14.92	-5 24 12.42	11.82	10.90	10.43	10.45	0.92	0.47	-0.02
177	5 35 22.10	-5 24 32.83	11.93	11.06	10.44	9.32	0.88	0.62	1.11
178	5 35 21.23	-5 22 00.20	12.76	11.33	10.45	9.51	1.43	0.88	0.94
179	5 35 19.12	-5 23 27.07	11.89	11.05	10.47	9.49	0.84	0.58	0.98
180	5 35 17.57	-5 23 24.74	13.07	11.55	10.47	8.93	1.52	1.08	1.54
181	5 35 14.71	-5 22 49.39	14.56	12.11	10.49	9.14	2.45	1.62	1.35
182	5 35 16.37	-5 25 09.73	11.94	11.00	10.50	9.49	0.94	0.50	1.01
183	5 35 20.53	-5 20 52.15	12.65	11.40	10.50	9.33	1.26	0.90	1.16
184	5 35 06.52	-5 24 41.45	11.45	10.72	10.51	10.28	0.73	0.21	0.24
185	5 35 16.35	-5 22 48.97	12.20	11.12	10.51	9.65	1.08	0.61	0.86
186	5 35 18.40	-5 20 20.33	12.71	11.21	10.52	9.88	1.50	0.69	0.64
187	5 35 25.08	-5 23 53.77	11.86	10.95	10.54	9.45	0.91	0.41	1.09
188	5 35 23.19	-5 22 28.37	13.76	11.87	10.54	9.25	1.89	1.33	1.29
189	5 35 21.66	-5 25 26.59	11.69	10.83	10.56	10.05	0.86	0.27	0.51
190	5 35 20.68	-5 23 53.22	11.70	11.04	10.56	10.11	0.67	0.48	0.45
191	5 35 14.23	-5 20 04.33	12.83	11.53	10.56	9.51	1.29	0.97	1.05
192	5 35 09.69	-5 23 56.01	13.66	11.59	10.56	9.70	2.07	1.03	0.87
193	5 35 11.66	-5 26 09.06	13.51	11.63	10.56	9.15	1.88	1.07	1.41
194	5 35 08.74	-5 22 56.74	12.48	11.16	10.57	10.09	1.32	0.59	0.47
195	5 35 21.80	-5 23 10.70	12.15	11.08	10.59	10.02	1.07	0.49	0.57
196	5 35 07.74	-5 21 01.63	13.98	11.92	10.60	8.79	2.06	1.32	1.81
197	5 35 29.35	-5 25 46.29	11.76	10.92	10.64	10.13	0.84	0.28	0.50
198	5 35 16.59	-5 24 06.04	11.88	11.06	10.64	10.18	0.82	0.42	0.46
199	5 35 13.05	-5 22 15.23	12.26	11.32	10.66	9.99	0.94	0.66	0.68
200	5 35 12.58	-5 23 02.03	13.58	11.70	10.66	9.45	1.88	1.04	1.21
201	5 35 16.09	-5 22 54.22	14.09	12.53	10.66	7.74	1.57	1.87	2.91
202	5 35 20.57	-5 20 43.22	12.45	11.29	10.67	9.82	1.16	0.62	0.84
203	5 35 21.56	-5 21 05.62	13.11	11.77	10.67	9.40	1.35	1.10	1.27
204	5 35 18.08	-5 24 01.01	12.01	11.29	10.69	9.75	0.72	0.59	0.94
205	5 35 05.69	-5 25 06.45	11.65	10.83	10.70	10.32	0.82	0.13	0.38

Table B-1-continued

ID	RA (2000)	Dec (2000)	J	H	K	L	(J-H)	(H-K)	(K-L)
206	5 35 16.49	-5 22 35.11	12.03	11.21	10.71	9.84	0.83	0.50	0.87
207	5 35 23.60	-5 25 26.48	12.83	11.60	10.72	9.35	1.23	0.88	1.37
208	5 35 15.17	-5 23 46.59	12.02	11.30	10.73	10.09	0.72	0.57	0.63
209	5 35 05.14	-5 20 24.55	12.38	11.32	10.74	9.68	1.06	0.58	1.06
210	5 35 18.88	-5 23 28.84	12.39	11.50	10.74	9.86	0.90	0.75	0.88
211	5 35 21.51	-5 23 16.70	12.33	11.28	10.75	10.25	1.05	0.53	0.50
212	5 35 10.91	-5 22 46.46	13.14	11.77	10.75	9.18	1.37	1.01	1.58
213	5 35 23.50	-5 20 01.72	14.29	12.05	10.77	9.66	2.24	1.29	1.11
214	5 35 15.27	-5 21 55.72	13.68	11.88	10.79	9.46	1.80	1.10	1.33
215	5 35 17.87	-5 23 03.12	12.46	11.52	10.83	9.77	0.94	0.69	1.06
216	5 35 24.66	-5 22 42.59	13.14	11.61	10.83	10.10	1.54	0.78	0.72
217	5 35 17.76	-5 22 30.93	13.89	12.10	10.83	9.99	1.79	1.27	0.84
218	5 35 20.85	-5 21 21.54	12.62	11.56	10.85	9.54	1.06	0.72	1.31
219	5 35 10.54	-5 22 16.69	13.15	11.62	10.87	10.43	1.53	0.75	0.44
220	5 35 20.55	-5 24 20.92	12.76	11.80	10.88	10.13	0.96	0.92	0.75
221	5 35 09.93	-5 21 43.46	14.11	12.00	10.88	9.69	2.11	1.11	1.19
222	5 35 24.63	-5 21 04.32	16.45	12.99	10.88	8.89	3.46	2.12	1.99
223	5 35 04.49	-5 26 04.11	12.14	11.25	10.89	10.09	0.89	0.37	0.80
224	5 35 21.78	-5 23 39.29	12.55	11.45	10.89	9.79	1.10	0.56	1.11
225	5 35 24.10	-5 21 32.70	12.32	11.48	10.89	10.08	0.84	0.59	0.82
226	5 35 29.58	-5 24 56.86	11.90	11.09	10.90	10.54	0.81	0.19	0.36
227	5 35 23.66	-5 23 46.32	12.26	11.35	10.91	10.18	0.91	0.43	0.73
228	5 35 14.68	-5 23 01.88	12.70	11.46	10.91	10.20	1.24	0.55	0.71
229	5 35 24.97	-5 24 01.46	12.84	11.59	10.92	10.07	1.26	0.67	0.85
230	5 35 18.95	-5 20 52.20	12.85	11.68	10.92	9.69	1.17	0.76	1.22
231	5 35 11.04	-5 22 46.73	13.74	11.92	10.93	9.60	1.82	0.99	1.33
232	5 35 20.85	-5 21 30.09	12.26	11.30	10.94	10.29	0.96	0.35	0.65
233	5 35 13.44	-5 21 07.36	13.63	11.96	10.95	10.33	1.67	1.01	0.63
234	5 35 08.54	-5 25 18.07	12.18	11.27	10.96	10.26	0.91	0.31	0.70
235	5 35 12.20	-5 24 56.44	16.70	12.79	10.96	9.03	3.91	1.83	1.92
236	5 35 22.13	-5 22 34.14	12.98	11.60	10.97	10.01	1.37	0.63	0.96
237	5 35 23.72	-5 23 19.96	13.32	11.92	10.98	9.92	1.41	0.94	1.06
238	5 35 10.15	-5 22 32.74	12.20	11.35	10.99	10.30	0.85	0.36	0.69
239	5 35 18.52	-5 20 42.75	12.67	11.55	11.00	10.19	1.12	0.55	0.81
240	5 35 17.95	-5 25 21.21	12.47	11.58	11.00	10.08	0.89	0.58	0.92
241	5 35 21.25	-5 22 59.53	12.72	11.54	11.01	10.40	1.18	0.53	0.61
242	5 35 18.85	-5 22 23.00	13.36	11.80	11.01	9.45	1.55	0.79	1.57
243	5 35 26.16	-5 22 57.02	13.14	11.70	11.03	10.30	1.43	0.67	0.73
244	5 35 10.55	-5 24 16.69	13.12	11.73	11.04	9.88	1.39	0.68	1.16
245	5 35 17.62	-5 21 53.86	13.67	12.00	11.04	9.71	1.67	0.96	1.33
246	5 35 19.61	-5 20 01.77	15.44	12.72	11.04	9.01	2.72	1.68	2.04
247	5 35 15.39	-5 23 33.45	12.09	11.39	11.05	10.30	0.70	0.34	0.75
248	5 35 18.37	-5 20 16.45	12.63	11.53	11.05	10.50	1.10	0.48	0.55

Table B-1-continued

ID	RA (2000)	Dec (2000)	J	H	K	L	(J-H)	(H-K)	(K-L)
249	5 35 17.78	-5 23 43.85	12.74	11.82	11.05	10.39	0.92	0.77	0.66
250	5 35 05.70	-5 25 04.26	12.01	11.38	11.06	10.72	0.63	0.33	0.34
251	5 35 13.54	-5 23 30.89	12.08	11.39	11.06	10.82	0.69	0.33	0.24
252	5 35 17.13	-5 22 50.10	12.27	11.40	11.07	11.60	0.87	0.33	-0.53
253	5 35 07.28	-5 22 26.66	12.22	11.49	11.08	10.33	0.73	0.41	0.75
254	5 35 17.96	-5 25 34.00	12.26	11.50	11.08	10.33	0.77	0.41	0.75
255	5 35 22.41	-5 25 09.48	12.22	11.37	11.10	11.25	0.85	0.27	-0.15
256	5 35 18.37	-5 24 26.84	12.56	11.74	11.10	10.37	0.82	0.64	0.73
257	5 35 14.07	-5 25 20.49	12.79	11.82	11.10	10.02	0.97	0.72	1.08
258	5 35 19.84	-5 24 47.96	12.51	11.66	11.11	10.20	0.86	0.55	0.91
259	5 35 14.47	-5 25 02.16	12.23	11.46	11.12	10.97	0.77	0.34	0.16
260	5 35 17.37	-5 20 14.84	12.56	11.56	11.12	10.80	0.99	0.45	0.32
261	5 35 14.88	-5 22 31.66	12.37	11.59	11.14	8.86	0.78	0.45	2.28
262	5 35 10.43	-5 19 52.30	12.73	11.63	11.15	10.52	1.10	0.48	0.64
263	5 35 06.18	-5 22 12.57	13.16	11.78	11.15	10.92	1.38	0.63	0.23
264	5 35 05.71	-5 23 54.17	12.09	11.46	11.18	10.90	0.63	0.27	0.29
265	5 35 16.96	-5 25 47.10	12.38	11.61	11.18	10.53	0.77	0.43	0.65
266	5 35 16.11	-5 24 11.42	12.33	11.65	11.18	10.59	0.69	0.46	0.59
267	5 35 16.19	-5 22 37.28	12.59	11.78	11.18	9.35	0.81	0.60	1.83
268	5 35 15.67	-5 25 10.49	12.85	11.92	11.18	10.41	0.93	0.74	0.77
269	5 35 23.68	-5 24 57.36	12.54	11.43	11.19	10.87	1.11	0.24	0.32
270	5 35 16.82	-5 24 32.11	14.19	12.54	11.19	9.75	1.66	1.35	1.44
271	5 35 10.60	-5 22 44.70	12.47	11.56	11.20	9.61	0.91	0.36	1.59
272	5 35 14.05	-5 25 50.17	12.49	11.65	11.22	10.48	0.83	0.44	0.74
273	5 35 13.07	-5 21 53.32	13.80	12.24	11.22	9.95	1.56	1.02	1.28
274	5 35 16.20	-5 21 32.38	12.70	11.79	11.23	10.19	0.91	0.55	1.04
275	5 35 04.61	-5 24 42.57	12.62	11.63	11.24	10.84	0.99	0.38	0.40
276	5 35 17.13	-5 24 58.67	12.35	11.64	11.24	11.03	0.72	0.40	0.20
277	5 35 20.09	-5 19 59.02	14.00	12.21	11.24	9.95	1.79	0.97	1.30
278	5 35 16.29	-5 22 25.11	13.49	12.81	11.24	9.46	0.67	1.58	1.77
279	5 35 13.62	-5 24 25.74	12.33	11.55	11.25	11.35	0.78	0.29	-0.09
280	5 35 18.88	-5 20 30.98	13.01	11.93	11.26	9.68	1.08	0.67	1.58
281	5 35 21.86	-5 22 08.31	12.59	11.62	11.27	11.24	0.97	0.35	0.03
282	5 35 11.00	-5 22 24.83	13.17	11.94	11.27	10.54	1.23	0.67	0.73
283	5 35 20.27	-5 25 04.06	14.10	12.58	11.29	9.24	1.51	1.29	2.06
284	5 35 17.70	-5 24 54.12	12.43	11.74	11.30	10.98	0.69	0.44	0.31
285	5 35 15.88	-5 22 32.81	13.46	12.38	11.30	9.71	1.08	1.08	1.59
286	5 35 13.55	-5 23 59.68	15.13	12.93	11.30	9.65	2.21	1.62	1.66
287	5 35 20.64	-5 22 45.52	13.37	12.16	11.31	10.11	1.21	0.86	1.19
288	5 35 11.66	-5 24 21.48	12.62	11.82	11.32	10.27	0.80	0.50	1.05
289	5 35 24.52	-5 25 01.55	13.21	11.87	11.32	10.70	1.34	0.55	0.62
290	5 35 15.53	-5 23 37.44	12.73	12.07	11.32	9.22	0.66	0.75	2.11
291	5 35 05.43	-5 25 22.57	13.08	12.37	11.32	11.56	0.70	1.06	-0.24

Table B-1-continued

ID	RA (2000)	Dec (2000)	J	H	K	L	(J-H)	(H-K)	(K-L)
292	5 35 25.43	-5 23 33.31	12.99	11.91	11.33	10.27	1.09	0.58	1.06
293	5 35 15.22	-5 23 18.67	13.46	12.28	11.33	10.22	1.18	0.95	1.10
294	5 35 08.55	-5 24 39.58	15.03	11.65	11.34	10.34	3.38	0.31	1.00
295	5 35 16.74	-5 20 20.01	13.45	12.16	11.34	9.94	1.29	0.82	1.40
296	5 35 11.73	-5 23 40.45	12.34	11.71	11.35	11.51	0.64	0.35	-0.16
297	5 35 23.89	-5 21 18.66	13.89	12.34	11.35	10.05	1.55	0.99	1.30
298	5 35 04.87	-5 20 57.56	13.38	12.09	11.36	10.93	1.30	0.72	0.44
299	5 35 25.13	-5 22 25.13	13.23	12.06	11.37	10.45	1.17	0.69	0.92
300	5 35 24.03	-5 23 13.91	14.22	12.40	11.39	10.35	1.82	1.01	1.04
301	5 35 21.89	-5 23 55.63	12.89	11.92	11.40	10.81	0.96	0.52	0.59
302	5 35 19.62	-5 23 57.29	12.59	11.82	11.41	11.19	0.77	0.41	0.22
303	5 35 05.41	-5 24 15.15	13.29	12.06	11.41	10.26	1.23	0.65	1.15
304	5 35 21.04	-5 22 25.26	13.27	12.19	11.41	10.33	1.07	0.78	1.09
305	5 35 06.15	-5 19 55.57	12.84	11.85	11.42	10.76	1.00	0.43	0.66
306	5 35 20.72	-5 22 31.49	13.31	12.12	11.44	10.57	1.19	0.68	0.87
307	5 35 17.66	-5 22 51.64	13.60	12.59	11.44	10.40	1.01	1.14	1.04
308	5 35 21.33	-5 24 11.50	12.60	11.70	11.45	10.76	0.89	0.25	0.70
309	5 35 16.59	-5 25 17.79	12.82	11.96	11.45	10.59	0.86	0.51	0.86
310	5 35 04.95	-5 21 09.33	13.71	12.13	11.45	10.83	1.58	0.68	0.62
311	5 35 12.40	-5 20 48.00	13.62	12.40	11.45	10.63	1.22	0.95	0.82
312	5 35 19.14	-5 20 35.94	13.67	12.27	11.46	10.47	1.40	0.82	0.98
313	5 35 16.39	-5 24 37.13	14.52	12.77	11.47	9.62	1.75	1.30	1.84
314	5 35 10.31	-5 19 56.30	12.90	11.90	11.48	10.39	1.00	0.42	1.08
315	5 35 11.79	-5 21 55.67	12.64	11.94	11.48	10.82	0.69	0.46	0.66
316	5 35 16.74	-5 22 31.13	12.86	12.11	11.48	10.88	0.76	0.62	0.60
317	5 35 17.93	-5 20 55.49	13.68	12.52	11.48	9.71	1.16	1.04	1.77
318	5 35 18.90	-5 24 17.47	12.96	12.14	11.49	10.70	0.83	0.65	0.79
319	5 35 13.89	-5 24 26.08	14.52	14.30	11.49	9.37	0.22	2.81	2.11
320	5 35 15.76	-5 21 39.85	12.76	11.87	11.50	11.09	0.89	0.37	0.41
321	5 35 20.06	-5 25 14.29	13.73	12.25	11.50	10.67	1.49	0.74	0.83
322	5 35 29.65	-5 20 02.23	14.60	12.52	11.50	10.58	2.08	1.02	0.92
323	5 35 09.70	-5 21 25.03	12.64	11.89	11.51	11.06	0.75	0.38	0.45
324	5 35 10.26	-5 23 16.26	14.34	12.52	11.52	10.13	1.81	1.01	1.39
325	5 35 16.01	-5 21 47.05	12.63	11.84	11.54	11.08	0.79	0.30	0.46
326	5 35 12.78	-5 20 35.02	13.37	12.16	11.54	10.68	1.21	0.62	0.86
327	5 35 19.55	-5 21 49.14	16.08	13.56	11.54	9.69	2.52	2.02	1.85
328	5 35 14.84	-5 23 46.38	12.63	11.92	11.55	10.57	0.71	0.37	0.99
329	5 35 14.35	-5 25 15.72	12.85	12.00	11.55	10.75	0.84	0.45	0.80
330	5 35 21.85	-5 23 06.60	13.84	12.49	11.55	10.17	1.35	0.94	1.38
331	5 35 17.82	-5 24 30.62	12.71	12.14	11.56	11.15	0.57	0.57	0.42
332	5 35 18.31	-5 24 38.90	13.19	12.23	11.56	10.65	0.96	0.67	0.91
333	5 35 11.64	-5 22 51.63	12.77	12.11	11.57	10.77	0.65	0.54	0.81
334	5 35 15.79	-5 24 24.69	12.84	12.11	11.58	10.93	0.73	0.53	0.65

Table B-1-continued

ID	RA (2000)	Dec (2000)	J	H	K	L	(J-H)	(H-K)	(K-L)
335	5 35 04.56	-5 20 14.03	16.74	13.53	11.60	10.65	3.21	1.93	0.94
336	5 35 26.41	-5 23 02.30	13.62	12.22	11.60	10.77	1.40	0.62	0.83
337	5 35 04.81	-5 22 38.81	12.85	12.00	11.61	11.03	0.85	0.39	0.58
338	5 35 22.47	-5 25 45.20	12.84	12.23	11.61	10.46	0.61	0.61	1.16
339	5 35 27.77	-5 21 18.87	16.48	13.44	11.61	9.65	3.04	1.83	1.96
340	5 35 15.88	-5 20 40.50	12.70	11.96	11.63	10.97	0.74	0.33	0.66
341	5 35 19.93	-5 24 02.62	12.85	12.13	11.63	11.00	0.72	0.50	0.63
342	5 35 24.47	-5 24 01.02	13.31	12.23	11.63	10.78	1.08	0.61	0.84
343	5 35 11.78	-5 21 32.83	15.70	13.33	11.63	10.11	2.37	1.70	1.52
344	5 35 18.28	-5 23 07.48	12.95	12.24	11.65	11.25	0.71	0.58	0.40
345	5 35 15.32	-5 23 23.30	13.15	12.72	11.65	11.19	0.43	1.07	0.46
346	5 35 08.30	-5 24 34.93	12.77	12.05	11.67	11.37	0.71	0.38	0.30
347	5 35 22.84	-5 25 47.67	12.84	12.08	11.67	10.84	0.75	0.41	0.83
348	5 35 24.89	-5 25 10.20	12.83	12.06	11.68	10.75	0.77	0.37	0.93
349	5 35 16.94	-5 20 59.88	12.95	12.15	11.68	10.63	0.81	0.47	1.04
350	5 35 23.98	-5 25 09.90	13.26	12.18	11.68	10.79	1.08	0.50	0.89
351	5 35 23.81	-5 24 16.76	13.32	12.19	11.69	11.03	1.13	0.50	0.67
352	5 35 17.48	-5 24 17.40	13.08	12.29	11.69	10.88	0.79	0.60	0.81
353	5 35 07.65	-5 24 00.82	12.88	12.05	11.70	11.24	0.83	0.35	0.46
354	5 35 07.52	-5 19 50.18	14.61	12.60	11.71	10.61	2.01	0.89	1.10
355	5 35 26.49	-5 23 45.01	13.92	12.41	11.71	11.09	1.51	0.70	0.62
356	5 35 23.22	-5 21 35.81	13.10	12.17	11.75	11.14	0.94	0.42	0.60
357	5 35 25.35	-5 25 29.57	12.91	12.15	11.76	10.84	0.77	0.38	0.92
358	5 35 16.32	-5 20 25.27	13.01	12.18	11.76	11.10	0.83	0.42	0.67
359	5 35 20.92	-5 23 21.87	13.17	12.30	11.77	11.04	0.87	0.53	0.73
360	5 35 14.15	-5 23 01.00	13.11	12.76	11.77	9.58	0.36	0.99	2.19
361	5 35 11.56	-5 24 48.14	15.56	13.07	11.77	10.79	2.49	1.30	0.98
362	5 35 08.24	-5 24 03.35	13.18	12.22	11.79	11.44	0.97	0.43	0.35
363	5 35 17.70	-5 23 41.19	13.12	12.46	11.80	10.53	0.66	0.65	1.27
364	5 35 16.98	-5 22 48.44	12.92	12.38	11.81	10.92	0.53	0.57	0.89
365	5 35 17.02	-5 20 12.04	13.67	12.50	11.81	11.23	1.17	0.69	0.58
366	5 35 10.47	-5 26 00.60	13.01	12.25	11.82	11.05	0.76	0.43	0.77
367	5 35 07.40	-5 25 48.19	12.93	12.30	11.84	11.00	0.63	0.45	0.84
368	5 35 10.84	-5 25 57.14	13.42	12.51	11.84	10.80	0.90	0.68	1.04
369	5 35 15.90	-5 23 38.12	13.58	12.55	11.84	10.79	1.03	0.71	1.04
370	5 35 17.49	-5 22 51.26	13.51	12.69	11.84	10.67	0.81	0.85	1.17
371	5 35 16.12	-5 22 12.50	13.09	12.16	11.86	11.24	0.94	0.30	0.62
372	5 35 26.97	-5 24 00.56	12.97	12.16	11.86	11.22	0.81	0.30	0.64
373	5 35 18.68	-5 23 56.42	13.06	12.40	11.86	11.06	0.66	0.54	0.79
374	5 35 28.16	-5 21 34.74	14.87	13.00	11.86	10.51	1.88	1.14	1.35
375	5 35 18.50	-5 23 29.24	13.30	12.43	11.87	10.99	0.87	0.55	0.88
376	5 35 17.40	-5 24 13.90	13.28	12.46	11.88	10.88	0.82	0.58	1.00
377	5 35 21.02	-5 23 55.68	13.17	12.47	11.89	11.52	0.70	0.58	0.37

Table B-1- continued

ID	RA (2000)	Dec (2000)	J	H	K	L	(J-H)	(H-K)	(K-L)
378	5 35 23.69	-5 22 12.71	13.82	12.68	11.90	10.91	1.13	0.79	0.99
379	5 35 19.51	-5 21 04.57	13.21	12.36	11.91	11.44	0.86	0.45	0.47
380	5 35 10.27	-5 21 57.21	13.49	12.53	11.93	11.50	0.96	0.60	0.42
381	5 35 13.37	-5 23 53.28	13.63	12.66	11.93	10.81	0.97	0.73	1.12
382	5 35 16.19	-5 21 10.75	13.35	12.68	11.93	11.23	0.67	0.75	0.70
383	5 35 17.67	-5 25 10.71	13.85	12.81	11.93	10.79	1.03	0.89	1.13
384	5 35 19.03	-5 25 02.95	13.12	12.41	11.94	11.50	0.71	0.47	0.44
385	5 35 22.85	-5 22 27.04	14.08	12.67	11.94	11.51	1.41	0.74	0.43
386	5 35 10.20	-5 20 21.11	13.41	12.47	11.95	10.99	0.93	0.52	0.96
387	5 35 20.16	-5 22 28.31	13.60	12.64	11.95	10.83	0.96	0.69	1.12
388	5 35 20.52	-5 23 23.03	14.33	12.99	11.95	10.73	1.34	1.05	1.21
389	5 35 06.55	-5 25 01.58	13.01	12.26	11.96	11.23	0.75	0.30	0.73
390	5 35 21.83	-5 22 40.31	13.49	12.61	11.96	11.40	0.87	0.65	0.56
391	5 35 18.38	-5 21 44.14	13.67	12.79	11.98	10.94	0.88	0.81	1.04

APPENDIX C
THE *JHK*L POSITIONS AND PHOTOMETRY FOR NGC 2071

Table C-1: The *JHK*L Photometry of NGC 2071 Sources

ID	RA (2000) ¹	Dec (2000) ¹	J	H	K	L	(J-H)	(H-K)	(K-L)
1	5 47 07.62	0 17 41.69	7.23	7.19	6.39	6.19	0.04	0.80	0.20
2	5 47 07.16	0 19 32.97	10.27	9.13	8.44	7.23	1.14	0.69	1.21
3	5 47 10.90	0 19 16.08	10.92	9.83	9.12	8.06	1.09	0.71	1.06
4	5 47 27.61	0 20 39.12	14.75	11.79	9.39	8.15	2.96	2.40	1.24
5	5 46 57.32	0 20 09.62	9.46	9.39	9.41	9.31	0.07	-0.02	0.10
6	5 47 05.04	0 23 11.27	13.40	11.13	9.43	7.90	2.27	1.70	1.53
7	5 46 45.78	0 17 00.71	11.16	10.14	9.51	8.60	1.02	0.63	0.91
8	5 47 35.01	0 21 33.77	14.09	11.63	10.00	9.69	2.46	1.63	0.31
9	5 47 04.92	0 18 33.65	11.51	10.50	10.02	9.95	1.01	0.48	0.07
10	5 47 05.22	0 21 51.22	14.48	12.41	10.15	7.77	2.07	2.26	2.38
11	5 46 44.02	0 18 01.24	11.58	10.68	10.16	9.55	0.90	0.52	0.61
12	5 47 01.63	0 18 46.10	13.88	11.49	10.18	9.30	2.39	1.31	0.88
13	5 47 05.53	0 22 11.56	13.88	11.75	10.21	8.69	2.13	1.54	1.52
14	5 47 04.57	0 21 43.55	16.64	13.11	10.33	7.92	3.53	2.78	2.41
15	5 47 03.05	0 23 24.13	12.82	11.26	10.43	9.66	1.56	0.83	0.77
16	5 47 25.00	0 18 52.80	13.35	12.30	10.48	11.50	1.05	1.82	-1.02
17	5 47 06.02	0 20 33.09	13.02	11.46	10.54	9.73	1.56	0.92	0.81
18	5 47 15.46	0 18 48.57	16.24	12.85	10.54	8.52	3.39	2.31	2.02
19	5 47 12.01	0 17 58.37	12.16	11.06	10.57	10.05	1.10	0.49	0.52
20	5 47 11.39	0 18 02.94	12.16	11.08	10.59	10.12	1.08	0.49	0.47
21	5 47 10.46	0 21 15.84	14.24	12.25	10.61	7.70	1.99	1.64	2.91
22	5 46 56.38	0 20 52.38	11.96	11.01	10.62	10.16	0.95	0.39	0.46
23	5 47 26.25	0 18 52.08	12.62	11.67	10.67	10.40	0.95	1.00	0.27
24	5 47 04.54	0 15 47.61	13.26	11.57	10.67	9.61	1.69	0.90	1.06
25	5 47 10.37	0 18 46.19	12.75	11.46	10.70	9.74	1.29	0.76	0.96
26	5 46 52.26	0 20 00.46	12.56	11.51	10.74	10.12	1.05	0.77	0.62
27	5 47 12.74	0 22 08.44	14.05	12.04	10.80	9.44	2.01	1.24	1.36
28	5 47 08.59	0 17 13.54	14.08	12.11	10.83	9.72	1.97	1.28	1.11
29	5 47 03.48	0 23 30.23	13.68	11.97	10.84	9.32	1.71	1.13	1.52
30	5 47 04.97	0 22 02.53	15.10	12.58	10.87	8.92	2.52	1.71	1.95
31	5 47 12.74	0 19 16.21	12.97	11.65	11.01	10.53	1.32	0.64	0.48
32	5 47 17.10	0 18 27.83	12.92	11.80	11.03	9.81	1.12	0.77	1.22
33	5 47 26.93	0 19 29.95	15.24	12.96	11.07	10.62	2.28	1.89	0.45

Table C-1—continued

ID	RA (2000)	Dec (2000)	J	H	K	L	(J-H)	(H-K)	(K-L)
34	5 47 06.63	0 19 23.30	13.04	11.80	11.10	10.40	1.24	0.70	0.70
35	5 47 07.78	0 20 25.47	13.02	11.76	11.19	10.35	1.26	0.57	0.84
36	5 47 01.97	0 23 56.51	15.09	12.56	11.19	10.46	2.53	1.37	0.73
37	5 47 04.63	0 19 19.72	13.60	12.23	11.19	9.83	1.37	1.04	1.36
38	5 46 43.93	0 15 30.64	12.79	11.86	11.33	10.20	0.93	0.53	1.13
39	5 46 54.81	0 19 54.64	13.90	12.33	11.43	10.67	1.57	0.90	0.76
40	5 47 06.25	0 17 28.01	12.84	11.97	11.49	11.15	0.87	0.48	0.34
41	5 47 32.61	0 18 17.99	15.78	13.02	11.52	10.62	2.76	1.50	0.90
42	5 47 03.07	0 19 24.53	13.02	12.05	11.54	10.41	0.97	0.51	1.13
43	5 46 44.81	0 16 57.82	13.18	12.13	11.60	11.30	1.05	0.53	0.30
44	5 46 54.27	0 21 13.50	13.55	12.43	11.63	10.53	1.12	0.80	1.11
45	5 47 04.09	0 23 20.88	14.77	12.92	11.68	10.45	1.85	1.24	1.23
46	5 46 51.74	0 19 38.09	13.15	12.21	11.74	11.47	0.94	0.47	0.27
47	5 47 08.53	0 19 24.81	13.69	12.09	11.81	10.79	1.60	0.28	1.02
48	5 47 09.54	0 22 37.77	17.70	14.44	11.94	10.60	3.26	2.50	1.34
49	5 47 19.98	0 16 15.61	13.59	12.53	11.96	11.23	1.06	0.57	0.73
50	5 47 12.28	0 22 17.23	15.28	13.19	11.97	10.93	2.09	1.22	1.04
51	5 46 51.37	0 19 20.65	13.66	12.57	11.97	10.88	1.09	0.60	1.09
52	5 46 59.90	0 18 18.99	13.57	12.53	12.03	11.51	1.04	0.50	0.52
53	5 47 10.14	0 18 05.18	14.20	13.02	12.04	11.43	1.18	0.98	0.61

¹Coordinates are approximate, and accurate to only a few arcseconds.

APPENDIX D
THE *JHK*L POSITIONS AND PHOTOMETRY FOR NGC 2068

Table D-1: The *JHK*L Photometry of NGC 2068 Sources

ID	RA (2000) ¹	Dec (2000) ¹	J	H	K	L	(J-H)	(H-K)	(K-L)
1	5 46 44.52	0 05 24.73	7.56	7.08	6.74	6.74	0.48	0.34	0.00
2	5 46 18.93	0 03 28.61	10.64	9.17	8.02	6.51	1.47	1.15	1.51
3	5 46 43.22	0 04 37.47	8.67	8.33	8.13	8.03	0.34	0.20	0.10
4	5 46 43.12	0 00 53.43	12.64	10.63	8.69	6.15	2.01	1.94	2.54
5	5 46 45.26	0 02 43.00	9.85	9.20	8.79	8.41	0.65	0.41	0.38
6	5 46 43.43	0 05 30.00	10.25	9.34	8.86	8.60	0.91	0.48	0.26
7	5 46 21.12	0 10 23.17	9.84	9.15	8.92	8.79	0.69	0.23	0.13
8	5 46 37.02	0 01 22.24	11.46	10.22	9.29	8.16	1.24	0.93	1.13
9	5 46 19.13	0 00 18.88	12.45	10.77	9.33	8.69	1.68	1.44	0.64
10	5 46 34.27	0 06 44.47	11.93	10.56	9.69	8.98	1.37	0.87	0.71
11	5 46 57.98	0 05 41.83	11.21	10.20	9.71	9.23	1.01	0.49	0.48
12	5 46 35.84	0 06 27.94	13.28	11.28	9.85	8.42	2.00	1.43	1.43
13	5 46 44.87	0 05 35.90	11.73	10.67	9.94	9.39	1.06	0.73	0.55
14	5 46 47.18	0 04 09.20	12.50	11.13	10.02	8.63	1.37	1.11	1.39
15	5 46 50.09	0 04 42.23	11.71	10.71	10.09	9.27	1.00	0.62	0.82
16	5 46 40.15	0 04 55.17	11.39	10.51	10.12	9.87	0.88	0.39	0.25
17	5 46 24.46	0 10 42.10	13.29	11.29	10.25	9.59	2.00	1.04	0.66
18	5 46 46.53	0 09 09.70	11.93	10.97	10.26	9.48	0.96	0.71	0.78
19	5 46 18.57	-0 00 20.75	12.78	11.46	10.29	9.27	1.32	1.17	1.02
20	5 46 33.26	0 02 53.67	13.58	11.61	10.32	8.76	1.97	1.29	1.56
21	5 46 41.87	0 12 11.95	10.83	10.47	10.35	10.40	0.36	0.12	-0.05
22	5 46 53.68	0 00 08.74	12.78	11.43	10.35	8.83	1.35	1.08	1.52
23	5 46 35.05	0 08 58.77	10.96	10.52	10.36	10.38	0.44	0.16	-0.02
24	5 46 17.99	0 06 56.66	12.12	11.09	10.41	9.60	1.03	0.68	0.81
25	5 46 16.41	0 07 11.48	12.78	11.63	10.53	10.35	1.15	1.10	0.18
26	5 46 40.23	0 05 09.07	12.17	11.19	10.78	10.52	0.98	0.41	0.26
27	5 46 56.31	0 05 15.42	12.73	11.41	10.80	10.22	1.32	0.61	0.58
28	5 46 46.73	0 07 11.80	13.53	11.95	10.80	9.59	1.58	1.15	1.21
29	5 46 29.01	0 02 59.42	14.40	12.20	10.81	9.40	2.20	1.39	1.41
30	5 46 24.84	0 05 40.70	13.55	11.88	10.81	9.73	1.67	1.07	1.08
31	5 46 32.38	0 08 51.71	13.35	11.91	10.86	9.73	1.44	1.05	1.13
32	5 46 29.89	0 07 02.39	12.86	11.56	10.89	10.36	1.30	0.67	0.53
33	5 46 39.63	0 06 46.54	13.75	12.12	10.95	9.69	1.63	1.17	1.26

Table D-1–continued

ID	RA (2000)	Dec (2000)	J	H	K	L	(J-H)	(H-K)	(K-L)
34	5 46 38.10	0 05 49.89	13.14	11.89	10.99	10.07	1.25	0.90	0.92
35	5 46 31.32	0 06 40.63	13.20	11.84	11.01	9.73	1.36	0.83	1.28
36	5 46 34.75	0 04 21.48	12.59	11.56	11.03	10.65	1.03	0.53	0.38
37	5 46 27.61	0 05 48.22	12.69	11.65	11.12	10.58	1.04	0.53	0.54
38	5 46 39.99	0 05 03.07	12.60	11.67	11.24	10.97	0.93	0.43	0.27
39	5 46 45.03	0 03 48.22	13.24	12.01	11.25	10.67	1.23	0.76	0.58
40	5 46 53.85	0 00 36.81	13.04	11.96	11.32	10.71	1.08	0.64	0.61
41	5 46 22.80	0 04 25.43	12.90	11.90	11.35	10.96	1.00	0.55	0.39
42	5 46 18.28	0 07 06.82	13.92	12.45	11.46	10.91	1.47	0.99	0.55
43	5 46 47.35	0 03 38.63	13.04	11.97	11.50	11.08	1.07	0.47	0.42
44	5 46 51.53	0 03 55.53	14.42	12.86	11.57	10.32	1.56	1.29	1.25
45	5 46 47.31	0 05 27.37	13.08	12.08	11.58	10.88	1.00	0.50	0.70
46	5 46 35.45	0 01 39.28	13.32	12.23	11.58	10.71	1.09	0.65	0.87
47	5 46 23.63	0 04 26.32	13.44	12.20	11.58	11.02	1.24	0.62	0.56
48	5 46 29.15	0 10 57.38	13.26	12.28	11.59	10.78	0.98	0.69	0.81
49	5 46 39.93	0 07 18.08	14.14	12.61	11.65	11.14	1.53	0.96	0.51
50	5 47 00.43	0 04 02.25	13.00	12.09	11.66	11.06	0.91	0.43	0.60
51	5 46 37.43	0 04 03.53	12.94	12.15	11.68	11.35	0.79	0.47	0.33
52	5 46 48.04	0 05 55.17	13.61	12.33	11.68	11.20	1.28	0.65	0.48
53	5 46 45.40	0 05 50.42	13.79	12.46	11.70	10.93	1.33	0.76	0.77
54	5 46 25.48	0 09 31.08	13.04	12.19	11.72	10.74	0.85	0.47	0.98
55	5 46 37.25	0 06 55.99	14.09	12.73	11.81	10.96	1.36	0.92	0.85
56	5 46 25.62	0 07 09.10	14.45	12.86	11.81	10.83	1.59	1.05	0.98
57	5 46 47.57	0 04 58.86	13.69	12.54	11.83	10.77	1.15	0.71	1.06
58	5 46 52.50	0 06 11.99	14.26	12.86	11.84	10.72	1.40	1.02	1.12
59	5 46 32.92	0 06 23.03	14.58	12.83	11.84	11.09	1.75	0.99	0.75
60	5 46 42.18	0 06 11.03	14.65	12.97	12.00	11.19	1.68	0.97	0.81

¹Coordinates are approximate, and accurate to only a few arcseconds.

APPENDIX E
THE *JHK*L POSITIONS AND PHOTOMETRY FOR IC 348

Table E-1: The *JHK*L Photometry of IC 348 Sources

ID	RA (2000)	Dec (2000)	J ¹	H ¹	K ¹	L	(J-H)	(H-K)	(K-L)
1	3 44 34.15	32 09 44.58	7.74	7.63	6.97	6.44	0.11	0.66	0.53
2	3 44 35.36	32 10 02.71	8.28	8.01	7.45	6.87	0.27	0.56	0.58
3	3 44 31.07	32 06 20.26	8.55	8.28	7.93	7.77	0.27	0.35	0.16
4	3 44 25.92	32 04 29.97	10.15	8.97	7.95	7.04	1.18	1.02	0.91
5	3 44 36.89	32 06 43.11	9.22	8.59	8.21	7.84	0.63	0.38	0.37
6	3 44 08.35	32 07 17.23	8.91	8.78	8.66	8.51	0.13	0.12	0.15
7	3 44 09.05	32 07 09.99	8.93	8.77	8.68	8.59	0.16	0.09	0.09
8	3 44 39.15	32 09 15.98	9.94	9.15	8.75	8.42	0.79	0.40	0.33
9	3 44 24.64	32 10 14.05	9.30	8.97	8.82	8.68	0.33	0.15	0.14
10	3 44 32.09	32 11 42.90	9.95	9.32	8.90	8.32	0.63	0.42	0.58
11	3 44 55.04	32 12 08.52	10.28	9.35	8.94	8.59	0.93	0.41	0.35
12	3 44 32.62	32 08 36.67	10.14	9.58	9.36	9.29	0.56	0.22	0.07
13	3 44 30.85	32 09 54.48	9.80	9.56	9.41	9.25	0.24	0.15	0.16
14	3 44 56.18	32 09 11.75	10.90	9.97	9.48	8.75	0.93	0.49	0.73
15	3 44 38.73	32 08 39.90	11.09	10.01	9.51	9.12	1.08	0.50	0.39
16	3 44 35.00	32 07 35.13	10.70	9.88	9.52	9.42	0.82	0.36	0.10
17	3 44 20.98	32 07 38.47	10.01	9.74	9.67	9.49	0.27	0.07	0.18
18	3 44 31.52	32 08 44.04	10.56	9.92	9.68	9.54	0.64	0.24	0.14
19	3 44 19.12	32 09 30.58	10.07	9.83	9.73	9.70	0.24	0.10	0.03
20	3 44 18.01	32 04 56.55	11.93	10.60	9.73	9.12	1.33	0.87	0.61
21	3 44 37.82	32 08 02.56	11.62	10.51	9.75	9.02	1.11	0.76	0.73
22	3 44 32.52	32 08 41.48	10.79	10.09	9.82	9.76	0.70	0.27	0.06
23	3 44 39.21	32 07 33.37	11.26	10.30	9.90	9.27	0.96	0.40	0.63
24	3 44 38.41	32 07 33.62	11.19	10.28	9.91	9.42	0.91	0.37	0.49
25	3 44 23.96	32 10 59.29	10.62	10.17	10.06	9.87	0.45	0.11	0.19
26	3 44 29.76	32 10 38.64	11.85	10.82	10.16	9.27	1.03	0.66	0.89
27	3 44 21.65	32 10 36.93	12.22	11.05	10.20	8.74	1.17	0.85	1.46
28	3 44 42.05	32 08 58.40	11.99	10.92	10.20	9.56	1.07	0.72	0.64
29	3 44 24.24	32 10 18.57	11.09	10.03	10.29	10.12	1.06	-0.26	0.17
30	3 44 34.78	32 06 31.64	11.43	10.62	10.35	10.09	0.81	0.27	0.26
31	3 44 55.68	32 09 16.48	11.74	10.77	10.39	10.06	0.97	0.38	0.33
32	3 44 43.52	32 07 40.31	12.05	10.87	10.43	10.00	1.18	0.44	0.43
33	3 44 16.42	32 09 54.84	11.26	10.64	10.45	10.06	0.62	0.19	0.39

Table E-1-continued

ID	RA (2000)	Dec (2000)	J ^I	H ^I	K ^I	L	(J-H)	(H-K)	(K-L)
34	3 44 48.70	32 15 25.91	11.26	10.69	10.53	10.36	0.57	0.16	0.17
35	3 44 38.52	32 07 59.11	11.88	10.95	10.54	10.06	0.93	0.41	0.48
36	3 44 40.20	32 11 32.32	11.63	10.85	10.56	10.16	0.78	0.29	0.40
37	3 44 25.57	32 11 30.20	12.23	11.21	10.59	9.40	1.02	0.62	1.19
38	3 44 22.14	32 05 41.90	12.32	11.20	10.61	9.95	1.12	0.59	0.66
39	3 44 25.60	32 12 29.49	11.73	10.96	10.68	10.40	0.77	0.28	0.28
40	3 44 33.93	32 08 52.49	11.71	10.94	10.68	10.41	0.77	0.26	0.27
41	3 44 28.39	32 07 21.12	11.69	10.93	10.69	10.41	0.76	0.24	0.28
42	3 44 26.92	32 04 42.91	11.74	10.98	10.70	10.27	0.76	0.28	0.43
43	3 44 32.53	32 08 54.78	11.99	11.09	10.71	10.34	0.90	0.38	0.37
44	3 44 34.27	32 10 48.07	12.01	11.15	10.80	10.49	0.86	0.35	0.31
45	3 44 43.78	32 10 28.00	12.15	11.19	10.81	10.09	0.96	0.38	0.72
46	3 44 43.43	32 08 15.42	11.60	11.01	10.82	10.60	0.59	0.19	0.22
47	3 44 26.60	32 08 19.63	12.79	11.53	10.84	9.85	1.26	0.69	0.99
48	3 44 27.86	32 10 51.26	13.77	11.85	10.86	10.28	1.92	0.99	0.58
49	3 44 37.27	32 06 09.39	12.00	11.16	10.89	10.59	0.84	0.27	0.30
50	3 44 37.44	32 08 58.88	12.24	11.32	10.89	10.16	0.92	0.43	0.73
51	3 44 27.79	32 07 30.36	12.05	11.26	10.97	10.59	0.79	0.29	0.38
52	3 44 32.74	32 09 14.56	12.23	11.37	10.99	10.62	0.86	0.38	0.37
53	3 44 33.35	32 09 37.83	12.20	11.39	11.03	10.31	0.81	0.36	0.72
54	3 44 39.26	32 09 42.57	12.35	11.43	11.03	10.65	0.92	0.40	0.38
55	3 44 23.56	32 06 46.01	12.09	11.32	11.03	10.77	0.77	0.29	0.26
56	3 44 17.88	32 12 20.46	12.03	11.34	11.03	10.79	0.69	0.31	0.24
57	3 44 21.98	32 12 11.31	12.15	11.40	11.07	10.69	0.75	0.33	0.38
58	3 44 34.85	32 09 51.44	12.01	11.39	11.08	11.17	0.62	0.31	-0.09
59	3 44 25.46	32 06 16.30	12.78	11.61	11.09	10.49	1.17	0.52	0.60
60	3 44 38.45	32 05 03.92	12.39	11.52	11.10	10.77	0.87	0.42	0.33
61	3 44 19.18	32 07 34.68	12.40	11.58	11.10	10.41	0.82	0.48	0.69
62	3 44 22.38	32 12 00.39	12.38	11.55	11.10	10.39	0.83	0.45	0.71
63	3 44 36.07	32 15 01.57	12.74	11.60	11.11	10.69	1.14	0.49	0.42
64	3 44 44.53	32 08 10.55	12.91	11.82	11.12	10.18	1.09	0.70	0.94
65	3 44 11.13	32 06 12.26	12.36	11.43	11.16	11.00	0.93	0.27	0.16
66	3 44 14.13	32 10 28.18	12.34	11.55	11.19	10.75	0.79	0.36	0.44
67	3 44 38.64	32 08 54.61	12.31	11.53	11.22	11.05	0.78	0.31	0.17
68	3 44 40.26	32 14 26.01	12.44	11.66	11.23	10.89	0.78	0.43	0.34
69	3 44 37.51	32 12 22.58	12.90	11.83	11.24	10.49	1.07	0.59	0.75
70	3 44 45.15	32 13 34.12	12.42	11.66	11.26	10.77	0.76	0.40	0.49
71	3 44 37.14	32 09 14.00	12.36	11.53	11.26	11.16	0.83	0.27	0.10
72	3 44 29.93	32 09 19.83	13.40	11.95	11.27	10.61	1.45	0.68	0.66
73	3 44 21.54	32 10 16.64	12.30	11.51	11.28	10.88	0.79	0.23	0.40
74	3 44 21.12	32 05 01.76	12.54	11.65	11.29	10.99	0.89	0.36	0.30
75	3 44 22.98	32 11 56.95	12.41	11.62	11.30	11.14	0.79	0.32	0.16
76	3 44 21.55	32 06 24.23	12.43	11.61	11.33	10.96	0.82	0.28	0.37

Table E-1-continued

ID	RA (2000)	Dec (2000)	J ¹	H ¹	K ¹	L	(J-H)	(H-K)	(K-L)
77	3 44 20.11	32 08 55.82	12.54	11.75	11.36	10.86	0.79	0.39	0.50
78	3 44 21.28	32 11 56.05	12.54	11.70	11.36	10.84	0.84	0.34	0.52
79	3 44 27.34	32 14 20.19	12.78	11.93	11.39	10.78	0.85	0.54	0.61
80	3 44 41.81	32 12 00.62	13.02	11.95	11.39	10.88	1.07	0.56	0.51
81	3 44 45.27	32 14 10.81	13.31	12.10	11.46	11.10	1.21	0.64	0.36
82	3 44 25.34	32 10 11.81	12.56	11.86	11.47	10.96	0.70	0.39	0.51
83	3 44 30.47	32 06 28.00	12.68	11.81	11.48	11.11	0.87	0.33	0.37
84	3 44 16.32	32 05 32.35	13.24	12.03	11.49	11.15	1.21	0.54	0.34
85	3 44 38.53	32 12 57.82	12.59	11.82	11.50	11.19	0.77	0.32	0.31
86	3 44 41.38	32 10 22.94	12.48	11.78	11.51	11.11	0.70	0.27	0.40
87	3 44 42.59	32 06 16.77	12.43	11.69	11.52	11.30	0.74	0.17	0.22
88	3 44 36.93	32 08 32.41	13.02	12.10	11.56	10.92	0.92	0.54	0.64
89	3 44 34.88	32 11 16.43	12.70	11.94	11.60	11.18	0.76	0.34	0.42
90	3 44 42.74	32 08 31.56	12.95	12.10	11.60	10.66	0.85	0.50	0.94
91	3 44 37.91	32 12 16.55	12.78	12.02	11.61	11.26	0.76	0.41	0.35
92	3 44 18.59	32 12 53.32	13.65	12.66	11.65	10.32	0.99	1.01	1.33
93	3 44 40.15	32 09 10.62	13.13	12.18	11.66	11.19	0.95	0.52	0.47
94	3 44 47.70	32 10 52.96	13.35	12.23	11.68	11.10	1.12	0.55	0.58
95	3 44 35.43	32 08 54.40	13.08	12.27	11.77	11.12	0.81	0.50	0.65
96	3 44 42.57	32 10 00.07	13.45	12.38	11.78	10.83	1.07	0.60	0.95
97	3 44 41.17	32 10 07.76	13.56	12.37	11.79	10.94	1.19	0.58	0.85
98	3 44 31.37	32 10 45.75	13.31	12.35	11.81	11.12	0.96	0.54	0.69
99	3 44 17.61	32 04 47.27	13.01	12.26	11.81	11.36	0.75	0.45	0.45
100	3 44 28.48	32 11 21.62	14.40	12.66	11.83	11.13	1.74	0.83	0.70
101	3 44 44.90	32 11 03.23	13.00	12.15	11.85	11.42	0.85	0.30	0.43
102	3 44 48.96	32 13 19.49	12.93	12.19	11.88	11.83	0.74	0.31	0.05
103	3 44 21.79	32 12 31.22	12.98	12.25	11.92	11.41	0.73	0.33	0.51
104	3 44 18.13	32 09 58.84	13.14	12.34	11.93	11.26	0.80	0.41	0.67
105	3 44 53.72	32 06 48.70	13.22	12.34	11.94	11.54	0.88	0.40	0.40
106	3 44 21.65	32 15 09.53	12.93	12.27	11.96	11.54	0.66	0.31	0.42
107	3 44 46.40	32 11 14.24	13.89	12.57	11.98	11.74	1.32	0.59	0.24

¹JHK magnitudes were taken from Lada & Lada (1995).

APPENDIX F
THE *JHK*L POSITIONS AND PHOTOMETRY FOR NGC 2264

Table F-1: The *JHK*L Photometry of NGC 2264 Sources

ID	RA (2000) ¹	Dec (2000) ¹	J	H	K	L	(J-H)	(H-K)	(K-L)
1	6 41 02.42	09 59 18.85	10.74	9.58	8.92	8.47	1.16	0.66	0.45
2	6 41 16.70	09 57 52.15	9.37	9.27	9.14	9.16	0.10	0.13	-0.02
3	6 41 10.50	09 54 22.71	9.55	9.28	9.22	9.25	0.27	0.06	-0.03
4	6 41 18.12	09 56 28.66	11.48	10.57	9.99	9.45	0.91	0.58	0.54
5	6 40 59.96	10 00 02.09	10.22	10.13	10.10	10.10	0.09	0.03	0.00
6	6 41 05.55	09 59 36.55	10.13	10.14	10.15	10.21	-0.01	-0.01	-0.06
7	6 41 03.06	09 54 48.99	10.38	10.23	10.20	10.25	0.15	0.03	-0.05
8	6 41 00.31	09 57 32.01	11.45	10.74	10.26	9.70	0.71	0.48	0.56
9	6 41 18.42	10 01 08.28	14.04	11.63	10.43	9.72	2.41	1.20	0.71
10	6 41 00.71	09 59 55.46	12.85	11.45	10.50	9.27	1.40	0.95	1.23
11	6 41 10.51	09 55 43.55	13.40	11.73	10.78	9.86	1.67	0.95	0.92
12	6 41 04.97	09 57 53.49	11.32	10.94	10.79	10.82	0.38	0.15	-0.03
13	6 41 09.01	09 56 36.45	13.71	11.97	10.98	9.78	1.74	0.99	1.20
14	6 41 00.81	10 00 03.78	12.87	11.79	11.02	10.29	1.08	0.77	0.73
15	6 41 07.20	09 57 36.62	12.22	11.40	11.05	10.75	0.82	0.35	0.30
16	6 41 10.55	09 56 45.02	12.59	11.68	11.08	10.38	0.91	0.60	0.70
17	6 41 19.13	09 56 02.85	12.02	11.30	11.09	11.00	0.72	0.21	0.09
18	6 41 22.35	10 00 11.76	12.26	11.53	11.15	10.44	0.73	0.38	0.71
19	6 41 18.56	09 56 48.59	13.42	11.91	11.20	10.83	1.51	0.71	0.37
20	6 41 08.64	09 54 24.48	12.09	11.36	11.21	11.25	0.73	0.15	-0.04
21	6 41 02.01	09 55 51.60	12.18	11.35	11.21	10.57	0.83	0.14	0.64
22	6 41 08.52	09 57 13.28	14.93	12.70	11.32	10.44	2.23	1.38	0.88
23	6 41 10.42	09 57 44.34	14.11	12.39	11.35	10.35	1.72	1.04	1.00
24	6 41 16.24	09 59 11.32	12.41	11.59	11.35	11.18	0.82	0.24	0.17
25	6 41 09.61	10 00 43.97	12.87	11.80	11.38	10.98	1.07	0.42	0.40
26	6 41 05.07	09 57 04.41	12.71	11.87	11.47	10.95	0.84	0.40	0.52
27	6 41 19.35	09 55 37.90	13.17	12.08	11.51	11.15	1.09	0.57	0.36
28	6 41 19.63	10 00 28.65	12.48	11.78	11.51	11.45	0.70	0.27	0.06
29	6 41 06.78	09 59 47.93	12.41	11.73	11.56	11.45	0.68	0.17	0.11
30	6 41 14.72	09 58 25.86	12.69	11.95	11.57	11.01	0.74	0.38	0.56
31	6 41 09.94	10 00 47.22	15.39	12.86	11.57	11.01	2.53	1.29	0.56
32	6 41 15.86	09 59 56.44	12.49	11.81	11.63	11.60	0.68	0.18	0.03
33	6 41 07.79	09 56 06.75	12.94	11.98	11.69	11.55	0.96	0.29	0.14

Table F-1—continued

ID	RA (2000)	Dec (2000)	J	H	K	L	(J-H)	(H-K)	(K-L)
34	6 41 19.29	10 00 12.32	12.53	11.87	11.69	11.37	0.66	0.18	0.32
35	6 40 59.26	09 57 25.14	12.86	12.04	11.73	11.42	0.82	0.31	0.31
36	6 41 08.37	09 56 00.21	13.53	12.38	11.78	11.10	1.15	0.60	0.68
37	6 41 10.36	10 00 20.77	12.91	12.10	11.78	11.31	0.81	0.32	0.47
38	6 41 14.74	09 56 48.24	14.72	12.87	11.79	10.69	1.85	1.08	1.10
39	6 41 04.90	09 56 40.45	12.76	11.96	11.79	11.65	0.80	0.17	0.14
40	6 41 18.85	09 57 04.94	13.95	12.82	11.79	10.76	1.13	1.03	1.03
41	6 41 01.20	09 55 19.51	12.86	12.01	11.80	11.52	0.85	0.21	0.28
42	6 41 16.12	10 00 48.12	13.92	12.64	11.83	10.43	1.28	0.81	1.40
43	6 41 00.44	09 55 28.54	12.92	12.20	12.01	11.62	0.72	0.19	0.39
44	6 41 09.26	09 54 49.85	12.96	12.21	12.04	11.95	0.75	0.17	0.09
45	6 41 07.00	09 58 15.59	13.32	12.51	12.05	11.81	0.81	0.46	0.24
46	6 41 00.99	09 56 26.95	13.19	12.40	12.05	11.45	0.79	0.35	0.60
47	6 41 13.59	09 56 28.48	13.58	12.77	12.13	11.39	0.81	0.64	0.74
48	6 41 07.73	09 56 16.32	14.55	13.05	12.17	10.99	1.50	0.88	1.18
49	6 41 10.01	09 57 41.37	14.37	12.99	12.18	11.51	1.38	0.81	0.67
50	6 41 01.51	09 55 25.74	13.02	12.27	12.25	12.11	0.75	0.02	0.14
51	6 41 09.46	09 57 16.02	13.19	12.46	12.27	12.33	0.73	0.19	-0.06
52	6 41 09.73	09 56 58.57	13.56	12.77	12.31	11.94	0.79	0.46	0.37
53	6 41 11.57	09 58 04.09	13.43	12.72	12.47	12.32	0.71	0.25	0.15
54	6 41 05.20	09 54 56.02	13.54	12.75	12.49	12.13	0.79	0.26	0.36
55	6 41 11.81	09 55 10.14	13.25	12.73	12.55	12.29	0.52	0.18	0.26
56	6 41 12.46	10 00 47.02	15.23	13.48	12.62	11.99	1.75	0.86	0.63
57	6 41 14.83	09 56 59.74	14.81	13.52	12.68	11.58	1.29	0.84	1.10
58	6 41 13.29	09 57 02.71	14.30	13.25	12.69	12.28	1.05	0.56	0.41
59	6 41 18.21	09 56 58.52	15.55	13.77	12.73	11.86	1.78	1.04	0.87
60	6 41 11.62	09 57 06.88	13.83	13.20	12.97	11.95	0.63	0.23	1.02

¹*JHK* coordinates adopted from the 2MASS archive (<http://pegasus.astro.umass.edu>).

APPENDIX G
THE *JHK*L POSITIONS AND PHOTOMETRY FOR NGC 2362

Table G-1: The *JHK*L Photometry of NGC 2362 Sources

ID	RA (2000) ¹	Dec (2000) ¹	J	H	K	L	(J-H)	(H-K)	(K-L)
1	7 18 48.59	-24 56 55.62	8.61	8.64	8.61	8.69	-0.03	0.03	-0.08
2	7 18 38.23	-24 57 00.00	10.24	9.69	9.40	9.24	0.55	0.29	0.16
3	7 18 49.88	-24 57 48.24	9.69	9.70	9.64	9.60	-0.01	0.06	0.04
4	7 18 42.04	-24 58 11.46	10.04	10.10	10.03	9.95	-0.06	0.07	0.08
5	7 18 38.46	-24 58 19.08	9.84	9.97	10.05	9.78	-0.13	-0.08	0.27
6	7 18 37.54	-24 57 41.38	10.01	10.03	10.09	9.76	-0.02	-0.06	0.33
7	7 18 38.87	-24 56 14.99	10.41	10.34	10.20	10.00	0.07	0.14	0.20
8	7 18 43.17	-24 58 18.05	10.30	10.33	10.29	10.15	-0.03	0.04	0.14
9	7 18 44.73	-24 57 37.00	10.67	10.42	10.41	10.12	0.25	0.01	0.29
10	7 18 46.25	-24 57 46.81	10.37	10.36	10.41	10.37	0.01	-0.05	0.04
11	7 18 39.31	-24 56 52.95	11.08	10.85	10.47	9.48	0.23	0.38	0.99
12	7 18 40.89	-24 58 26.62	10.56	10.56	10.55	10.31	0.00	0.01	0.24
13	7 18 53.28	-24 57 23.20	10.65	10.58	10.63	10.33	0.07	-0.05	0.30
14	7 18 42.95	-24 55 48.62	11.10	11.10	11.16	10.88	0.00	-0.06	0.28
15	7 18 43.31	-24 59 05.29	11.45	11.17	11.20	10.71	0.28	-0.03	0.49
16	7 18 34.13	-24 58 00.10	11.61	11.38	11.30	11.00	0.23	0.08	0.30
17	7 18 41.52	-24 55 55.74	11.66	11.40	11.31	11.02	0.26	0.09	0.29
18	7 18 34.33	-24 56 44.57	11.26	11.29	11.34	11.06	-0.03	-0.05	0.28
19	7 18 44.51	-24 56 51.69	11.86	11.40	11.36	11.09	0.46	0.04	0.27
20	7 18 41.62	-24 57 43.64	11.54	11.48	11.47	11.25	0.06	0.01	0.22
21	7 18 38.17	-24 59 00.58	11.65	11.65	11.55	11.36	0.00	0.10	0.19
22	7 18 42.84	-24 58 18.42	12.17	11.79	11.64	11.42	0.38	0.15	0.22
23	7 18 45.84	-24 58 44.95	11.80	11.67	11.67	11.27	0.13	0.00	0.40
24	7 18 40.25	-24 58 48.37	11.84	11.80	11.75	11.52	0.04	0.05	0.23
25	7 18 46.86	-24 59 18.04	12.68	12.03	11.80	11.12	0.65	0.23	0.68
26	7 18 44.72	-24 55 14.38	12.56	11.93	11.84	11.49	0.63	0.09	0.35
27	7 18 54.63	-24 57 28.99	12.12	11.95	11.91	11.54	0.17	0.04	0.37
28	7 18 42.33	-24 58 37.13	11.96	11.94	11.93	11.72	0.02	0.01	0.21
29	7 18 41.37	-24 57 25.44	12.25	12.02	12.00	11.75	0.23	0.02	0.25
30	7 18 34.75	-24 56 11.14	12.25	12.24	12.14	11.90	0.01	0.10	0.24
31	7 18 43.77	-24 58 34.51	12.72	12.28	12.16	11.66	0.44	0.12	0.50
32	7 18 51.59	-24 58 19.64	12.77	12.44	12.21	11.99	0.33	0.23	0.22
33	7 18 41.72	-24 56 00.92	12.60	12.37	12.26	12.00	0.23	0.11	0.26

Table G-1-continued

ID	RA (2000) ¹	Dec (2000) ¹	J	H	K	L	(J-H)	(H-K)	(K-L)
34	7 18 43.85	-24 55 04.25	12.59	12.29	12.28	11.92	0.30	0.01	0.36
35	7 18 47.01	-24 55 32.51	12.43	12.30	12.30	11.83	0.13	0.00	0.47
36	7 18 46.93	-24 56 59.92	13.51	12.83	12.45	12.34	0.68	0.38	0.11
37	7 18 38.01	-24 58 52.48	13.30	12.79	12.50	12.33	0.51	0.29	0.17
38	7 18 55.16	-24 56 44.52	12.65	12.58	12.54	12.30	0.07	0.04	0.24
39	7 18 48.28	-24 57 22.44	13.78	13.02	12.62	12.42	0.76	0.40	0.20
40	7 18 38.17	-24 55 48.46	13.68	13.03	12.65	12.43	0.65	0.38	0.22
41	7 18 49.28	-24 56 18.85	13.48	12.87	12.65	12.38	0.61	0.22	0.27
42	7 18 43.47	-24 56 17.27	13.46	12.86	12.68	12.39	0.60	0.18	0.29
43	7 18 42.80	-24 56 55.10	13.66	12.88	12.73	12.33	0.78	0.15	0.40
44	7 18 35.74	-24 58 11.22	12.95	12.84	12.78	12.39	0.11	0.06	0.39
45	7 18 40.78	-24 56 36.15	14.33	13.44	12.81	12.47	0.89	0.63	0.34
46	7 18 42.24	-24 57 58.13	13.33	12.94	12.82	12.58	0.39	0.12	0.24
47	7 18 50.96	-24 57 03.32	13.66	13.03	12.85	12.60	0.63	0.18	0.25
48	7 18 47.13	-24 55 11.83	13.60	13.07	12.85	12.39	0.53	0.22	0.46
49	7 18 45.70	-24 57 17.17	13.57	12.94	12.87	12.54	0.63	0.07	0.33
50	7 18 43.98	-24 54 26.29	13.07	12.97	12.91	12.46	0.10	0.06	0.45
51	7 18 49.35	-24 57 15.34	14.02	13.24	12.98	12.70	0.78	0.26	0.28
52	7 18 39.00	-24 58 23.67	13.83	13.26	13.00	12.66	0.57	0.26	0.34
53	7 18 43.55	-24 57 46.61	13.90	13.19	13.00	12.59	0.71	0.19	0.41
54	7 18 39.97	-24 56 53.47	15.67	14.22	13.02	11.57	1.45	1.20	1.45
55	7 18 46.63	-24 55 09.81	13.80	13.13	13.03	12.59	0.67	0.10	0.44
56	7 18 41.89	-24 55 51.81	13.84	13.23	13.06	12.55	0.61	0.17	0.51
57	7 18 40.33	-24 55 12.45	13.82	13.25	13.07	13.05	0.57	0.18	0.02
58	7 18 49.74	-24 58 26.18	14.00	13.38	13.08	12.79	0.62	0.30	0.29
59	7 18 42.11	-24 57 58.85	14.02	13.31	13.08	12.80	0.71	0.23	0.28
60	7 18 33.07	-24 57 03.00	13.48	13.18	13.13	12.80	0.30	0.05	0.33
61	7 18 53.24	-24 57 56.11	14.21	13.46	13.14	12.49	0.75	0.32	0.65
62	7 18 44.25	-24 57 08.65	13.94	13.24	13.16	12.73	0.70	0.08	0.43
63	7 18 35.82	-24 56 39.27	13.94	13.33	13.17	12.77	0.61	0.16	0.40
64	7 18 50.10	-24 56 08.94	13.79	13.39	13.22	12.96	0.40	0.17	0.26
65	7 18 48.42	-24 57 14.42	14.32	13.61	13.26	13.23	0.71	0.35	0.03
66	7 18 39.04	-24 58 46.16	14.24	13.59	13.27	12.86	0.65	0.32	0.41
67	7 18 45.68	-24 57 12.30	14.09	13.37	13.27	12.87	0.72	0.10	0.40
68	7 18 42.65	-24 57 34.60	14.08	13.38	13.33	12.90	0.70	0.05	0.43
69	7 18 37.59	-24 54 38.63	14.20	13.54	13.33	13.06	0.66	0.21	0.27
70	7 18 46.51	-24 57 09.21	14.13	13.39	13.34	12.85	0.74	0.05	0.49
71	7 18 38.00	-24 54 46.00	13.79	13.51	13.34	13.22	0.28	0.17	0.12
72	7 18 44.50	-24 55 32.05	13.68	13.38	13.38	12.85	0.30	0.00	0.53
73	7 18 40.55	-24 57 21.89	14.49	13.66	13.42	12.91	0.83	0.24	0.51
74	7 18 36.80	-24 57 39.46	13.87	13.52	13.44	12.68	0.35	0.08	0.76
75	7 18 45.64	-24 56 05.97	14.23	13.61	13.46	13.30	0.62	0.15	0.16
76	7 18 49.49	-24 56 25.26	14.70	13.89	13.47	12.86	0.81	0.42	0.61

Table G-1-continued

ID	RA (2000) ¹	Dec (2000) ¹	J	H	K	L	(J-H)	(H-K)	(K-L)
77	7 18 33.28	-24 58 09.72	13.98	13.65	13.48	13.23	0.33	0.17	0.25
78	7 18 37.73	-24 54 52.90	14.57	13.88	13.53	13.72	0.69	0.35	-0.19
79	7 18 38.67	-24 58 02.78	14.64	13.92	13.54	13.28	0.72	0.38	0.26
80	7 18 47.12	-24 58 51.78	14.36	13.66	13.55	13.08	0.70	0.11	0.47
81	7 18 40.66	-24 57 38.95	14.40	13.77	13.57	13.29	0.63	0.20	0.28
82	7 18 33.41	-24 57 07.83	13.94	13.63	13.62	13.33	0.31	0.01	0.29
83	7 18 46.71	-24 58 41.44	14.63	13.88	13.72	13.29	0.75	0.16	0.43
84	7 18 43.15	-24 58 40.95	14.27	13.82	13.75	13.31	0.45	0.07	0.44
85	7 18 42.00	-24 58 49.82	14.73	13.97	13.75	13.33	0.76	0.22	0.42
86	7 18 53.23	-24 56 37.09	14.76	14.05	13.76	13.59	0.71	0.29	0.17
87	7 18 49.57	-24 56 37.39	14.83	14.06	13.80	13.31	0.77	0.26	0.49
88	7 18 39.31	-24 56 30.99	14.89	14.14	13.82	13.53	0.75	0.32	0.29
89	7 18 34.47	-24 56 11.81	14.64	14.11	13.88	13.34	0.53	0.23	0.54
90	7 18 38.40	-24 58 15.80	13.86	13.91	13.90	14.00	-0.05	0.01	-0.10
91	7 18 43.51	-24 57 38.46	14.79	14.08	13.92	13.32	0.71	0.16	0.60
92	7 18 44.70	-24 57 51.07	14.91	14.13	13.94	13.70	0.78	0.19	0.24
93	7 18 47.98	-24 57 11.63	15.15	14.36	13.95	13.59	0.79	0.41	0.36
94	7 18 48.38	-24 57 38.14	14.67	14.21	13.97	14.05	0.46	0.24	-0.08

¹*JHK* coordinates kindly provided by João Alves.

APPENDIX H
THE *JHK*L POSITIONS AND PHOTOMETRY FOR NGC 1960

Table H-1: The *JHK*L Photometry of NGC 1960 Sources

ID	RA (2000) ¹	Dec (2000) ¹	J	H	K	L	(J-H)	(H-K)	(K-L)
1	5 36 15.81	34 08 36.54	8.73	8.78	8.80	8.89	-0.05	-0.02	-0.09
2	5 36 23.05	34 10 32.52	8.86	8.90	8.91	8.96	-0.04	-0.01	-0.05
3	5 36 07.90	34 08 50.25	9.27	9.34	9.34	9.35	-0.07	0.00	-0.01
4	5 36 21.06	34 10 16.61	9.62	9.65	9.66	9.66	-0.03	-0.01	0.00
5	5 36 23.84	34 05 57.19	9.66	9.69	9.68	9.68	-0.03	0.01	0.00
6	5 36 00.91	34 09 07.56	11.09	10.08	9.75	9.69	1.01	0.33	0.06
7	5 36 02.39	34 06 50.86	9.85	9.89	9.89	9.81	-0.04	0.00	0.08
8	5 36 07.20	34 08 03.35	10.01	10.01	9.99	9.89	0.00	0.02	0.10
9	5 36 09.77	34 11 35.89	10.12	10.17	10.16	10.23	-0.05	0.01	-0.07
10	5 36 21.39	34 09 40.99	10.38	10.38	10.36	10.37	0.00	0.02	-0.01
11	5 36 05.98	34 06 11.98	13.36	12.00	10.46	8.73	1.36	1.54	1.73
12	5 36 12.57	34 08 58.55	10.48	10.51	10.52	10.52	-0.03	-0.01	0.00
13	5 36 01.96	34 09 17.58	10.80	10.74	10.71	10.91	0.06	0.03	-0.20
14	5 36 12.06	34 08 24.73	12.36	11.17	10.74	10.46	1.19	0.43	0.28
15	5 36 07.74	34 09 24.98	10.95	10.88	10.80	10.78	0.07	0.08	0.02
16	5 36 20.23	34 10 08.62	12.29	11.15	10.82	10.58	1.14	0.33	0.24
17	5 36 22.14	34 07 13.77	10.87	10.84	10.86	10.78	0.03	-0.02	0.08
18	5 36 09.24	34 08 21.00	12.07	11.23	10.89	10.71	0.84	0.34	0.18
19	5 36 24.85	34 10 32.47	12.24	11.44	11.17	11.02	0.80	0.27	0.15
20	5 36 28.35	34 07 21.44	11.44	11.41	11.38	11.27	0.03	0.03	0.11
21	5 36 14.46	34 08 23.92	11.66	11.48	11.42	11.39	0.18	0.06	0.03
22	5 36 18.57	34 10 45.97	11.61	11.55	11.48	11.46	0.06	0.07	0.02
23	5 36 20.75	34 06 50.13	11.63	11.52	11.49	11.40	0.11	0.03	0.09
24	5 36 12.85	34 07 55.01	12.37	11.76	11.52	11.25	0.61	0.24	0.27
25	5 36 26.44	34 07 39.15	12.06	11.68	11.54	11.44	0.38	0.14	0.10
26	5 36 13.78	34 10 18.05	12.50	11.81	11.55	11.42	0.69	0.26	0.13
27	5 36 02.66	34 06 06.12	11.55	11.57	11.56	11.45	-0.02	0.01	0.11
28	5 36 15.31	34 07 53.06	12.58	11.92	11.61	11.38	0.66	0.31	0.23
29	5 36 26.58	34 06 21.39	11.84	11.71	11.63	11.51	0.13	0.08	0.12
30	5 36 20.03	34 06 11.48	11.80	11.71	11.66	11.51	0.09	0.05	0.15
31	5 36 11.45	34 09 33.68	12.05	11.78	11.67	11.69	0.27	0.11	-0.02
32	5 36 21.53	34 09 51.05	11.74	11.69	11.68	11.63	0.05	0.01	0.05
33	5 36 09.18	34 08 56.90	12.97	12.10	11.72	11.50	0.87	0.38	0.22

Table H-1- continued

ID	RA (2000) ¹	Dec (2000) ¹	J	H	K	L	(J-H)	(H-K)	(K-L)
34	5 36 03.99	34 06 55.28	13.69	12.55	11.73	11.34	1.14	0.82	0.39
35	5 36 01.71	34 06 21.76	12.03	11.88	11.82	11.76	0.15	0.06	0.06
36	5 36 24.09	34 09 07.41	12.91	12.10	11.83	11.77	0.81	0.27	0.06

¹*JHK* coordinates adopted from the 2MASS archive (<http://pegasus.astro.umass.edu>).

REFERENCES

- Adams, F. C., Lada, C. J., & Shu, F. H. 1987, *ApJ*, 321, 788
- Ali, B. & Depoy, D. L. 1995, *AJ*, 109, 709
- André, P., & Montmerle, T. 1994, *ApJ*, 420, 837
- Anthony-Twarog, B. J. 1982, *AJ*, 87, 1213
- Appenzeller, I., Jankovics, I., & Ostreicher, R. 1984, *A&A*, 141, 108
- Aspin, C., Reipurth, B., & Lehmann, T. 1994, *A&A*, 288, 165
- Aspin, C., & Sandell, G. 1997, *MNRAS*, 289, 1
- Bally, J., Langer, W. D., & Liu, W. 1991, *ApJ*, 383, 645
- Bally, J., Sutherland, R. S., Devine, D., & Johnstone, D. 1998, *AJ*, 116, 293
- Balona, L. A., & Laney, C. D. 1996, *MNRAS*, 281, 1341
- Barkhatova, K. A., Zakharova, P. E., Shashkina, L. P., & Orekhova, L. K. 1985, *Soviet Astronomy*, 62, 854
- Barnes, P. J., Crutcher, R. M., Biegging, J. H., Storey, J. W. V., & Willner, S. P. 1989, *ApJ*, 342, 883
- Barsony, M., Kenyon, S. J., Lada, E. A., & Teuben, P. J. 1997, *ApJS*, 112, 109
- Beckwith, S. V. W. 1999, in *The Origin of Stars and Planetary Systems*, edited by C. J. Lada and N. Kylafis (Kluwer, Dordrecht), 579
- Beckwith, S. V. W., & Sargent, A. I. 1993, in *Protostars and Planets III*, ed. E. H. Levy and J. I. Lunine, Univ. of Arizona Press, 521
- Beckwith, S. V. W., Sargent, A. I., Chini, R. S., & Guesten, R. 1990, *AJ*, 99, 924
- Bernasconi, P. A., & Maeder, A. 1996, *A&A*, 307, 829
- Bessell, M. S. & Brett, J. M. 1988, *PASP*, 100, 1134
- Boss, A. P. 1998, *ApJ*, 503, 923
- Boss, A. P. 2000, *ApJ*, 536, L101
- Brandner, W., Zinnecker, H., Alcalá, J. M., Allard, F., Covino, E., Frink, S., Köhler, R., Kunkel, M., Moneti, A., & Schweitzer, A. 2000, *AJ*, 120, 950
- Carpenter, J. M. 2000, *AJ*, in press

- Carpenter, J. M., Snell, R. L., & Schloerb, F. P. 1995, *ApJ*, 450, 201
- Churchwell, E., Wood, D. O. S., Felli, M., & Massi, M. 1987, *ApJ*, 321, 516
- Cohen, J. G., Frogel, J. A., Persson, S. E., & Elias, J. H. 1981, *ApJ*, 249, 481
- Cohen, M., Witteborn, F. C., Walker, R. G., Bregman, J. D., & Wooden, D. H. 1995, *AJ*, 110, 275
- Comerón, F., Rieke, G. H., & Rieke, M. J. 1996, *ApJ*, 473, 294
- Dahari, D., & Lada, E. A. 2001, *AJ*, in preparation
- D'Antona, F., & Mazzitelli, I. 1994, *ApJS*, 90, 467
- D'Antona, F., & Mazzitelli, I. 1997, *Mem. Soc. Astron. Italiana*, 68, 4
- Dolan, C. J., & Mathieu, R. D. 1999, *AJ*, 118, 2409
- Dutrey, A., Guilloteau, S., Duvert, G., Prato, L., Simon, M., Schuster, K., & Menard, F. 1996, *A&A*, 309, 493
- Elias, J. H., Frogel, J. A., Matthews, K., & Neugebauer, G. 1982, *ApJ*, 87, 102
- Elsässer, H., & Staude, J. 1978, *A&A*, 70, L3
- Felli, M., Taylor, G. B., Catarzi, M., Churchwell, E., & Kurtz, S. 1993, *A&AS*, 101, 127
- Genzel, R., Reid, M. J., Moran, J. M. & Downes, D. 1981, *ApJ*, 244, 884
- Gibb, A. G. 1999, *MNRAS*, 304, 1
- Gibb, A. G., & Little, L. T. 2000, *MNRAS*, 313, 663
- Greene, T. P., & Meyer, M. R. 1995, *ApJ*, 450, 233
- Greene, T. P., Wilking, B. A., André, P., Young, E. T., & Lada, C. J. 1994, *ApJ*, 434, 614
- Herbig, G. H. 1998, *ApJ*, 497, 736
- Herbst, W., Maley, J. A., & Williams, E. C. 2000, *AJ*, 120, 349
- Hillenbrand, L. A. 1997, *AJ*, 113, 1733
- Hillenbrand, L. A., Strom, S. E., Calvet, N., Merrill, K. M., Gatley, I., Makidon, R. B., Meyer, M. R., & Skrutskie, M. F. 1998, *AJ*, 116, 1816
- Horner, D. J., Lada, E. A., & Lada, C. J. 1997, *AJ*, 113, 1788
- Johnstone, D., Hollenbach, D., & Bally, J. 1998, *ApJ*, 499, 758
- Kenyon, S. J., Gomez, M., Marzke, R. O., & Hartmann, L. 1994b, *AJ*, 108, 251
- Kenyon, S. J., & Hartmann, L. W. 1995, *ApJS*, 101, 117
- Kenyon, S. J., Hartmann, L. W., Strom, K. M., & Strom, S. E. 1990, *AJ*, 99, 869
- Kenyon, S. J., Lada, E. A., & Barsony, M. 1998, *AJ*, 115, 252
- Koornneef, J. 1983, *A&A*, 128, 84

- Lada, C. J. 1987, in *Star Forming Regions*, edited by M. Peimbert & J. Jugaku (Dordrecht, Reidel), 1
- Lada, C. J. 1999a, in *The Origin of Stars and Planetary Systems*, edited by C. J. Lada and N. Kylafis (Kluwer, Dordrecht), 143
- Lada, C. J., & Adams, F. C. 1992, *ApJ*, 393, 278
- Lada, C. J., Alves, J., & Lada, E. A. 1996, *AJ*, 111, 1964
- Lada, C. J., & Kylafis, N. D. 1991, *The Physics of Star Formation and Early Stellar Evolution*, (Kluwer, Dordrecht)
- Lada, C. J., & Kylafis, N. D. 1999, *The Origin of Stars and Planetary Systems*, (Kluwer, Dordrecht)
- Lada, C. J., Muench, A. A., Haisch, Jr., K. E., Lada, E. A., Alves, J. F., Tollestrup, E. V., & Willner, S. P. 2000, *AJ*, in press
- Lada, C. J., Young, E. T., & Greene, T. P. 1993, *ApJ*, 408, 471
- Lada, E. A. 1992, *ApJ*, 393, L25
- Lada, E. A. 1999, in *The Origin of Stars and Planetary Systems*, edited by C. J. Lada and N. Kylafis (Kluwer, Dordrecht), 441
- Lada, E. A., Depoy, D. L., Evans, N. J. , II, & Gatley, I. 1991, *ApJ*, 371, 171
- Lada, E. A., Evans II, N. J., & Falgarone, E. 1997, *ApJ*, 488, 286
- Lada, E. A., & Lada, C. J. 1995, *AJ*, 109, 1682
- Launhardt, R., Mezger, P. G., Haslam, C. G. T., Kreysa, E., Lemke, R., Seivers, A., & Zylka, R. 1996, *A&A*, 312, 569
- Levy, E. H., & Lunine, J. I. 1993, *Protostars and Planets III*, Univ. of Arizona Press
- Lissauer, J. J. 1987, *Icarus*, 69, 249
- Luhman, K. L. 1999, *ApJ*, 525, 466
- Luhman, K. L., Rieke, G. H., Lada, C. J., & Lada, E. A. 1998, *ApJ*, 508, 347
- Lynden-Bell, D., & Pringle, J. E. 1974, *MNRAS*, 168, 603
- Mannings, V., Boss, A., & Russell, S. 2000, *Protostars and Planets IV*, Univ. of Arizona Press
- Marcy, G. W., & Butler, R. P. 1999, in *The Origin of Stars and Planetary Systems*, edited by C. J. Lada and N. Kylafis (Kluwer, Dordrecht), 681
- Marcy, G. W., Cochran, W. D., & Mayor, M. 2000, in *Protostars & Planets IV*, ed. V. Mannings, A. P. Boss, & S. S. Russell (Tucson: Univ. Arizona Press), 1285
- Martín, E. L. 1997, *A&A*, 321, 492
- Mathis, J. S. 1990, *ARA&A*, 28, 37
- McCaughrean, M. J. & O'Dell, C. R. 1996, *AJ*, 111, 1977

- McCaughrean, M. J., & Stauffer, J. R. 1994, *AJ*, 108, 1382
- Ménard, F., & Bertout, C. 1999, in *The Origin of Stars and Planetary Systems*, edited by C. J. Lada and N. Kylafis (Kluwer, Dordrecht), 341
- Meyer, M. R. 1996, Ph.D. thesis, University of Massachusetts
- Meyer, M. R., Calvet, N., & Hillenbrand, L. A. 1997, *AJ*, 114, 233
- Meyer, M., & Lada, E. A. 1999, in *Orion Revisited*, edited by M. McCaughrean (ASP, San Francisco), in press
- Mundt, R., & Fried, J. 1983, *ApJ*, 274, L83
- Myers, P. C., Fuller, G. A., Mathieu, R. D., Beichman, C. A., Benson, P. J., Schild, R. E., & Emerson, J. P. 1987, *ApJ*, 319, 340
- O'Dell, C. R., Wen, Z., & Hu, X. 1993, *ApJ*, 410, 696
- O'Dell, C. R., & Wong, K. 1996, *AJ*, 111, 846
- Osterloh, M., & Beckwith, S. V. W. 1995, *ApJ*, 439, 288
- Ostriker, E. C. 1994, *ApJ*, 424, 292
- Parker, J. W. M. 1991, *PASP*, 103, 243
- Perez, M. R., Thé, P. S., & Westerlund, B. E. 1987, *PASP*, 99, 1050
- Phelps, R. L., & Lada, E. A. 1997, *ApJ*, 477, 176
- Pollack, J. B., Hubickyj, O., Bodenheimer, P., Lissauer, J. J., Podolak, M., & Greenzweig, Y. 1996, *Icarus*, 124, 62
- Rieke, G. H., & Lebofsky, M. J. 1985, *ApJ*, 288, 618
- Rucinski, S. M. 1985, *AJ*, 90, 2321
- Ruden, S. P. 1999, in *The Origin of Stars and Planetary Systems*, edited by C. J. Lada and N. Kylafis (Kluwer, Dordrecht), 643
- Sanner, J., Altmann, M., Brunzendorf, J., & Geffert, M. 2000, *A&A*, 357, 471
- Sato, S., Nagata, T., Tanaka, M., & Yamamoto, T. 1990, *ApJ*, 359, 192
- Scholz, R. D., Brunzendorf, J., Ivanov, G., Kharchenko, N., Lasker, B., Meusinger, H., Preibisch, T., Schilbach, E., & Zinnecker, H. 1999, *A&AS*, 137, 305
- Shu, F. H., Adams, F. C., & Lizano, S. 1987, *Ann. Rev. Astron. Astrophys.*, 25, 23
- Snell, R. L., Loren, R. B., & Plambeck, R. L. 1980, *ApJ*, 239, L17
- Soderblom, D. R., King, J. R., Siess, L., Jones, B. F., & Fischer, D. 1999, *AJ*, 118, 1301
- Stetson, P. 1987, *PASP*, 99, 191
- Störzer, H., & Hollenbach, D. 1999, *ApJ*, 515, 669
- Strom, K. M., Strom, S. E., Edwards, S., Cabrit, S., & Skrutskie, M. F. 1989, *AJ*, 97, 1451
- Strom, K. M., Strom, S. E., & Merrill, K. M. 1993, *ApJ*, 412, 233

- Strom, S. E., Edwards, S., & Skrutskie, M. F. 1993 in *Protostars and Planets III*, edited by E. H. Levy and J. I. Lunine, Univ. of Arizona Press, 837
- Strom, S. E., Strom, K. A., & Carrasco, L. 1974, *PASP*, 86, 798
- Sung, H., Bessell, M. S., & Lee, S. 1997, *AJ*, 114, 2644
- Swenson, F. J., Faulkner, J., Rodgers, F. J., & Iglesias, C. A. 1994, *ApJ*, 425, 286
- Thompson, R. I., Thronson, H. A. , Jr. & Campbell, B. G. 1981, *ApJ*, 249, 622
- Walker, M. F. 1956, *ApJS*, 2, 365
- Walter, F. 1987, *PASP*, 99, 31
- Walter, F. M., & Barry, D. C. in *The Sun in Time*, edited by C. P. Sonett, M. S. Giampapa and M. S. Matthews, (Tucson: Univ. Arizona Press), 633
- Whittet, D. C. B., Bode, M. F., Longmore, A. J., Admason, A. J., McFadzean, A. D., Aitken, D. K., & Roche, P. F. 1988, *MNRAS*, 233, 321
- Wilking, B. A., Lada, C. J., & Young, E. T. 1989, *ApJ*, 340, 823
- Wilner, D. J., Ho, P. T. P., Kastner, J. H., & Rodriguez, L. F. 2000, in press
- Young, E. T., Lada, C. J., & Wilking, B. A. 1986, *ApJ*, 304, L45

BIOGRAPHICAL SKETCH

Ever since I was young, I have wanted to pursue an astronomical career. I received my first telescope when I was about 10 years old. I remember the frustration that I experienced trying to find anything with it. Many nights were spent outdoors just attempting to find even a star with the telescope. Eventually, however, my patience paid off; I found my first star. Then I stumbled across Venus and soon many other objects. These observing sessions were supplemented with trips to the local library to learn as much as I could about astronomy. I have pursued my love for astronomy as an amateur ever since. However, in high school I discovered that astronomy was an actual profession, and I could be paid to do what I loved most. At this point, there was no question what my career path would be.


After high school, I attended Michigan State University for four years, graduating in June of 1989 with a Bachelor of Science degree in astrophysics. While at Michigan State, I began an undergraduate thesis project with Dr. Susan Simkin involving the environment around Seyfert galaxies. The results of this research were presented at the June 1990 meeting of the American Astronomical Society. I remained at Michigan State for an additional two years to pursue a Master of Science degree in physics. My undergraduate work was extended into a kinematic and dynamical study of the companions around Seyfert galaxies and their possible involvement with the nuclear activity observed in these objects. This research culminated in a master's thesis and the publication of two papers.

After graduating from Michigan State in August of 1991, I accepted a position as a physics and astronomy instructor for three years at Illinois Central College in East Peoria, Illinois. My responsibilities included teaching physics and astronomy to undergraduate engineering and physics majors. During this time, I obtained valuable experience and found that my desire to pursue astronomy as a career had been strengthened. I decided to

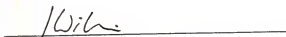
attend the University of Florida to obtain a Ph.D. because of the work done by faculty in infrared astronomy.

Three years ago, I began a research project with Dr. Elizabeth Lada involving the properties of circumstellar disks in young stellar clusters. This work represents the culmination of my efforts to pursue an astronomical career. After graduation, I will begin a National Research Council postdoctoral fellowship at NASA Ames Research Center in Mountain View, California under Dr. Thomas P. Greene.

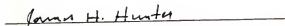
I certify that I have read this study and that in my opinion it conforms to acceptable standards of scholarly presentation and is fully adequate, in scope and quality, as a dissertation for the degree of Doctor of Philosophy.


Elizabeth A. Lada, Chairman
Associate Professor of Astronomy

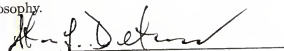
I certify that I have read this study and that in my opinion it conforms to acceptable standards of scholarly presentation and is fully adequate, in scope and quality, as a dissertation for the degree of Doctor of Philosophy.


Jonathan P. Williams
Assistant Professor of Astronomy

I certify that I have read this study and that in my opinion it conforms to acceptable standards of scholarly presentation and is fully adequate, in scope and quality, as a dissertation for the degree of Doctor of Philosophy.



James H. Hunter
Professor of Astronomy

I certify that I have read this study and that in my opinion it conforms to acceptable standards of scholarly presentation and is fully adequate, in scope and quality, as a dissertation for the degree of Doctor of Philosophy.


Steven L. Detweiler
Professor of Physics

This dissertation was submitted to the Graduate Faculty of the Department of Astronomy in the College of Liberal Arts and Sciences and to the Graduate School and was accepted as partial fulfillment of the requirements for the degree of Doctor of Philosophy.

December 2000


Winfred M. Phillips
Dean, Graduate School